

Dissertation  
submitted to the  
Combined Faculties of the Natural Sciences and for Mathematics  
of the Ruperto-Carola University of Heidelberg, Germany  
for the degree of  
Doctor of Natural Sciences

Put forward by  
**Dipl.-Phys. Gero Jürgens**  
born in Northeim  
Oral examination: January 23<sup>rd</sup>, 2013



# **Evolution and observational signatures of cosmic structures**

Referees: Prof. Dr. Matthias Bartelmann  
Prof. Dr. Luca Amendola



*“Vorurteile sind keine Gedanken.”*  
– Sir Yehudi Menuhin



## Entwicklung und beobachtbare Signaturen kosmischer Strukturen

**Zusammenfassung:** Zwei Themen bilden den Inhalt dieser Arbeit. Im ersten Teil untersuchen wir nichtlineare kosmische Strukturbildung mit Hilfe von Zeitrenormierungsgruppen (TRG). Hierbei wurde zusätzlich das störungstheoretische tree-level Trispektrum in der Zeitentwicklungsgleichung für das Bispektrum berücksichtigt. Unter Annahme Gaußscher Anfangsbedingungen wurde eine signifikante Verbesserung in der Vorhersage des Leistungsspektrums von dunkler Materie erzielt. Bei Rotverschiebung  $z = 1$  lag die Genauigkeit für Wellenzahlen im Bereich  $k < 0.18 \text{ hMpc}^{-1}$  bei 1%. Für größere Wellenzahlen,  $k > 0.25 \text{ hMpc}^{-1}$ , hingegen bricht die störungstheoretische Beschreibung des Trispektrums zusammen. Unsere Ergebnisse bekräftigen die Bedeutung von Korrelatoren höherer Ordnungen für die nichtlineare Entwicklung des Leistungsspektrums. Allerdings beschränkt diesbezüglich der schnelle Anstieg von numerischem Rechenaufwand den Anwendungsbereich der TRG-Methode.

Im Mittelpunkt des zweiten Teils stehen Schätzungen von Signal-Rausch-Verhältnissen möglicher Messungen von Kreuzkorrelatoren zwischen dem integrierten Sachs-Wolfe (iSW) Effekt  $\tau$  und dem Dichtefeld von Markierergalaxien  $\gamma$  unter Annahme von Daten aus der *Planck*-Mission und Galaxiendurchmusterungen ähnlich zu *Euclid*. Orthogonale Polynome wurden als Sichtlinienwichtungsfunktionen für das Galaxienfeld benutzt, um tomographische Informationen des Kreuzspektrums aufzulösen. Bei einem Zustandsgleichungsparameter  $w = -0.9$  bewirkte unsere tomographische Methode einen Anstieg von 15% im Signal-Rausch-Verhältnis  $\Sigma$  des Kreuzspektrums (10% für  $w = -1.0$ ). Desweiteren wurden Kreuzbispektren und Kreuztrispektren hinsichtlich einer möglichen Messung des nichtlinearen iSW-Effekts untersucht. Wegen der geschätzten Signal-Rausch-Verhältnisse von  $\Sigma \approx 0.83$  für das gemischte Bispektrum  $\langle \tau\gamma^2 \rangle$  und von  $\Sigma \approx 0.19$  für das gemischte Trispektrum  $\langle \tau\gamma^3 \rangle$  betrachten wir den Effekt als nicht messbar in Korrelationen selbst mit zukünftigen Galaxiendurchmusterungen.

## Evolution and observational signatures of cosmic structures

**Abstract:** Two main topics form the content of this thesis. In the first part, non-linear cosmological structure formation is studied within the time renormalization group (TRG) formalism. The tree-level perturbative trispectrum was included in the time evolution of the bispectrum. Using Gaussian initial growing mode conditions we achieved an improvement in the predictions of the dark matter power spectrum in the mildly non-linear regime. We reached percent accuracy for wave numbers  $k < 0.18 \text{ hMpc}^{-1}$  for redshift  $z = 1$ , while for  $k > 0.25 \text{ hMpc}^{-1}$  the perturbative description of the trispectrum breaks down. Our results emphasize the importance of higher order correlators for the non-linear power spectrum evolution, but the fast increase in numerical cost limits the applicability of the TRG method.

Subject of the second part are signal-to-noise estimates for possible cross-correlation measurements between the integrated Sachs-Wolfe (iSW) effect  $\tau$  and the tracer galaxy density field  $\gamma$  assuming data from the *Planck* mission and a *Euclid*-like galaxy survey. Orthogonalized polynomial line-of-sight weighting functions for the galaxy field are employed to resolve tomographical information of the cross-spectrum. For the equation-of-state parameter  $w = -0.9$  our tomographic method provides a 15% increase in the signal-to-noise ratio  $\Sigma$  of the cross-spectrum (10% for  $w = -1.0$ ). Furthermore, cross-bispectra and cross-trispectra are studied with respect to a possible detection of the non-linear iSW effect. Finding values of  $\Sigma \approx 0.83$  for the mixed bispectrum  $\langle \tau\gamma^2 \rangle$  and  $\Sigma \approx 0.19$  in case of the trispectrum  $\langle \tau\gamma^3 \rangle$ , the effect has to be regarded as undetectable in correlations with future galaxy surveys.



# Contents

<b>Abstract</b>	<b>1</b>
<b>Table of Contents</b>	<b>3</b>
<b>List of Figures</b>	<b>5</b>
<b>List of Tables</b>	<b>5</b>
<b>Introduction</b>	<b>7</b>
<b>1. Cosmology</b>	<b>11</b>
1.1. Friedman-Lemaître-Robertson-Walker model . . . . .	11
1.2. Friedman's equations . . . . .	13
1.3. Cosmological redshift and comoving distance . . . . .	13
1.4. Dimensionless density parameters . . . . .	14
<b>2. Structure formation</b>	<b>19</b>
2.1. Vlasov equation . . . . .	19
2.2. Fluid equations . . . . .	21
2.3. Gaussian random fields and ergodicity . . . . .	22
2.4. Homogeneity and isotropy . . . . .	23
2.5. Non-Gaussianities . . . . .	24
2.6. Evolution in Fourier space . . . . .	25
2.7. Perturbation theory . . . . .	25
2.8. Matrix formulation . . . . .	27
<b>3. Perturbation theory trispectrum in the time renormalization group approach</b>	<b>33</b>
3.1. Introduction . . . . .	33
3.2. Time renormalization . . . . .	34
3.3. Trispectrum . . . . .	38
3.4. Diagrammatic description . . . . .	41
3.5. Numerical results . . . . .	44
3.6. Full trispectrum evolution - limits of contemporary numerics . . . . .	45
3.7. Summary . . . . .	46
<b>4. Introduction to the integrated Sachs-Wolfe effect</b>	<b>49</b>
4.1. Cosmic microwave background . . . . .	49
4.2. Anisotropies . . . . .	50
4.3. Galaxy distribution . . . . .	51
4.4. Integrated Sachs-Wolfe effect . . . . .	52
4.5. Statistics of fluctuations on the sky . . . . .	53
4.6. Flat sky to full sky correspondence . . . . .	54
4.7. Limber equation . . . . .	56

<b>5. Integrated Sachs-Wolfe tomography with orthogonal polynomials</b>	<b>57</b>
5.1. Introduction . . . . .	57
5.2. Tomography with orthogonal polynomials . . . . .	58
5.3. Statistics . . . . .	61
5.4. Summary . . . . .	67
<b>6. Cross-bispectra and cross-trispectra of the non-linear integrated Sachs-Wolfe effect and the tracer galaxy density field</b>	<b>69</b>
6.1. Introduction . . . . .	69
6.2. Non-linear iSW-effect . . . . .	70
6.3. Cross-bispectra and cross-trispectra . . . . .	71
6.4. Detectability . . . . .	77
6.5. Summary . . . . .	81
<b>Summary and conclusions</b>	<b>83</b>
<b>A. Analytical details</b>	<b>87</b>
A.1. Wick's theorem . . . . .	87
A.2. Compact structure formation equations . . . . .	88
A.3. Derivation of the iSW-effect in general relativity . . . . .	90
A.4. Analytical details of signal-to-noise ratios . . . . .	91
<b>B. Numerical Details</b>	<b>93</b>
B.1. The correction integrals . . . . .	93
B.2. Monte Carlo integration . . . . .	94
<b>C. Fourier conventions</b>	<b>97</b>
C.1. Spatial transformations . . . . .	97
C.2. Time transformations, Laplace transform . . . . .	98
<b>D. Units and constants</b>	<b>99</b>
D.1. Astronomical units and physical constants . . . . .	99
<b>Bibliography</b>	<b>101</b>
<b>Acknowledgements</b>	<b>109</b>

# List of Figures

1.1.	2d-illustration of the three different curvature cases. . . . .	12
1.2.	Density parameters in dependence of the scale factor for the best-fitting cosmology. . . . .	16
2.1.	The acoustic peak in the two-point matter correlation function. . . . .	32
3.1.	Correction integrals in the time renormalization group approach. . . . .	36
3.2.	Time renormalization integrals relative to a smooth linear power spectrum. . . . .	38
3.3.	Diagrammatic illustration of the fundamental correlators and interactions. . . . .	40
3.4.	The lowest order bispectrum corrections from the tree-level trispectrum. . . . .	42
3.5.	The lowest order corrections to the power spectrum from the tree-level trispectrum. . . . .	43
3.6.	Predicted matter power spectrum in comparison to $N$ -body simulations for $z = 1$ . . . . .	44
3.7.	Predicted matter power spectrum in comparison to $N$ -body simulations for $z = 0$ . . . . .	45
5.1.	Orthogonal polynomials and the accuracy of the orthogonality relation. . . . .	59
5.2.	Weighted galaxy efficiency functions as a function of comoving distance. . . . .	61
5.3.	Tomographic galaxy-galaxy spectra and Galaxy-iSW cross-spectra. . . . .	62
5.4.	Sensitivity of the Fisher matrix with respect to the parameters $h$ and $\Omega_m$ . . . . .	64
5.5.	Cumulative signal-to-noise ratio of the iSW-galaxy cross-spectrum. . . . .	66
5.6.	Marginalized and conditional errors on the fiducial cosmological parameters. . . . .	67
5.7.	The $1\sigma$ -error ellipses on cosmological parameter estimates. . . . .	68
6.1.	iSW and galaxy time evolution functions. . . . .	71
6.2.	Weighting functions of the mixed iSW-galaxy trispectra. . . . .	73
6.3.	Time evolution functions for equilateral iSW-galaxy bispectra and trispectra. . . . .	75
6.4.	The absolute values of the equilateral iSW-galaxy bispectra and trispectra. . . . .	76
6.6.	Cumulative signal-to-noise ratios of the bispectra and trispectra. . . . .	80
6.7.	Differential contributions of the equilateral bispectra to the signal-to-noise ratios. . . . .	81
B.1.	Coordinate system for the time renormalization integrals. . . . .	93
B.2.	Coordinate transformation for the time renormalization integrals. . . . .	94
D.1.	Definition of a parsec. . . . .	99

# List of Tables

1.1.	The best-fitting parameters for our cosmological model. . . . .	15
6.1.	Properties of the <i>Euclid</i> galaxy survey. . . . .	77
6.2.	Cumulative signal-to-noise ratios of the mixed bispectra and trispectra. . . . .	80



# Introduction

Exploring the origin of our Cosmos obtained a different quality, when we started to collect information from outside of our own Galaxy. In the first half of the past century galaxies were found to move apart from one another on average by measurements of their redshift. They even move the faster the more distant they are. The cosmological redshift was established as an indicator of age and distance of an astrophysical object. Soon, older and more distant galaxies were found, whose existence is only consistent with Einstein's theory of General Relativity, if the Universe is assumed to have originated from an initial singularity, the Big Bang, which is today estimated to have occurred 13.7 billion years ago.

The field of cosmology has experienced a fast evolution over the past twenty years. Today, we are capable of describing almost all phenomena observed in the Cosmos with a few parameters only, whose statistical bounds have also improved significantly. This success is mainly tribute to several surveys. Their observational outcome establishes - once they are combined - the model which is known as the standard model of cosmology or  $\Lambda$ CDM model. The detailed observation of the cosmic microwave background (CMB), which started with the launch of the COBE satellite in 1989 and was followed by seven years of WMAP observations, is today continued with unprecedented resolution by the *Planck* satellite. Besides this, the observation of the late dynamics of the Universe's expansion via Supernova surveys and the measurement of baryonic signatures from the early Universe contribute the major statistical constraints on the cosmological parameters.

So, are we done yet? Not quite - having a powerful model passing successfully our cosmological probes is not very valuable as long as some constituents are only placeholders. The largest part of the Universe's energy content is the one which is responsible for its late time acceleration - the cosmological constant. It was introduced by Einstein to achieve a model for a static universe. It can be understood as a pure geometrical constant as part of space-time or as a term contributing to the energy-momentum content. In the latter case it is also referred to as dark energy. Independent of its nature it accounts for approximately 70% of the energy content today. With roughly 23%, dark matter is the second largest contributor and also here the word *dark* expresses our ignorance of its detailed nature and the fact that it only interacts gravitationally. Its existence is necessary to explain flat rotation curves in spiral galaxies and the fast structure formation beginning from the small perturbations during the time of recombination. Summing up, the nature of more than 90% of the energy content of our Universe is not entirely understood. Furthermore, the universe as we observe it today is spatially almost perfectly flat and the cosmic microwave background is isotropic with relative deviations of order  $10^{-5}$ . For these observations to be consistent with the model, the Cosmos must have undergone an epoch of accelerated expansion in its early stages - the so-called inflation. Also this era is not understood at the present day.

Thinking about this, many questions remain to be clarified: Why is the cosmological constant so much smaller than quantum field theory estimates for the vacuum energy? Is it a constant or does it vary with time? Is it of geometrical nature can it be understood as a quintessence field or one of many other suggested fields? Can inflation and late time acceleration have the same physical origin? Which candidate is the right one for dark matter?

We could ask many more of these important cosmological questions here. But the focus of this thesis is only indirectly connected to these problems. For the description of the unknown constituents diverse models are discussed in the community. In order to find deviations from the  $\Lambda$ CDM model or to exclude alternative models one needs to compare theoretical predictions to observations, which are often not available at the same level of accuracy. It can then happen that the theory is too involved

to reach the accuracy of observation. In this case, one first has to improve the theoretical predictions. If the theoretical description is rather simple one can estimate the range of possible results before the observations are done depending on the predicted measurement accuracy. The content of this thesis can be divided into two parts, each of which is motivated by one of the two aforementioned cases.

The topic of the first part is the evolution of structures from initially tiny perturbations in the density and velocity field. This phenomenon is known as structure formation. It plays an important role in cosmology and is a vivid area of research. From the early times, when small deviations from homogeneity - presumably quantum fluctuations - were imprinted in the density field, over the time of recombination, when baryonic oscillations were frozen, to the later stages, when stars and planets were formed, processes of structure formation have to be understood for a thorough theoretical prediction. We concentrate on the evolution of structures in the matter dominated universe after the time of recombination,  $0 < z < 100$ . Due to the nonlinearity of the continuity equation and the Euler equation there does not exist an exact analytical solution. However, we would like to keep our focus on analytical or semi-analytical approximations, since numerical simulations lack the ability to scan over a large range of different cosmologies. The validity of all kinds of perturbative approaches strongly depends on the scale and the amplitude of the structures at hand. While they perform very well on scales larger than 100 Mpc and low amplitudes, they fail miserably in case of stronger fluctuations and on scales smaller than 10 Mpc. Since the amplitude of structures continues to grow on average during cosmic history, these methods also perform the better the earlier times are considered.

In the last fifteen years one started to apply semi-analytical methods known from quantum field theory on classical cosmological density fields and achieved considerable improvement in the field of structure formation. Renormalization group techniques do not work perturbatively but follow the change of physical laws along the aforementioned variables. Since initial conditions are given as a random field, the quantities of interest are the correlators of these fields to different orders. The most important quantity is the Fourier transform of the two-point correlator - the power spectrum. It would contain all statistical information in case of a Gaussian random field. In the time renormalization group (TRG) approach one follows the time evolution of correlators of all orders and finds an infinite coupled hierarchy of evolution equations (Pietroni, 2008). In a first approach to solve for the power spectrum one neglected the non-Gaussianities of the four-point function, also known as trispectrum. A slight improvement in the prediction of the power spectrum with respect to standard perturbation theory was achieved. As the next logical step, we studied the influence of the trispectrum on the predictions of the power spectrum in this thesis. To keep the numerical cost at a reasonable level we decided for a hybrid approach. We extended the non-perturbative approach including the influence of the tree-level perturbation theory trispectrum and illustrate the corrections in a diagrammatic way. We also argue that including the trispectrum in a non-perturbative way would increase the numerical cost to an unreasonable level.

As mentioned earlier, in the second part we study the possible outcome of an analysis. Here, the object is an anisotropy of the CMB called integrated Sachs-Wolfe (iSW) effect. Time-varying potentials along the way of the CMB photons, decoupled from matter since the Universe had cooled down sufficiently to form neutral hydrogen, changed their frequency and therefore induced a secondary anisotropy in the CMB. The effect is highly sensitive to the amount of dark energy and vanishes in case of a pure dark matter universe. Unfortunately, the signal strength is much weaker than the amplitude of initial anisotropies and can thus only be observed via cross-correlation with a field representing the origin of the effect. Since the time-varying potentials can not be observed directly one correlates the CMB observations with the galaxy density field, which should be tightly bound to the potential field.

While the line of sight information in the iSW signal is lost, this is not the case for the galaxy source field. For this reason one can improve the signal-to-noise using a tomographical technique. We perform for the first time a line-of-sight tomographical Fisher analysis for the integrated Sachs-Wolfe effect. For the study of related effects - as for instance weak gravitational lensing - the line-of-sight is often divided into redshift bins, which diagonalizes the noise part of the covariance. In contrast

to this, we chose in this approach orthogonal polynomials as weighting functions to diagonalize the signal part of the covariance (Schäfer & Heisenberg, 2011). This change in basis system will not alter the achievable signal-to-noise ratio but may be chosen as alternative technique in cases, in which the signal's cross-correlation is hard to evaluate.

One furthermore distinguishes between the linear and the non-linear iSW effect, which is also known as the Rees-Sciama effect. While the signal-to-noise ratio lies around  $\sim 5$  in case of the linear effect, the signal strength of the non-linear effect does not exceed the amplitude of the noise contribution. Motivated by this, we also studied the tree level perturbative cross bispectra and cross trispectra with respect to their signal-to-noise spectra and their qualitative behavior.

The thesis has the following structure: First, we introduce in Chapter 1 the physical principles which the  $\Lambda$ CDM model is based on. In Chapter 2 we lay out the definitions and techniques of structure formation as a preparation of Chapter 3, in which we include the tree-level trispectrum into the time renormalization approach. In Chapter 4 we present the basics of the cosmological microwave background and its anisotropies - especially the integrated Sachs-Wolfe effect. While Chapter 5 is dedicated to the presentation of our tomographical approach with orthogonal polynomials to measure the iSW effect, we study the cross bispectra and cross trispectra between the iSW effect and the galaxy density field in Chapter 6. The Appendix is divided into parts covering analytical and numerical details in Chapter A and Chapter B, respectively. Finally, in Chapter C and D we defined Fourier conventions, units and relevant constants.

Parts of this work were published in the following papers:

- **Jürgens, G.** & Bartelmann, M. (2012): *Perturbation theory trispectrum in the time renormalization approach*. [MNRAS, 230](#).
- **Jürgens, G.** & Schäfer, B. M. (2012a): *Cross bispectra and trispectra of the non-linear integrated Sachs-Wolfe effect and the tracer galaxy density field*. [MNRAS](#), accepted, [ArXiv e-prints 1210.7513](#)
- **Jürgens, G.** & Schäfer, B. M. (2012b): *Integrated Sachs-Wolfe tomography with orthogonal polynomials*. [MNRAS, 425](#).



# 1

## Chapter 1

# Cosmology

In the following chapter, we would like to introduce the basic principles of cosmology and the most established  $\Lambda$ CDM model, which is based on Einstein's General Relativity. Relevant distance measures and the cosmological redshift will also be subject of this chapter since it is essential for the understanding throughout the thesis. More comprehensive introductions to cosmology can be found in [Coles & Lucchin \(2002\)](#); [Bartelmann \(2004\)](#); [Weinberg \(2008\)](#).

## 1.1. Friedman-Lemaître-Robertson-Walker model

On large cosmological scales gravity is by far the dominant of all forces. Newtonian gravity can only be applied in case of weak fields and on short distances, where retardation effects are irrelevant. For this reason, the standard cosmological models are based on Einstein's general relativity ([Einstein, 1915, 1916](#)) which could not be proven wrong by any Solar System test so far. Time and space are not strictly separated and the universe is described as a space-time manifold of four dimensions. All distance measurements on this manifold are based on the metric tensor  $g_{\mu\nu}$  and its eigentime element

$$ds^2 = g_{\mu\nu} dx^\mu dx^\nu, \quad (1.1)$$

where  $0 \leq \mu, \nu \leq 3$  and  $g_{\mu\nu} = g_{\nu\mu}$ . In General Relativity the dynamics of the space-time metric  $g_{\mu\nu}$  is non-linearly connected to the energy-momentum tensor  $T_{\mu\nu}$  and is described by Einstein's field equations,

$$R_{\mu\nu} - \frac{1}{2}g_{\mu\nu}R - \Lambda g_{\mu\nu} = \frac{8\pi G}{c^4}T_{\mu\nu}. \quad (1.2)$$

The left hand side is non-linear since the Ricci tensor  $R_{\mu\nu}$  and its contraction, the Ricci scalar  $R \equiv R^\mu{}_\mu$ , are formed from first and second derivatives of the metric tensor  $g_{\mu\nu}$ . Both are measures of the space-time curvature. Furthermore,  $c$  denotes the speed of light,  $G$  is Newton's gravitational constant and  $\Lambda$  is the so-called cosmological constant, which was originally introduced by Einstein to achieve a static universe. All forms of matter encoded in  $T_{\mu\nu}$  directly influence the space-time geometry and vice versa. Due to the non-linearity of the field equations (1.2), it is not possible to give a general solution without any further approximations or constraints.

### 1.1.1. The Robertson-Walker metric

For the Friedman-Lemaître-Robertson-Walker model two assumptions are imposed leading to strong space-time symmetry. The assumptions are also known as the *Cosmological Principle*:

- (1) *The Universe is isotropic.*

Motivated by the observation of the cosmic microwave background (CMB), the Universe is

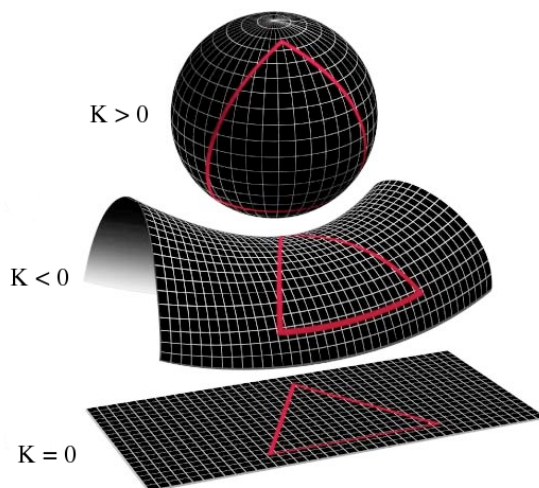


**Figure 1.1.:** 2d-illustration of the three different curvature cases <sup>1</sup>: flat universe ( $K = 0$ ), open universe ( $K < 0$ ) and closed universe ( $K > 0$ ).

assumed to have started from an almost perfectly isotropic state. The emission originates from a time when the Universe was 380,000 years old and radiation decoupled from the matter content. Although the matter content became more and more clumpy until today, the assumption holds still true if one averages over a scale of 100 Mpc.

(2) *The Universe is homogeneous (Copernican Principle).*

The Copernican principle states, that our Earth does not occupy a special place in the Universe. Therefore, our Universe has to be isotropic around every point. Hence it must be homogeneous.

Taking the cosmological principle into account, there exists only one metric fulfilling the aforementioned symmetries for a simply-connected topology. The metric is called Robertson-Walker metric and a coordinate system can be found in which the metric tensor can be simplified considerably,

$$\begin{aligned} ds^2 &= c^2 dt^2 - a(t)^2 (dx^2 + f_K^2(x) d\omega^2) \\ d\omega^2 &= d\theta^2 + \sin^2 \theta d\phi^2 \end{aligned} \quad (1.3)$$

(Robertson, 1935; Walker, 1935) with the time dependent scale factor  $a(t)$  and the radial function  $f_K(w)$ ,

$$f_K(w) = \begin{cases} K^{-\frac{1}{2}} \sin(K^{\frac{1}{2}}x) & (K > 0) \\ x & (K = 0) \\ |K|^{-\frac{1}{2}} \sinh(|K|^{\frac{1}{2}}x) & (K < 0) \end{cases} \quad (1.4)$$

The parameter  $K$  describes the spatial curvature of the Universe. It can assume the following values

- (1)  $K < 0$ : open universe,
- (2)  $K = 0$ : flat universe,
- (3)  $K > 0$ : closed universe.

The three different cases of the curvature parameter  $K$  are shown in Fig. (1.1) as a 2d-illustration. Only for  $K = 0$  the angles in a triangle sum up to  $180^\circ$ , while the sum is  $> 180^\circ$  in the closed case and  $< 180^\circ$  in the open case.

<sup>1</sup><http://www.talkorigins.org/faqs/astronomy/bigbang.html>, slightly modified version.

Since observations indicate the curvature parameter  $K$  to be close or equal to zero it is assumed to vanish in our model. Then, the eigentime element becomes

$$ds^2 = c^2 dt^2 - a(t)^2 (dx^2 + x^2 d\omega^2). \quad (1.5)$$

## 1.2. Friedman's equations

With the symmetry imposed by the cosmological principle the energy momentum tensor takes on the form of an ideal fluid. This is represented by the pressure  $p(t)$  and the density  $\rho(t)$ , which can only be functions of time due to homogeneity. If Cartesian coordinates are chosen for the spatial part, the energy-momentum tensor can be written as

$$T_{\mu\nu} = \begin{pmatrix} \rho c^2 & 0 & 0 & 0 \\ 0 & -p & 0 & 0 \\ 0 & 0 & -p & 0 \\ 0 & 0 & 0 & -p \end{pmatrix}. \quad (1.6)$$

This is the energy momentum tensor of a perfect fluid. In the special case of the Robertson-Walker metric from eqn. (1.5) and the energy-momentum tensor of eqn. (1.6) the field equations (1.2) can be simplified to differential equations for the scale factor  $a(t)$ ,

$$\left(\frac{\dot{a}}{a}\right)^2 = \frac{8\pi G}{3}\rho + \frac{\Lambda}{3} \quad (1.7)$$

$$\frac{\ddot{a}}{a} = -\frac{4\pi G}{3}\left(\rho + \frac{3p}{c^2}\right) + \frac{\Lambda}{3}. \quad (1.8)$$

These are the Friedman Equations (Friedmann, 1922, 1924; Lemaître, 1927). The scale factor of today  $t_0$  is set to unity:  $a_0 \equiv a(t_0) = 1$ . If a Robertson-Walker metric also obeys the two Friedman equations (1.7)-(1.8), it is called Friedman-Lemaître-Robertson-Walker metric.

## 1.3. Cosmological redshift and comoving distance

Light rays travel along so-called null geodesics along which  $ds^2 = 0$  holds. For light rays moving radially in our coordinate system, i.e.  $d\omega = 0$ , eqn.(1.5) then implies

$$c dt = \pm a(t) dx.$$

One can now define the so-called proper distance and comoving distance,

- (1) The *proper distance*  $D_{\text{prop}}$ .

The proper distance is defined via the time that light needs to travel from one point to another,  $dD_{\text{prop}} \equiv -c dt = -c da/\dot{a}$ . For convenience, the coordinate system was chosen such, that  $d\omega = 0$ . One can now define the total distance between two redshifts,

$$D_{\text{prop}}(z_1, z_2) = -c \int_{a(z_1)}^{a(z_2)} \frac{da'}{\dot{a}'}. \quad (1.9)$$

- (2) The *comoving distance*  $D_{\text{com}}$ .

The comoving distance measures the conformal time  $\tau = t/a$ , that light needs to travel from one point to another,  $dD_{\text{com}} = dD_{\text{prop}}/a = -c da/(a\dot{a})$ . In other words, the scale factor  $a$ ,

describing the expansion of the universe, is divided out and the distance is measured in terms of the comoving coordinate  $x$ ,

$$D_{\text{com}}(z_1, z_2) = -c \int_{a(z_1)}^{a(z_2)} \frac{da'}{a' \dot{a}'}. \quad (1.10)$$

If now observer  $o$  and emitter  $e$  are fundamental observers, their comoving distance is constant in time,

$$\begin{aligned} \frac{d}{dt_e} x_{eo} &= \frac{dt}{dt_e} \frac{d}{dt} \int_{t_e}^{t_o} \frac{c dt}{a(t)} = \frac{c}{a_o} \frac{dt_o}{dt_e} - \frac{c}{a_e} = 0 \\ \frac{dt_o}{dt_e} &= \frac{a_o}{a_e}. \end{aligned} \quad (1.11)$$

If one relates the time dilatation effect from eqn. (1.11) to the frequencies and wavelengths of the emitted and observed light, one finds

$$\frac{\lambda_o}{\lambda_e} = \frac{\nu_e}{\nu_o} = \frac{dt_o}{dt_e} = \frac{a_o}{a_e} = 1 + z, \quad (1.12)$$

where the redshift  $z$  has been introduced in the last step as the relative change of wavelength,

$$z \equiv \frac{\lambda_o - \lambda_e}{\lambda_e}. \quad (1.13)$$

This implies that the wavelength  $\lambda$  of a light ray becomes red-shifted in an expanding universe, since then  $a_o > a_e$ . For this reason, as observers on our Earth we can use the cosmological redshift  $z$  as a cosmological distance measure for sources, which emitted light, when the Universe had the scale factor  $a$ ,

$$a = \frac{1}{1 + z}. \quad (1.14)$$

## 1.4. Dimensionless density parameters

The relative expansion rate appearing in the first Friedman equation (1.7) is known as the Hubble function  $H(t)$ , which is a time dependent quantity,

$$H(t) \equiv \frac{\dot{a}}{a}. \quad (1.15)$$

Its value of today  $H_0$  is the so-called Hubble constant,

$$H_0 \equiv H(t_0) = 100 h \frac{\text{km}}{\text{s Mpc}}, \quad (1.16)$$

with the Hubble parameter  $h$ . With observations of Cepheids<sup>2</sup> the Hubble parameter can be measured (Hubble, 1929; Freedman et al., 2001). We give here the value of  $h = 0.704 \pm 0.013$  from the seven-year Wilkinson Microwave Anisotropy Probe (WMAP) data (Komatsu et al., 2011). This value states that our universe is expanding. General relativity is also allowing for the cosmological constant  $\Lambda$ , which therefore can not be neglected a priori. While Albert Einstein used it to account for a static universe, dropping  $\Lambda$  would with eqn. (1.8) inevitably lead to a decelerating universe. Since observations are indicating the opposite, namely an accelerating universe (Riess et al., 1998; Perlmutter et al., 1999), it is included in  $\Lambda$ CDM representing the so-called dark energy component, the physical composition

parameter	value	comments
$h$	$0.704^{+0.013}_{-0.014}$	
$\Omega_{\text{b}0}$	$0.0456 \pm 0.0016$	
$\Omega_{\text{CDM}0}$	$0.227 \pm 0.014$	assuming $\Omega_{\text{K}0} = 0$
$\Omega_{\text{m}0}$	$0.272^{+0.016}_{-0.015}$	
$\Omega_{\Lambda 0}$	$0.728^{+0.015}_{-0.016}$	
$t_0$	$13.75 \pm 0.11 \text{ Gyr}$	
$\Omega_{\text{r}0}$	$(8.375^{+0.309}_{-0.333}) \times 10^{-5}$	from CMB temperature (including neutrinos)
$\Omega_{\text{K}0}$	$-0.0023^{+0.0054}_{-0.0056}$	assuming $\Omega_{\text{K}0} \neq 0$
$\Omega_{\text{tot}0}$	$1.0023^{+0.0056}_{-0.0054}$	

**Table 1.1.:** The best-fitting values including WMAP7-, BAO- and  $H_0$  measurements. Also the contribution from neutrinos was included adding a factor of 1.68 to  $\Omega_{\text{r}}$ .

of which is still unclear. For the construction of dimensionless density parameters it is convenient to introduce the critical density  $\rho_{\text{cr}}(t)$ ,

$$\rho_{\text{cr}} := \frac{3H^2}{8\pi G} \quad (1.17)$$

and to describe a particular mass component by the dimensionless ratio

$$\Omega := \frac{\rho}{\rho_{\text{cr}}} . \quad (1.18)$$

Typically, two types of matter are distinguished: non-relativistic matter  $\rho_{\text{m}}$  and relativistic matter  $\rho_{\text{r}}$ . Their different behavior can be observed in their equation of state

$$p = w\rho c^2 , \quad (1.19)$$

where the equation-of-state parameter  $w$  was defined. Non-relativistic matter can occur in form of cold dark matter and baryonic matter  $\rho_{\text{m}} = \rho_{\text{CDM}} + \rho_{\text{b}}$ . Dark matter interacts only gravitationally and moves slowly with respect to the speed of light. Cold dark matter in particular can be assumed as being pressure-less ( $w = 0$ ). Its existence was motivated by discrepancies in the mass-to-light ratios of galaxy clusters (Zwicky, 1937), but the nature of dark matter is still unknown. Relativistic matter  $\rho_{\text{r}}$  has an equation-of-state parameter of  $w = 1/3$  and mainly consists of photons and neutrinos.

One can combine eqs. (1.7)-(1.8) to find the adiabatic equation,

$$\frac{d}{dt} (a^3 \rho c^2) + w \rho c^2 \frac{d}{dt} (a^3) = 0 , \quad (1.20)$$

from which one can infer the different scale dependences of the matter constituents,

$$\begin{aligned} \frac{\rho_{\text{m}}}{\rho_{\text{m}0}} &= a^{-3} \\ \frac{\rho_{\text{r}}}{\rho_{\text{r}0}} &= a^{-4} . \end{aligned} \quad (1.21)$$

The dimensionless density parameters can now be introduced for the dust and radiation components,

$$\Omega_{\text{m}0} = \frac{\rho_{\text{m}0}}{\rho_{\text{cr}0}} \quad \text{and} \quad \Omega_{\text{r}0} = \frac{\rho_{\text{r}0}}{\rho_{\text{cr}0}} . \quad (1.22)$$

<sup>2</sup>Cepheids form a particular class of variable stars. For the tight correlation between their period of variability and their absolute luminosity they can be used as standard candles to determine the distance to their host galaxy.

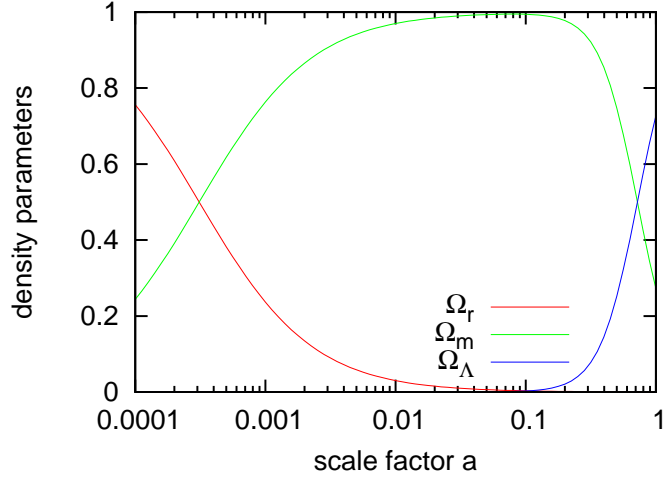


**Figure 1.2.:** The density parameters in dependence of the scale factor for the WMAP7+BAO+ $H_0$  best-fitting cosmology. *Figure taken from Angrick (2011).*

This can also be done for the cosmological constant  $\Lambda$  and the spatial curvature  $K$ ,

$$\Omega_{\Lambda 0} = \frac{\Lambda}{3H_0^2} \quad \text{and} \quad \Omega_{K0} \equiv -\frac{Kc^2}{H_0^2}. \quad (1.23)$$

Now, we can rewrite the first Friedman equation (1.7) as

$$H^2(a) = H_0^2 E^2(a) \equiv H_0^2 (\Omega_{r0} a^{-4} + \Omega_{m0} a^{-3} + \Omega_{K0} a^{-2} + \Omega_{\Lambda 0}), \quad (1.24)$$

where the expansion function  $E(a)$  was defined. For  $a_0 = a(t_0) = 1$  this yields

$$\Omega_m + \Omega_r + \Omega_K + \Omega_\Lambda = 1. \quad (1.25)$$

This expresses that today's total energy density of our universe is equal to the critical density  $\rho_{\text{cr}}(t_0)$  defined in eqn. (1.17).

A few interesting implications should be mentioned at this point:

- Today, the contribution of radiation is negligible compared to the dust component, but eqn. (1.24) implies that there must have been a time when it was the other way around.
- At late times and for large scale factors  $a$ , the cosmological constant term will be dominant in eqn. (1.24) and the evolution of the scale factor can be approximated as  $\dot{a} \approx H_0 \sqrt{\Omega_{\Lambda 0}} a$ , which implies an exponential growth of the Universe,  $a \propto \exp(H_0 \sqrt{\Omega_{\Lambda 0}} t)$ .
- A universe with  $\Omega_m + \Omega_r + \Omega_\Lambda = 1$  implies spatial flatness,  $K = 0$ , and therefore leads to a spatially Euclidean universe.

In Table 1.1, the best-fitting cosmological parameters and the the age of the Universe  $t_0$  are listed, which were inferred from the 7-year data release of the Wilkinson Microwave Anisotropy Probe (WMAP7) combined with data from baryonic acoustic oscillations (BAO)<sup>3</sup> and measurements of the Hubble constant  $H_0$  (Komatsu et al., 2011). In Fig. 1.2 the evolution of the density parameters of the aforementioned model is depicted. The index 0 is sometimes omitted in the notation for the cosmological matter density parameters  $\Omega_{m0}$ ,  $\Omega_{\text{CDM}0}$ ,  $\Omega_{\Lambda 0}$  and  $\Omega_{b0}$ , if a confusion with the time dependent variables can be excluded.

<sup>3</sup>see also Section 2.8.5

It might appear worrying that only the nature of a small fraction of the Universe's energy content can be considered to be understood. Today, *normal* baryonic matter only contributes  $\sim 4 - 5\%$  to the energy content of our Universe, radiation even only a negligible fraction of  $\sim 10^{-5}$ . In contrast to this, the Universe consists to 23% of dark matter and the rest is made up by the cosmological constant or dark energy,  $\sim 72\%$ . However, even more astonishingly it is that the  $\Lambda$ CDM model was found to be in remarkable agreement with most cosmological probes and for this reason has become the standard model of cosmology.



# 2

## Structure formation

### 2.1. Vlasov equation

Our introduction to cosmological structure formation in the Eulerian picture could start directly from the fluid equations. However, it is interesting to see the chain of argumentation from microscopic point particles to a continuous description and the necessary assumptions. A thorough discussion of this issue can be found in [Pietroni et al. \(2012\)](#). The reader, who is only interested in the theory based directly on the description of matter as a continuous field, may skip this section.

The intuitive starting point is a microscopic description of the system of  $N$  point-like particles in form of their discrete distribution in phase space,

$$f_{\text{mic}}(\mathbf{x}, \mathbf{p}, \tau) = \sum_{n=1}^N \delta_{\text{D}}(\mathbf{x} - \mathbf{x}_i(\tau)) \delta_{\text{D}}(\mathbf{p} - \mathbf{p}_i(\tau)) \quad (2.1)$$

with the Dirac  $\delta_{\text{D}}$ -function. This expression is also known as the Klimontovich density. The particle's physical coordinate  $\mathbf{r} = a \mathbf{x}$  can be split up into the background motion and the peculiar motion,

$$\dot{\mathbf{r}} = \dot{a} \mathbf{x} + a \dot{\mathbf{x}}, \quad (2.2)$$

where the dots indicate derivatives with respect to conformal time  $d\tau = dt/a$ . In Newtonian dynamics the coordinates and momenta of the individual particles now obey

$$\begin{aligned} \dot{\mathbf{x}}_n &= \frac{\mathbf{p}}{am} \\ \dot{\mathbf{p}}_n &= -am \nabla \phi_{\text{mic}}(\mathbf{x}_n, \tau), \end{aligned} \quad (2.3)$$

where the gravitational potential  $\phi_{\text{mic}}$  is defined as the deviation from the background potential,  $\phi_{\text{mic}} = \phi - \bar{\phi}$ . Consequently, the Poisson equation relates  $\phi_{\text{mic}}$  to the fluctuation of the particle density from the comoving background density  $\bar{\rho}$ ,

$$\nabla^2 \phi_{\text{mic}}(\mathbf{x}_l, \tau) = \frac{4\pi G}{a} \left[ m \sum_{k \neq l} \delta_{\text{D}}(\mathbf{x}_k - \mathbf{x}_l) - \bar{\rho} \right]. \quad (2.4)$$

Taking moments of the momentum  $p^i/am$  with the Klimontovich distribution in eqn. (2.1) one can define a number density  $n_{\text{mic}}(\mathbf{x}, \tau)$ , a particle current  $\mathbf{v}_{\text{mic}}(\mathbf{x}, \tau)$  and a velocity dispersion tensor  $\sigma_{\text{mic}}^{ij}(\mathbf{x}, \tau)$  in the following way,

$$\begin{aligned} n_{\text{mic}}(\mathbf{x}, \tau) &= \int d^3 p f_{\text{mic}}(\mathbf{x}, \mathbf{p}, \tau) \\ n_{\text{mic}}(\mathbf{x}, \tau) v_{\text{mic}}^i(\mathbf{x}, \tau) &= \int d^3 p \frac{p^i}{am} f_{\text{mic}}(\mathbf{x}, \mathbf{p}, \tau) \\ n_{\text{mic}}(\mathbf{x}, \tau) \sigma_{\text{mic}}^{ij}(\mathbf{x}, \tau) &= \int d^3 p \left( \frac{p^i}{am} - v_{\text{mic}}^i(\mathbf{x}, \tau) \right) \left( \frac{p^j}{am} - v_{\text{mic}}^j(\mathbf{x}, \tau) \right) f_{\text{mic}}(\mathbf{x}, \mathbf{p}, \tau). \end{aligned} \quad (2.5)$$

The velocity dispersion  $\sigma_{\text{mic}}^{ij}(\mathbf{x}, \tau)$  is non-zero only in points in which the trajectories of particles cross, i.e.  $\mathbf{x}_n = \mathbf{x}_m$  for  $n \neq m$ . This process is also known as shell-crossing. The name originates from the analysis of spherical collapse. In that case the crossing of two particles trajectories implies entire shells to become congruent at the same time due to spherical symmetry.

Requiring particle conservation implies mathematically the total time derivative of the particle density to vanish,  $dn_{\text{mic}}/d\tau = 0$ , and leads to the Klimontovich equation,

$$\left[ \frac{\partial}{\partial \tau} + \frac{p^i}{am} \frac{\partial}{\partial x^i} - am \nabla^i \phi_{\text{mic}}(\mathbf{x}, \tau) \frac{\partial}{\partial p^i} \right] f_{\text{mic}}(\mathbf{x}, \mathbf{p}, \tau) = 0. \quad (2.6)$$

However, due to their discrete formulation the quantities in eqn. (2.5) are difficult to handle. Fortunately, in the cosmological context we are rather interested in scales much larger than the typical distance of neighboring particles. For these two reasons, it is useful and possible to introduce averaged quantities with the help of a window function  $W(|x|)$  of scale  $L$ , beginning with the phase space density

$$f(\mathbf{x}, \mathbf{p}, \tau) = \frac{1}{V} \int d^3y W\left(\left|\frac{\mathbf{y}}{L}\right|\right) f_{\text{mic}}(\mathbf{x}, \mathbf{p}, \tau). \quad (2.7)$$

Naturally, the window function  $W(|x|)$  has to be normalized to unity,

$$1 = \frac{1}{V} \int d^3y W\left(\left|\frac{\mathbf{y}}{L}\right|\right), \quad (2.8)$$

and should be steeply decreasing for  $|x| > 1$ . This density will now behave smoothly in comparison to the Klimontovich distribution in eqn. (2.1) if sufficiently many particles are contained in the volume  $V \approx L^3$ . Reasonable choices for the window function would be any differentiable function close to a so-called *top hat* distribution

$$W(|x|) = \begin{cases} 1 & |x| \leq 1 \\ 0 & |x| > 1 \end{cases}. \quad (2.9)$$

In analogy to eqn. (2.5) one can now introduce the smoothed density  $n(\mathbf{x}, \tau)$ , velocity  $\mathbf{v}(\mathbf{x}, \tau)$  and a velocity dispersion  $\sigma^{ij}(\mathbf{x}, \tau)$ . In spite of the elegance of this formulation, it leads to an additional convolution term with the window function in the smoothed analogon to eqn. (2.6),

$$\begin{aligned} & \left[ \frac{\partial}{\partial \tau} + \frac{p^i}{am} \frac{\partial}{\partial x^i} - am \nabla_x^i \phi(\mathbf{x}, \tau) \frac{\partial}{\partial p^i} \right] f(\mathbf{x}, \mathbf{p}, \tau) \\ &= \frac{am}{V} \int d^3y W\left(\left|\frac{\mathbf{y}}{L}\right|\right) \nabla_y^i \delta\phi(\mathbf{x} + \mathbf{y}, \tau) \frac{\partial}{\partial p^i} \delta f(\mathbf{x} + \mathbf{y}, \mathbf{p}, \tau), \end{aligned} \quad (2.10)$$

where  $\delta f$  and  $\delta\phi$  indicate the local microscopic quantities' deviation from the smoothed ones,

$$\begin{aligned} \delta\phi(\mathbf{x} + \mathbf{y}, \tau) &= \phi_{\text{mic}}(\mathbf{x} + \mathbf{y}, \tau) - \phi(\mathbf{x}, \tau) \\ \delta f(\mathbf{x} + \mathbf{y}, \tau) &= f_{\text{mic}}(\mathbf{x} + \mathbf{y}, \tau) - f(\mathbf{x}, \tau). \end{aligned} \quad (2.11)$$

The convolution term on the right hand side of eqn. (2.10) acts like a collision term if one interprets the equation as a Boltzmann equation. If it is rigorously taken into account, the term translates to a source of velocity dispersion in the second moment of eqn. (2.10) even if the absence of shell-crossing is assumed (Pietroni et al., 2012). To obtain the traditional starting point for Eulerian perturbation theory, we therefore have to neglect this term in the course of our consequent description. Assuming  $\delta f = \delta\phi = 0$  in the following leads us to the collision-less Boltzmann equation,

$$\left[ \frac{\partial}{\partial \tau} + \frac{p^i}{am} \frac{\partial}{\partial x^i} - am \nabla^i \phi(\mathbf{x}, \tau) \frac{\partial}{\partial p^i} \right] f(\mathbf{x}, \mathbf{p}, \tau) = 0. \quad (2.12)$$

This expression is also known as the Vlasov equation.

## 2.2. Fluid equations

For our calculations we first seek to obtain differential equations in real space, which represent our required fundamental theorems. In the first place, we impose conservation of matter. Since eqn. (2.12) was found by imposing particle number conservation in phase space, its integral over momentum will simply lead to the real space expression,

$$\frac{\partial}{\partial \tau} n = \nabla \cdot (n \mathbf{v}) = 0. \quad (2.13)$$

Here, we omit the obvious dependence of space and time ( $\mathbf{x}, \tau$ ) for notational clarity. Allowing different masses of particles the transition of the particle density to a mass density, i.e.  $n \rightarrow \rho$ , accounts for mass conservation,

$$\frac{\partial}{\partial \tau} \rho = \nabla \cdot (\rho \mathbf{v}) = 0. \quad (2.14)$$

Technically speaking the  $n^{\text{th}}$ -order moment of the Vlasov equation describes the dynamics of the  $n^{\text{th}}$ -order moment of the one particle distribution function  $f(\mathbf{x}, \mathbf{p}, \tau)$ . For  $n = 1$  this implies the dynamics for the velocity field,

$$\frac{\partial}{\partial \tau} \mathbf{v} + \mathcal{H} \mathbf{v} + (\mathbf{v} \cdot \nabla) \mathbf{v} = -\nabla \phi \quad (2.15)$$

Here, the Hubble function  $\mathcal{H}$  is the logarithmic derivative of the scale factor with respect to conformal time,  $\mathcal{H} = d \ln a / d\tau$ . In principle, we are - already at this point - confronted with a hierarchy of moments of the Vlasov equation describing physics on smaller and smaller scales with increasing order. However, the density regime of interest in our work covers small variations around the critical density (Smoot & Davidson, 1993),

$$\rho_{\text{crit}} = 5 \cdot 10^{-30} \frac{\text{g}}{\text{cm}^3}. \quad (2.16)$$

For this reason, shell-crossing is very unlikely and the assumption of  $\sigma_{\text{mic}} = 0$  holds with good accuracy. This truncates our system of dynamical quantities and we are left with closing the set of equations by imposing the  $r^{-1}$  dependence of gravitational potential via Poisson's equation in comoving coordinates

$$\nabla^2 \phi = \frac{4\pi G}{a} \rho. \quad (2.17)$$

The equations (2.14), (2.15) and (2.17) now build the basis of our description of structure formation and have to be modified for our specific systems of different types of matter.

In the later introduction of correlators it is useful to have quantities with a vanishing ensemble average. By construction of  $\mathbf{v}$  as the peculiar velocity field and of the potential  $\phi$  as the source of deviation from a background density in eqn. (2.4), these two fields already have zero mean. It is only natural to follow the relative deviation of density from a background field instead of the entire quantity itself,

$$\delta(\mathbf{x}) \equiv \frac{\rho(\mathbf{x}) - \bar{\rho}}{\bar{\rho}}. \quad (2.18)$$

In a matter dominated universe the Poisson equation (2.17) and the continuity equation (2.14) can then be rephrased as

$$\begin{aligned} \nabla^2 \phi &= \frac{3}{2} \mathcal{H}^2 \Omega_m \delta \\ 0 &= \frac{\partial}{\partial \tau} \delta + \nabla \cdot [(1 + \delta) \mathbf{v}]. \end{aligned} \quad (2.19)$$

One can now linearize the set of equations in order to find the linear solutions. If one is now exclusively interested in the evolution of the density contrast, one can combine the divergence of eqn. (2.15) and

the time derivative of the continuity equation in (2.19) with help of the Poisson equation to find the linear solution to be described by

$$\begin{aligned}\delta_L(\mathbf{x}, \tau) &= D(\tau) \delta_L(\mathbf{x}) \\ 0 &= \left( \partial_\tau^2 + \mathcal{H} \partial_\tau - \frac{3}{2} \mathcal{H}^2 \Omega_m \right) D(\tau).\end{aligned}\quad (2.20)$$

In case of a flat matter-dominated universe, the equation can be solved analytically. Due to its second order time derivative it has two solutions,

$$\begin{aligned}D_+(a) &= a \\ D_-(a) &= a^{-\frac{3}{2}}.\end{aligned}\quad (2.21)$$

The solutions  $D_+(a)$  and  $D_-(a)$  are called growing mode and decaying mode, respectively. All density perturbations having been initially in decaying mode  $D_-(a)$  will disappear rapidly and are subdominant after a short period of time. For this reason one often considers only the growing mode solution  $D_+(a)$  in linear initial conditions.

### 2.3. Gaussian random fields and ergodicity

In our statistical approach the initial conditions at a certain point  $\mathbf{x}$  - realizations of observables such as the density  $\rho_{\text{in}}(\mathbf{x})$  and velocity  $\mathbf{v}(\mathbf{x})$  - can be thought as drawn from an ensemble of universes. Once this realization has been performed our system is regarded as being described completely by deterministic Newtonian dynamics. The ensemble average of an observable  $A(\mathbf{x})$  at a fixed point in space  $\mathbf{x}$  will be the mean of all realizations  $A_i(\mathbf{x})$  in an ensemble of  $N$  universes,

$$\langle A(\mathbf{x}) \rangle = \lim_{N \rightarrow \infty} \frac{1}{N} \sum_i^N A_i(\mathbf{x}). \quad (2.22)$$

In the first place, this should not be confused with the average over a large volume  $V$  in space  $\mathbf{x}$  in a specific realization of the entire field  $A_{\text{spec}}(\mathbf{x})$  in one universe,

$$\bar{A} = \frac{1}{V} \int_V d\mathbf{x}^3 A_{\text{spec}}(\mathbf{x}). \quad (2.23)$$

Now, the ergodic hypothesis states that this spatial average in one specific realization of the field  $\bar{A}$  can be identified with the ensemble average at one fixed point  $\langle A(\mathbf{x}) \rangle$ ,

$$\bar{A} = \langle A(\mathbf{x}) \rangle \quad (2.24)$$

The relative deviation of the density from the mean density in eqn. (2.18) can then be written as

$$\delta(\mathbf{x}) = \frac{\rho(\mathbf{x}) - \bar{\rho}}{\bar{\rho}} = \frac{\rho(\mathbf{x}) - \langle \rho \rangle}{\langle \rho \rangle} \quad (2.25)$$

It is assumed that during inflation initial density conditions are produced, which are very close to Gaussian. For this reason and due to practical advantages, which will become clearer later, the choice of Gaussian initial conditions is widely established for studying the processes in structure formation. Assuming Gaussianity, the probability of finding the density contrast  $\delta_x$  at the position  $\mathbf{x}$  can be expressed as

$$p(\delta_x) d\delta_x = \frac{1}{\sqrt{2\pi \langle \delta_x^2 \rangle}} \exp \left[ -\frac{1}{2} \frac{\delta_x^2}{\langle \delta_x^2 \rangle} \right] d\delta_x \quad (2.26)$$

The probability of finding the values  $\delta_{x_1} \dots \delta_{x_m}$  at positions  $\mathbf{x}_1 \dots \mathbf{x}_m$  at the same time is then given by a multivariate Gaussian distribution,

$$p(\delta_{x_1}, \dots, \delta_{x_m}) d\delta_{x_1} \dots d\delta_{x_m} = \frac{1}{\sqrt{(2\pi)^m \det(Q)}} \exp\left[-\frac{1}{2} \delta_{x_i} (Q^{-1})_{ij} \delta_{x_j}\right] d\delta_{x_1} \dots d\delta_{x_m}, \quad (2.27)$$

where the width of the probability distribution is determined by the variance of the density  $\langle \delta_{x_i}^2 \rangle$  and its two point correlator  $\langle \delta_{x_i} \delta_{x_j} \rangle$  in the covariance matrix  $Q$ ,

$$Q = \begin{pmatrix} \langle \delta_{x_1} \delta_{x_1} \rangle & \dots & \langle \delta_{x_m} \delta_{x_1} \rangle \\ \vdots & \ddots & \vdots \\ \langle \delta_{x_1} \delta_{x_m} \rangle & \dots & \langle \delta_{x_m} \delta_{x_m} \rangle \end{pmatrix}. \quad (2.28)$$

By definition, the whole random field is described completely by its covariance matrix. For this reason the two-point correlator or its Fourier space analogon - the power spectrum - will be the quantities of main interest in our studies. The off-diagonal two-point correlator

$$\xi(\mathbf{x}_i, \mathbf{x}_j) = \langle \delta(\mathbf{x}_i) \delta(\mathbf{x}_j) \rangle \quad (2.29)$$

obtains a very intuitive interpretation. It indicates the random field's memory of the field at position  $\mathbf{x}_i$  with increasing distance  $|\mathbf{x}_i - \mathbf{x}_j|$ . With the help of the Cauchy-Schwarz inequality

$$\langle \delta(\mathbf{x}_i) \delta(\mathbf{x}_j) \rangle \leq \sqrt{\langle \delta^2(\mathbf{x}_i) \rangle \langle \delta^2(\mathbf{x}_j) \rangle}, \quad (2.30)$$

a rough estimate for this memory can be given in form of the so-called correlation coefficient  $r$ ,

$$r = \frac{\langle \delta(\mathbf{x}_i) \delta(\mathbf{x}_j) \rangle}{\sqrt{\langle \delta^2(\mathbf{x}_i) \rangle \langle \delta^2(\mathbf{x}_j) \rangle}}. \quad (2.31)$$

It runs from values of  $r = 0$  indicating independent measurements to values up to a maximum of  $r = 1$  implying fully correlated density values at the distance of  $|\mathbf{x}_i - \mathbf{x}_j|$ .

## 2.4. Homogeneity and isotropy

The fundamental assumptions of homogeneity and isotropy in our universe lead to interesting consequences for the Fourier transformed two-point function  $\xi(\mathbf{x}_1, \mathbf{x}_1 + \mathbf{x})$ . Since this argumentation is essential for the later understanding of the non-linear evolution, we will guide the reader through the few steps in detail.

First, we write the two-point function in Fourier space in terms of its single field Fourier transformations  $\delta(\mathbf{k})$ . Due to the linearity of the ensemble average and the integration one can write

$$\langle \delta(\mathbf{k}_1) \delta(\mathbf{k}) \rangle = \int \frac{d\mathbf{x}_1^3}{(2\pi)^3} \int \frac{d\mathbf{x}^3}{(2\pi)^3} \xi(\mathbf{x}_1, \mathbf{x}_1 + \mathbf{x}) e^{i(\mathbf{k}_1 + \mathbf{k}) \cdot \mathbf{x}_1} \cdot e^{i\mathbf{k} \cdot \mathbf{x}}. \quad (2.32)$$

Assuming homogeneity in the density field imposes the real space two-point function  $\xi(\mathbf{x}_1, \mathbf{x}_1 + \mathbf{x})$  to depend only on the relative vector  $\mathbf{x}$  between the two positions. Due to isotropy there must not be any directional dependence either,

$$\xi(\mathbf{x}_1, \mathbf{x}_1 + \mathbf{x}) = \xi(\mathbf{x}) = \xi(x). \quad (2.33)$$

Therefore, homogeneity forces the correlating wave vectors to be equal, since now the integration over  $\mathbf{x}_1$  can be translated to a Dirac  $\delta_D$ -function,

$$\begin{aligned} \langle \delta(\mathbf{k}_1) \delta(\mathbf{k}) \rangle &= \int \frac{d\mathbf{x}_1^3}{(2\pi)^3} \int \frac{d\mathbf{x}^3}{(2\pi)^3} \xi(x) e^{i(\mathbf{k}_1 + \mathbf{k}) \cdot \mathbf{x}_1} e^{i\mathbf{k} \cdot \mathbf{x}} \\ \langle \delta(\mathbf{k}_1) \delta(\mathbf{k}) \rangle &= \delta_D(\mathbf{k}_1 + \mathbf{k}) \int \frac{d\mathbf{x}^3}{(2\pi)^3} \xi(x) e^{i\mathbf{k} \cdot \mathbf{x}} \\ \langle \delta(\mathbf{k}_1) \delta(\mathbf{k}) \rangle &\equiv \delta_D(\mathbf{k}_1 + \mathbf{k}) P^k. \end{aligned} \quad (2.34)$$

In the last step the power spectrum  $P^k$  was defined as the Fourier transform of the two-point correlator  $\xi(x)$ . For later notational brevity in case of higher order correlators the  $k$ -dependence of the power spectrum was introduced as an upper index, which should not be mistaken for  $P$  to the power of  $k$ . The power spectrum formed from the linear solutions in eqn. (2.20) of the structure formation equations is called the linear power spectrum,

$$\langle \delta_L(\mathbf{k}_1) \delta_L(\mathbf{k}) \rangle = \delta_D(\mathbf{k}_1 + \mathbf{k}) P_L^k \equiv \delta_D(\mathbf{k}_1 + \mathbf{k}) P_L(k). \quad (2.35)$$

Physically, the power spectrum can be understood as the variance of the density contrast field at wave length  $\lambda = 2\pi/k$ . It is therefore a statistical measure for the strength of structure on different scales.

Going beyond Gaussianity, one has to consider higher order correlators. With the same argument of homogeneity, one will find analog definitions to be the most sensible. The next two higher order functions can then be written as

$$\begin{aligned} \xi(\mathbf{x}_2, \mathbf{x}_2 + \mathbf{x}_1, \mathbf{x}_2 + \mathbf{x}) &= \xi^{(3)}(\mathbf{x}_1, \mathbf{x}) \\ \xi(\mathbf{x}_3, \mathbf{x}_3 + \mathbf{x}_2, \mathbf{x}_3 + \mathbf{x}_1, \mathbf{x}_3 + \mathbf{x}) &= \xi^{(4)}(\mathbf{x}_2, \mathbf{x}_1, \mathbf{x}). \end{aligned} \quad (2.36)$$

With the definitions

$$\begin{aligned} B^{k,k_1} &= \int \frac{d\mathbf{x}^3}{(2\pi)^3} \int \frac{d\mathbf{x}_1^3}{(2\pi)^3} \xi^{(3)}(\mathbf{x}, \mathbf{x}_1) e^{i(\mathbf{k}\cdot\mathbf{x} + \mathbf{k}_1\cdot\mathbf{x}_1)} \\ Q^{k,k_1,k_2} &= \int \frac{d\mathbf{x}^3}{(2\pi)^3} \int \frac{d\mathbf{x}_1^3}{(2\pi)^3} \int \frac{d\mathbf{x}_2^3}{(2\pi)^3} \xi^{(4)}(\mathbf{x}, \mathbf{x}_1, \mathbf{x}_2) e^{i(\mathbf{k}\cdot\mathbf{x} + \mathbf{k}_1\cdot\mathbf{x}_1 + \mathbf{k}_2\cdot\mathbf{x}_2)} \end{aligned} \quad (2.37)$$

the bispectrum  $B^{k,k_1}$  and the four-point function  $Q^{k,k_1,k_2}$  are given in the following way,

$$\begin{aligned} \langle \delta(\mathbf{k}) \delta(\mathbf{k}_1) \delta(\mathbf{k}_2) \rangle &= \delta_D(\mathbf{k} + \mathbf{k}_1 + \mathbf{k}_2) B^{k,k_1} \\ \langle \delta(\mathbf{k}) \delta(\mathbf{k}_1) \delta(\mathbf{k}_2) \delta(\mathbf{k}_3) \rangle &= \delta_D(\mathbf{k} + \mathbf{k}_1 + \mathbf{k}_2 + \mathbf{k}_3) Q^{k,k_1,k_2}. \end{aligned} \quad (2.38)$$

## 2.5. Non-Gaussianities

In the case of a Gaussian random field with zero mean,  $\langle \delta_x \rangle = 0$ , the higher order correlators can be described by the power spectrum with help of Wick's theorem (see also Section A.1.1). Up to the four point correlator one finds

$$\langle \delta_{x_1} \delta_{x_2} \delta_{x_3} \rangle = 0 \quad (2.39)$$

$$\langle \delta_{x_1} \delta_{x_2} \delta_{x_3} \delta_{x_4} \rangle = \langle \delta_{x_1} \delta_{x_2} \rangle \langle \delta_{x_3} \delta_{x_4} \rangle + \langle \delta_{x_1} \delta_{x_3} \rangle \langle \delta_{x_2} \delta_{x_4} \rangle + \langle \delta_{x_1} \delta_{x_4} \rangle \langle \delta_{x_2} \delta_{x_3} \rangle. \quad (2.40)$$

In contrast to this, in presence of non-Gaussianity connected parts of correlators do not vanish and represent the deviation of the correlators away from Gaussianity

$$\langle \delta_{x_1} \delta_{x_2} \delta_{x_3} \rangle = \langle \delta_{x_1} \delta_{x_2} \delta_{x_3} \rangle_c \quad (2.41)$$

$$\begin{aligned} \langle \delta_{x_1} \delta_{x_2} \delta_{x_3} \delta_{x_4} \rangle &= \langle \delta_{x_1} \delta_{x_2} \rangle \langle \delta_{x_3} \delta_{x_4} \rangle + \langle \delta_{x_1} \delta_{x_3} \rangle \langle \delta_{x_2} \delta_{x_4} \rangle + \langle \delta_{x_1} \delta_{x_4} \rangle \langle \delta_{x_2} \delta_{x_3} \rangle \\ &\quad + \langle \delta_{x_1} \delta_{x_2} \delta_{x_3} \delta_{x_4} \rangle_c. \end{aligned} \quad (2.42)$$

The general definition of connected correlators can be found in Section A.1.2. The definitions are the same in other representations as for instance for the Fourier analogs. Since the three-point function is fully described by its own connected part, no new definition is needed here. However, in case of the four-point function, it is sensible to introduce a new quantity for the connected part. The trispectrum is defined as

$$\langle \delta(\mathbf{k}_1) \delta(\mathbf{k}_2) \delta(\mathbf{k}_3) \delta(\mathbf{k}_4) \rangle_c = \delta_D(\mathbf{k}_1 + \dots + \mathbf{k}_4) T^{k_1, k_2, k_3, k_4}, \quad (2.43)$$

which will be a very important quantity throughout this entire work.

## 2.6. Evolution in Fourier space

Any linear solution of partial differential equations will be scale invariant, which is due to the absence of any convolution terms in the Fourier representation. Besides this, differential operators can be transformed to algebraic factors by this technique. For these reasons, we will mainly work in Fourier space throughout this and the following chapters. This will also lead to an intuitive interpretation of the non-linear terms.

Due to Helmholtz's theorem the peculiar velocity can be split into the irrotational part ( $\nabla \times \mathbf{v}(\mathbf{x}) = 0$ ) and a divergence-free contribution ( $\nabla \cdot \mathbf{v}(\mathbf{x})$ ). However, one can argue that initial rotational modes of the peculiar velocity field should decay quickly and are only generated on very small scales (Pueblas & Scoccimarro, 2009). In the regime of interest one can therefore describe the velocity field explicitly in terms of its divergence,

$$\theta(\mathbf{x}) = \nabla \cdot \mathbf{v}(\mathbf{x}). \quad (2.44)$$

Using this definition, the divergence of eqn. (2.15) and eqn. (2.19) can now be combined and transformed to Fourier space to obtain (Bernardeau et al., 2002)

$$\begin{aligned} \frac{\partial}{\partial \tau} \delta(\mathbf{k}) + \theta(\mathbf{k}) &= -\delta_{\text{D}}(\mathbf{k} - \mathbf{k}_1 - \mathbf{k}_2) \alpha(\mathbf{k}_1, \mathbf{k}_2) \delta(\mathbf{k}_1) \theta(\mathbf{k}_2) \\ \frac{\partial}{\partial \tau} \theta(\mathbf{k}) + \mathcal{H} \theta(\mathbf{k}) + \frac{3}{2} \mathcal{H}^2 \Omega_{\text{m}} \theta(\mathbf{k}) &= -\delta_{\text{D}}(\mathbf{k} - \mathbf{k}_1 - \mathbf{k}_2) \beta(\mathbf{k}_1, \mathbf{k}_2) \theta(\mathbf{k}_1) \theta(\mathbf{k}_2), \end{aligned} \quad (2.45)$$

where integrations are implied over wave vectors, which are repeated in products, i.e.  $\mathbf{k}_1$  and  $\mathbf{k}_2$ . While the left hand sides of eqs. (2.45) represent the linear evolution of the fields, the right hand sides of both equations describe the non-linear mode-coupling of the structure formation determined by the time independent functions  $\alpha(\mathbf{k}_1, \mathbf{k}_2)$  and  $\beta(\mathbf{k}_1, \mathbf{k}_2)$ ,

$$\begin{aligned} \alpha(\mathbf{k}_1, \mathbf{k}_2) &= \frac{(\mathbf{k}_2 + \mathbf{k}_1) \cdot \mathbf{k}_1}{k_1^2} \\ \beta(\mathbf{k}_1, \mathbf{k}_2) &= \frac{(\mathbf{k}_2 + \mathbf{k}_1)^2 \mathbf{k}_2 \cdot \mathbf{k}_1}{2 k_1^2 k_2^2}. \end{aligned} \quad (2.46)$$

The real space analoga of the functions  $\alpha$  and  $\beta$  are  $\nabla \cdot (\delta \mathbf{v})$  and  $(\mathbf{v} \cdot \nabla) \mathbf{v}$ , respectively.

## 2.7. Perturbation theory

There are different possibilities to write down non-linear evolution and to sort the contributions into different orders with different interpretations. Here, we introduce two perturbative methods. Both sort the non-linear corrections in orders of the initial field configuration. While the standard perturbative approach separates the time evolution from the  $\mathbf{k}$ -dependence one can also use a Laplace transform to obtain an intuitive time integration representation of the corrections. However, the perturbative terms of the two approaches can be identified pairwise, which is fundamental for the argumentation in Chapter 3.

### 2.7.1. The standard approach

In order to describe non-Gaussianities in the density source field arising from the full non-linear evolution, a perturbative approach is introduced.

We employ non-linear solutions to the density field from standard perturbation theory (Sahni & Coles, 1995; Bernardeau et al., 2002). One expands the density contrast  $\delta(\mathbf{k}, a)$  and the velocity divergence  $\theta(\mathbf{k}, a)$  in  $n^{\text{th}}$  order perturbative contributions  $\delta^{(n)}(\mathbf{k})$  and  $\theta^{(n)}(\mathbf{k})$  which evolve differently in time. The latter can be written in terms of the perturbation theory kernels  $F^{(n)}(\mathbf{k}_1, \dots, \mathbf{k}_n)$  and

$G^{(n)}(\mathbf{k}_1, \dots, \mathbf{k}_n)$  as well as the initial linear fields  $\delta^{(1)}(\mathbf{k}) = \delta_L(\mathbf{k}, a = 1)$ . In a flat matter-dominated universe, i.e.  $\Omega_m = 1$ , one can accurately separate the time- from the  $\mathbf{k}$ -dependence and it is possible to write

$$\begin{aligned}\delta(\mathbf{k}, a) &= \sum_{n=1}^{\infty} a^n \delta^{(n)}(\mathbf{k}) \\ \theta(\mathbf{k}, a) &= -\mathcal{H}(a) \sum_{n=1}^{\infty} a^n \theta^{(n)}(\mathbf{k}).\end{aligned}\quad (2.47)$$

The  $n^{\text{th}}$  order modes are then given as

$$\begin{aligned}\delta^{(n)}(\mathbf{k}) &= \int d^3 q_1 \dots \int d^3 q_n \delta_D(\mathbf{k} - \mathbf{q}_{1\dots n}) \\ &\quad \times F^{(n)}(\mathbf{q}_1, \dots, \mathbf{q}_n) \delta^{(1)}(\mathbf{q}_1) \dots \delta^{(1)}(\mathbf{q}_n) \\ \theta^{(n)}(\mathbf{k}) &= \int d^3 q_1 \dots \int d^3 q_n \delta_D(\mathbf{k} - \mathbf{q}_{1\dots n}) \\ &\quad \times G^{(n)}(\mathbf{q}_1, \dots, \mathbf{q}_n) \delta^{(1)}(\mathbf{q}_1) \dots \delta^{(1)}(\mathbf{q}_n),\end{aligned}\quad (2.48)$$

with  $\mathbf{q}_{1\dots n} = \mathbf{q}_1 + \dots + \mathbf{q}_n$ . Inserting eqs. (2.47-2.48) into the evolution equations (2.45), one finds recursion relations for the kernels  $F^{(n)}(\mathbf{q}_1, \dots, \mathbf{q}_n)$  by combinatorics (Goroff et al., 1986; Jain & Bertschinger, 1994),

$$\begin{aligned}F^{(n)}(\mathbf{k}_1, \dots, \mathbf{k}_n) &= \sum_{m=1}^{n-1} \frac{G^{(m)}(\mathbf{k}_1, \dots, \mathbf{k}_m)}{(2n+1)(n-1)} \times \\ &\quad \left[ (2n+1) \alpha(\mathbf{q}_1, \mathbf{q}_2) F^{(n-m)}(\mathbf{k}_{m+1}, \dots, \mathbf{k}_n) + 2\beta(\mathbf{q}_1, \mathbf{q}_2) G^{(n-m)}(\mathbf{k}_{m+1}, \dots, \mathbf{k}_n) \right] \\ G^{(n)}(\mathbf{k}_1, \dots, \mathbf{k}_n) &= \sum_{m=1}^{n-1} \frac{G^{(m)}(\mathbf{k}_1, \dots, \mathbf{k}_m)}{(2n+1)(n-1)} \times \\ &\quad \left[ 3\alpha(\mathbf{q}_1, \mathbf{q}_2) F^{(n-m)}(\mathbf{k}_{m+1}, \dots, \mathbf{k}_n) + 2n G^{(n-m)}(\mathbf{k}_{m+1}, \dots, \mathbf{k}_n) \right],\end{aligned}\quad (2.49)$$

where  $\mathbf{q}_1 = \mathbf{k}_1 + \dots + \mathbf{k}_m$ ,  $\mathbf{q}_2 = \mathbf{k}_{m+1} + \dots + \mathbf{k}_n$  and  $F^{(1)} = G^{(1)} = 1$ . The explicit symmetrized expressions for the second order perturbation theory kernels take a very simple and intuitive form

$$\begin{aligned}F^{(2)}(\mathbf{k}_1, \mathbf{k}_2) &= \frac{5}{7} + \frac{1}{2} \frac{\mathbf{k}_1 \cdot \mathbf{k}_2}{k_1 k_2} \left( \frac{k_1}{k_2} + \frac{k_2}{k_1} \right) + \frac{2}{7} \frac{(\mathbf{k}_1 \cdot \mathbf{k}_2)^2}{k_1^2 k_2^2} \\ G^{(2)}(\mathbf{k}_1, \mathbf{k}_2) &= \frac{3}{7} + \frac{1}{2} \frac{\mathbf{k}_1 \cdot \mathbf{k}_2}{k_1 k_2} \left( \frac{k_1}{k_2} + \frac{k_2}{k_1} \right) + \frac{4}{7} \frac{(\mathbf{k}_1 \cdot \mathbf{k}_2)^2}{k_1^2 k_2^2}.\end{aligned}\quad (2.50)$$

One can see that mode-coupling to second order reaches its maximum when the contributing modes  $\mathbf{k}_1$  and  $\mathbf{k}_2$  are aligned, whereas the kernels vanish for anti-parallel modes. When in eqn. (2.48)  $n$  different modes  $\mathbf{q}_1 \dots \mathbf{q}_n$  contribute to a mode  $\mathbf{k}$ , momentum conservation holds, enforced by the  $\delta_D$ -distribution,  $\mathbf{k} = \mathbf{q}_1 + \dots + \mathbf{q}_n$ .

### 2.7.2. Approximate solution in $\Lambda$ CDM

In more general cosmologies, in particular those with dark energy, one has to employ the more general series ansatz

$$\begin{aligned}\delta(\mathbf{k}, a) &= \sum_{n=1}^{\infty} D_n \delta^{(n)}(\mathbf{k}) \\ \theta(\mathbf{k}, a) &= -\mathcal{H}(a) f_+(a) \sum_{n=1}^{\infty} E_n \theta^{(n)}(\mathbf{k}).\end{aligned}\quad (2.51)$$

Inserting eqs. (2.51) into the evolution eqs. (2.45), the  $n^{\text{th}}$  order contributions now have to obey the two following integro-differential equations,

$$\begin{aligned} \frac{dD_n}{d \ln D_1} \delta_n - E_n \theta_n &= \delta_D(\mathbf{k} - \mathbf{k}_{12}) \alpha(\mathbf{k}, \mathbf{k}_1) \\ &\times \sum_{m=1}^{n-1} D_{n-m} E_m \theta_m(\mathbf{k}_1) \delta_{n-m}(\mathbf{k}_2) \\ \frac{dE_n}{d \ln D_1} \theta_n + \left( \frac{3\Omega_m}{2f_+^2} - 1 \right) E_n \theta_n - \frac{3\Omega_m}{2f_+^2} D_n \delta_n &= \delta_D(\mathbf{k} - \mathbf{k}_{12}) \beta(\mathbf{k}, \mathbf{k}_1) \\ &\times \sum_{m=1}^{n-1} E_{n-m} E_m \theta_m(\mathbf{k}_1) \theta_{n-m}(\mathbf{k}_2), \end{aligned} \quad (2.52)$$

where integration over the wave vectors  $\mathbf{k}_1$  and  $\mathbf{k}_2$  is implied. However, also this system of equations becomes separable to any order, if we set

$$\begin{aligned} D_n &= E_n = D_+^n \\ f_+^2 &= \Omega_m, \end{aligned} \quad (2.53)$$

where the latter condition actually is not far from the good empirical approximation for flat cosmologies with only matter and vacuum energy (Bernardeau et al., 2002),

$$f_+ \approx \Omega_m^{5/9}, \quad (2.54)$$

as it is the case in the structure formation era of the  $\Lambda$ CDM universe. With this approximation, the eqs. (2.52) not only become separable but in fact reduce to the standard flat matter-dominated case and the spatial parts reduce to the contributions from eqs. (2.48) with the same kernels as from eqs. (2.49).

## 2.8. Matrix formulation

### 2.8.1. Matrix formulation in SCDM

To write the equations in a more compact form in a SCDM cosmology, we introduce the logarithmic time variable  $\eta$ , which explicitly contains the linear structure growth with respect to the scale factor,

$$\eta = \ln \left( \frac{a}{a_{\text{in}}} \right). \quad (2.55)$$

The fiducial scale  $a_{\text{in}}$  may be chosen at a time when the system could still be well approximated to be Gaussian and in the linear regime. A doublet field can be introduced for the density contrast  $\delta(\mathbf{k})$  and the divergence of the velocity dispersion  $\theta(\mathbf{k})$ ,

$$\begin{pmatrix} \varphi_1(\mathbf{k}) \\ \varphi_2(\mathbf{k}) \end{pmatrix} = e^{-\eta} \begin{pmatrix} \delta(\mathbf{k}) \\ -\theta(\mathbf{k})/\mathcal{H} \end{pmatrix}. \quad (2.56)$$

In a flat matter-dominated universe the factor  $e^{-\eta}$  now compensates for the linear evolution of the fields  $\varphi_i(\mathbf{k})$ . In other words, solving the linearized structure formation equations for these fields would lead to no time dependence in the doublet field at all. Therefore, any evolution away from the initial field doublet is explicitly due to non-linear effects. The set of equations (2.45) can now be expressed in a very compact form,

$$\partial_\eta \varphi_a(\mathbf{k}) = \Omega_{ab} \varphi_b(\mathbf{k}) + e^\eta \tilde{\gamma}_{abc}(\mathbf{k}, -\mathbf{q}, -\mathbf{p}) \varphi_b(\mathbf{q}) \varphi_c(\mathbf{p}). \quad (2.57)$$

Here, the linear evolution is governed by the matrix

$$\Omega_{ab} = \begin{pmatrix} 1 & -1 \\ -3/2 & 3/2 \end{pmatrix}, \quad (2.58)$$

while the non-linear mode-coupling is moderated by the vertex functions  $\tilde{\gamma}_{abc}(\mathbf{k}, \mathbf{q}, \mathbf{p})$ . The only non-vanishing vertex functions are

$$\begin{aligned} \tilde{\gamma}_{121}(\mathbf{k}, \mathbf{q}, \mathbf{p}) &= \tilde{\gamma}_{112}(\mathbf{k}, \mathbf{p}, \mathbf{q}) = \frac{1}{2} \delta_{\text{D}}(\mathbf{k} + \mathbf{q} + \mathbf{p}) \alpha(\mathbf{q}, \mathbf{p}), \\ \tilde{\gamma}_{222}(\mathbf{k}, \mathbf{q}, \mathbf{p}) &= \delta_{\text{D}}(\mathbf{k} + \mathbf{q} + \mathbf{p}) \beta(\mathbf{q}, \mathbf{p}). \end{aligned} \quad (2.59)$$

Since the vertex functions only appear in integrals, it is notationally convenient to introduce vertex functions, for which the  $\delta_{\text{D}}$ -function is already integrated out,

$$\gamma_{acb}^{k,q,|k+q|} \equiv \int d^3 p \tilde{\gamma}_{abc}(\mathbf{k}, \mathbf{q}, \mathbf{p}). \quad (2.60)$$

These quantities turn out to depend only on the absolute values of the wave vectors  $k, q$  and  $|\mathbf{k} + \mathbf{q}|$ .

### 2.8.2. The linear propagator in SCDM

Similar to the standard perturbative approach, also this formulation works only in case of a time independent matrix  $\Omega$ ,

$$\Omega_{ab}(\eta) = \Omega_{ab}, \quad (2.61)$$

which is equivalent to the condition

$$f^2(\eta) = \Omega_{\text{m}}(\eta). \quad (2.62)$$

Given this, the starting point of the argumentation are the compact structure formation equations (2.57). As so often, different choices of quantities have their own advantages depending on the application. For this calculation we absorb in the beginning the factor  $e^\eta$  into the fields on the right hand side of the equation saving the Laplace transform of this term,

$$\tilde{\varphi}_a(\mathbf{k}, \eta) = e^{\frac{\eta}{2}} \varphi_a(\mathbf{k}, \eta). \quad (2.63)$$

Shifting the linear evolution in eqs. (2.57) to the left hand side, we can write

$$\left( \partial_\eta \delta_{ab} - \Omega_{ab} \right) \varphi_b(\mathbf{k}, \eta) = \tilde{\gamma}_{abc}^{k,-q,-p} \tilde{\varphi}_b(\mathbf{q}, \eta) \tilde{\varphi}_c(\mathbf{p}, \eta). \quad (2.64)$$

Writing the fields as their inverse time Fourier transform (see Section C.2), we obtain

$$\begin{aligned} & - \int_0^\infty \frac{d\omega'}{2\pi} (i\omega \delta_{ab} + \Omega_{ab}) \varphi_b(\mathbf{k}, \omega') e^{-i\omega' \eta} \\ &= \tilde{\gamma}_{abc}^{k,-q,-p} \int_0^\infty \frac{d\omega'}{2\pi} \int_0^\infty \frac{d\omega''}{2\pi} \tilde{\varphi}_b(\mathbf{q}, \omega') \tilde{\varphi}_c(\mathbf{p}, \omega'') e^{-i(\omega' + \omega'') \eta}. \end{aligned} \quad (2.65)$$

Transforming this equation to frequency space yields

$$-(i\omega \delta_{ab} + \Omega_{ab}) \varphi_b(\mathbf{k}, \omega) = \tilde{\gamma}_{abc}^{k,-q,-p} \int_0^\infty \frac{d\omega'}{2\pi} \tilde{\varphi}_b(\mathbf{q}, \omega') \tilde{\varphi}_c(\mathbf{p}, \omega - \omega'). \quad (2.66)$$

The linear evolution has now been reduced to an algebraic operation. Introducing the inverse matrix  $\sigma_{ab}(\omega)$  via

$$(\sigma^{-1})_{ab}(\omega) = -(i\omega \delta_{ab} + \Omega_{ab}), \quad (2.67)$$

we can simply invert the linear time evolution,

$$\begin{aligned}
 \varphi_a(\mathbf{k}, \omega) &= \sigma_{ab}(\omega) \tilde{\gamma}_{bcd}^{k,-q,-p} \int_0^\infty \frac{d\omega'}{2\pi} \tilde{\varphi}_c(\mathbf{q}, \omega') \tilde{\varphi}_d(\mathbf{p}, \omega - \omega') \\
 &= \sigma_{ab}(\omega) \tilde{\gamma}_{bcd}^{k,-q,-p} \int_0^\eta d\eta' \int_0^{\eta'} d\eta'' \int_0^\infty \frac{d\omega'}{2\pi} \tilde{\varphi}_c(\mathbf{q}, \eta') \tilde{\varphi}_d(\mathbf{p}, \eta'') e^{i\omega'(\eta' - \eta'')} e^{i\omega\eta''} \\
 &= \sigma_{ab}(\omega) \tilde{\gamma}_{bcd}^{k,-q,-p} \int_0^\eta d\eta' \tilde{\varphi}_c(\mathbf{q}, \eta') \tilde{\varphi}_d(\mathbf{p}, \eta') e^{i\omega\eta'}.
 \end{aligned} \tag{2.68}$$

Now, we can transform the equation back to the time domain and resubstitute to our fields  $\varphi_a(\mathbf{k}, \eta)$  to find one particular solution of the inhomogeneous equation,

$$\varphi_a(\mathbf{k}, \eta) = \int_0^\eta d\eta' \tilde{g}_{ab}(\eta, \eta') \tilde{\gamma}_{bcd}^{k,-q,-p} \tilde{\varphi}_c(\mathbf{q}, \eta') e^{i\omega\eta'}, \tag{2.69}$$

where the linear operator  $\tilde{g}_{ab}(\eta, \eta')$  was defined as

$$\tilde{g}_{ab}(\eta, \eta') = \int_0^\infty \frac{d\omega}{2\pi} \sigma_{ab}(\omega) e^{-i\omega(\eta - \eta')} e^{i\omega\eta'}. \tag{2.70}$$

The full solution with an initial field  $\varphi_a^k(\eta_0)$  at time  $\eta_0$  as boundary condition can now be written as

$$\varphi_a(\mathbf{k}, \eta) = \tilde{g}_{ab}(\eta, \eta_0) \varphi_b^k(\eta_0) + \int_0^\eta d\eta' \tilde{g}_{ab}(\eta, \eta') \tilde{\gamma}_{bcd}^{k,-q,-p} \varphi_c(\mathbf{q}, \eta') \varphi_d(\mathbf{p}, \eta'). \tag{2.71}$$

The first term on the right hand side of eqn. (2.71) is the general solution of the linearized equations specified to the initial conditions  $\varphi_b^k(\eta_0)$  at initial time  $\eta_0$ , since it holds

$$(\partial_\eta \delta_{ab} - \Omega_{ab}) \tilde{g}_{bc}(\eta, \eta_0) = \delta_{ac} \delta_D(\eta - \eta_0). \tag{2.72}$$

One finds the linear equation

$$\varphi_{L,a}(\mathbf{k}, \eta) = \tilde{g}_{ab}(\eta, \eta_0) \varphi_{L,b}(\mathbf{k}, \eta_0), \tag{2.73}$$

which motivates the name linear propagator for  $\tilde{g}_{ab}$ . From eqn. (2.70),  $\tilde{g}_{ab}$  can be derived explicitly (Matarrese & Pietroni, 2007),

$$\tilde{g}_{ab}(\eta, \eta_0) = \left( \mathbf{B} + \mathbf{A} e^{-5/2(\eta - \eta_0)} \right)_{ab} \theta_H(\eta - \eta_0), \tag{2.74}$$

with the Heaviside step function  $\theta_H$  and the propagators  $\mathbf{B}$  and  $\mathbf{A}$  for growing and decaying mode, respectively,

$$\mathbf{B} = \frac{1}{5} \begin{pmatrix} 3 & 2 \\ 3 & 2 \end{pmatrix} \quad \text{and} \quad \mathbf{A} = \frac{1}{5} \begin{pmatrix} 2 & -2 \\ 3 & -3 \end{pmatrix}. \tag{2.75}$$

Initial conditions for growing mode ( $\varphi_a \propto \text{const}$ ) or decaying mode ( $\varphi_a \propto e^{5/2\eta}$ ) can then be selected by choosing

$$\varphi_a(\mathbf{k}, \eta) = u_a \varphi(\mathbf{k}) \quad \text{or} \quad \varphi_a(\mathbf{k}, \eta) = v_a \varphi(\mathbf{k}), \tag{2.76}$$

with

$$u_a = \begin{pmatrix} 1 \\ 1 \end{pmatrix} \quad \text{and} \quad v_a = \begin{pmatrix} 1 \\ -3/2 \end{pmatrix}. \tag{2.77}$$

### 2.8.3. The linear propagator for time dependent $\Omega_{ab}(\eta)$

For time dependent  $\Omega_{ab}(\eta)$  the procedure of the previous subsection does not succeed, since one obtains instead of eqn. (2.66)

$$- \int_0^\infty \frac{d\omega'}{2\pi} [i\omega' \delta_{ab} + \Omega_{ab}(\omega - \omega')] \varphi_b(\mathbf{k}, \omega') = \tilde{\gamma}_{abc}^{k,-q,-p} \int_0^\infty \frac{d\omega'}{2\pi} \tilde{\varphi}_b(\mathbf{q}, \omega') \tilde{\varphi}_c(\mathbf{p}, \omega - \omega'), \quad (2.78)$$

which can not be inverted in a simple algebraic way. Even though it is not possible to write the solution in a similar form as in eqn. (2.71) one can at least solve the linear part of the structure formation equations,

$$\partial_\eta \varphi_a(\mathbf{k}, \eta) = \Omega_{ab}(\eta) \varphi_b(\mathbf{k}, \eta). \quad (2.79)$$

The formalism presented in this subsection can be found in [Pietroni \(2008\)](#). Solutions to the linear structure formation equations are of the form

$$\begin{pmatrix} \varphi_1(\mathbf{k}, \eta) \\ \varphi_2(\mathbf{k}, \eta) \end{pmatrix} = \begin{pmatrix} 1 \\ f(\eta) \end{pmatrix} \varphi(\mathbf{k}, \eta). \quad (2.80)$$

Given this the two functions have to obey the following two equations,

$$\begin{aligned} \varphi(\mathbf{k}, \eta) &= \exp \left[ - \int_{\eta'}^\eta ds \left( \Omega_{11}(s) + \Omega_{12}(s) f(s) \right) \right] \varphi(\mathbf{k}, \eta') \\ f(\eta) \varphi(\mathbf{k}, \eta) &= \exp \left[ - \int_{\eta'}^\eta ds \left( \Omega_{21}(s)/f(s) + \Omega_{22}(s) \right) \right] f(\eta') \varphi(\mathbf{k}, \eta'). \end{aligned} \quad (2.81)$$

Identifying independent solutions as for instance starting in a flat matter dominated universe, one can set the initial conditions

$$f_\pm(\eta_{\text{in}}) = \bar{f}_\pm(\eta_{\text{in}}), \quad (2.82)$$

with

$$\bar{f}_\pm(\eta) = \frac{\Omega_{22} - \Omega_{11} \mp \sqrt{(\Omega_{22} - \Omega_{11})^2 + 4\Omega_{21}\Omega_{12}}}{2\Omega_{12}}. \quad (2.83)$$

Now, a linear propagator  $g_{ab}(\eta, \eta')$  can be defined,

$$\begin{aligned} g_{ab}(\eta, \eta') &= \exp \left[ - \int_{\eta'}^\eta ds \left( \Omega_{11}(s) + \Omega_{12}(s) f_+(s) \right) \right] \begin{pmatrix} 1 & 0 \\ 0 & \frac{f_+(\eta)}{f_+(\eta')} \end{pmatrix} \mathbf{M}_+(\eta') \\ &+ \exp \left[ - \int_{\eta'}^\eta ds \left( \Omega_{11}(s) + \Omega_{12}(s) f_-(s) \right) \right] \begin{pmatrix} 1 & 0 \\ 0 & \frac{f_-(\eta)}{f_-(\eta')} \end{pmatrix} \mathbf{M}_-(\eta'), \end{aligned} \quad (2.84)$$

relating the field  $\varphi_a(\mathbf{k}, \eta')$  at time  $\eta'$  to the field  $\varphi_a(\mathbf{k}, \eta)$  at time  $\eta$ ,

$$\varphi_a(\mathbf{k}, \eta) = g_{ab}(\eta, \eta') \varphi_b(\mathbf{k}, \eta'). \quad (2.85)$$

The projection matrices in  $\mathbf{M}_+(\eta)$  and  $\mathbf{M}_-(\eta)$  in eqn. (2.84) are the instantaneous projectors to the independent solutions and are defined by

$$\begin{aligned} \mathbf{M}(\eta) &= \frac{1}{f_- - f_+} \begin{pmatrix} f_- & -1 \\ f_- f_+ & -f_+ \end{pmatrix} \\ \mathbf{M}_- &= \mathbf{1} - \mathbf{M}_+(\eta). \end{aligned} \quad (2.86)$$

### 2.8.4. The n-point functions in perturbation theory

For an analytic expression of the perturbation theory  $n$ -point function one has to expand the fields in the correlator. Due to the assumed Gaussianity of the initial field  $\delta^{(1)}$  the correlators with an even number of fields  $\delta^{(1)}$  will later simplify to products of the initial power spectrum  $P_L^k$ , while all uneven contributions vanish,

$$\langle \delta_1 \dots \delta_n \rangle = \left\langle \sum_{i_1} D_+^{i_1} \delta_1^{(i_1)} \dots \sum_{i_n} D_+^{i_n} \delta_1^{(i_n)} \right\rangle. \quad (2.87)$$

For simplicity we use in this subsection the notation  $\delta_n \equiv \delta(\mathbf{k}_n)$ . Simple truncation of the expansion in eqn. (2.51) would lead to an inconsistent inclusion of powers of the linear power spectrum  $P_L^k$ . It is more sensible to take into account all terms up to a certain power  $m$  in the linear power spectrum, which is equivalent to including terms with initial fields up to powers  $2m$ .

In this work we exclusively use tree-level perturbation theory, i.e. no perturbative terms with inner momentum integrations are taken into account. Following this path, the density bispectrum  $B_\delta^{k_1, k_2, k_3}$  can be written as

$$B_\delta^{k_1, k_2, k_3} = 2 F^{(2)}(\mathbf{k}_1, \mathbf{k}_2) P_L^{k_1} P_L^{k_2} + \text{cyclic}\{1, 2, 3\}. \quad (2.88)$$

The non-Gaussian part of the 4-point function is the trispectrum  $T_\delta^{k_1, k_2, k_3, k_4}$ . It is convenient to split its tree-level expression into two parts.

The first contribution originates from second order perturbation theory. In this case, two of the fields in the correlator have been expanded to second order. The expressions in terms of the initial power spectra and the second order kernels are of the type

$$\begin{aligned} t^{(2)}((\mathbf{k}_1, \mathbf{k}_2), (\mathbf{k}_3, \mathbf{k}_4)) &= 4 D_+^6 P_L^{k_3} P_L^{k_4} \times \\ &\left( F^{(2)}(\mathbf{k}_{13}, -\mathbf{k}_3) F^{(2)}(\mathbf{k}_{24}, -\mathbf{k}_4) P_L^{k_{13}} \right. \\ &\left. + F^{(2)}(\mathbf{k}_{14}, -\mathbf{k}_4) F^{(2)}(\mathbf{k}_{23}, -\mathbf{k}_3) P_L^{k_{14}} \right). \end{aligned} \quad (2.89)$$

The second contribution is due to third order perturbation theory. Here, one field is expanded to third order while the other three remain at linear order. For this reason only one perturbation kernel appears in the expression for this type of contributions

$$t^{(3)}(\mathbf{k}_1, \mathbf{k}_2, \mathbf{k}_3, \mathbf{k}_4) = 6 D_+^6 F^{(3)}(\mathbf{k}_1, \mathbf{k}_2, \mathbf{k}_3) P_L^{k_1} P_L^{k_2} P_L^{k_3}. \quad (2.90)$$

With these two functions the connected perturbation theory four-point function up to third order in the linear power spectrum  $P_L^k$  can be expressed by the following two tree-level contributions,

$$\begin{aligned} T_\delta^{k_1, k_2, k_3, k_4} &= t^{(2)}((\mathbf{k}_1, \mathbf{k}_2), (\mathbf{k}_3, \mathbf{k}_4)) + \text{all pairs} \in \{1, 2, 3, 4\} \\ &+ t^{(3)}(\mathbf{k}_1, \mathbf{k}_2, \mathbf{k}_3, \mathbf{k}_4) + \text{cyclic}\{1, 2, 3, 4\}. \end{aligned} \quad (2.91)$$

The second order and the third order contributions of  $T_\delta$  have the same time dependence  $D_+^6$ .

### 2.8.5. Baryonic acoustic oscillations

Important features in the power spectrum  $P^k$  are signatures of baryonic acoustic oscillations of the Universe before recombination. The main constituents of the Universe - dark matter, photons and baryons - were in thermal equilibrium. Baryons attracted by dark matter overdensities were still tightly coupled to photons and felt their pressure as counteracting force leading to oscillations.

These oscillations induced ripples in the baryon-photon fluid which circularly propagated away from the source until the system decoupled. After decoupling the baryons did not feel the photon pressure any more and the waves were frozen up to a distance of  $c_s t_L$  from their origin, where  $c_s$  indicates the sound speed and  $t_L$  is the time of last scattering. In the following, gravitation was the

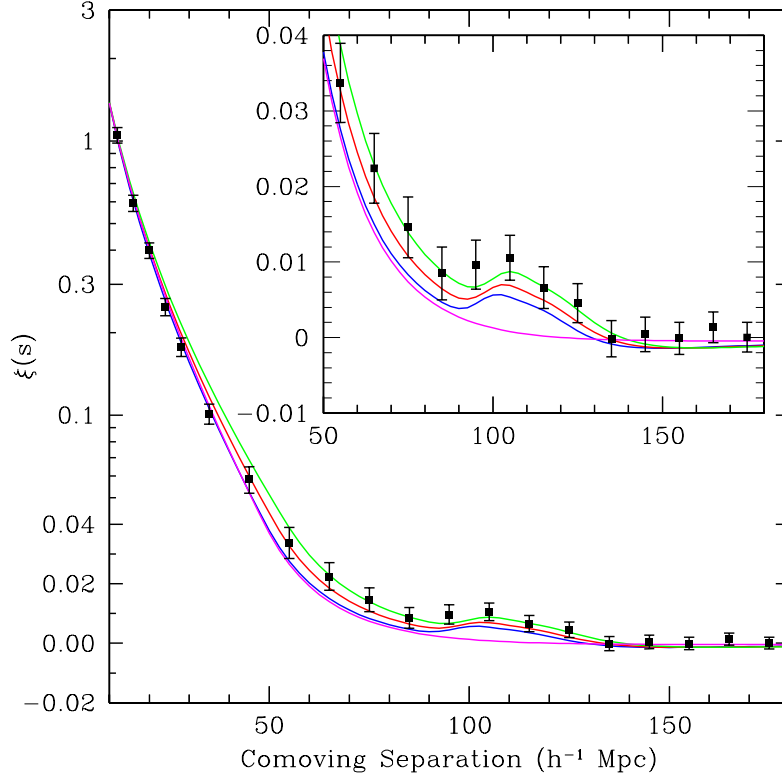


**Figure 2.1.:** Large-scale two-point galaxy correlation function from the SDSS LRG sample (dots). Shown are also the theoretical predictions for cosmological models with  $\Omega_m h^2 = 0.12$  (green line),  $\Omega_m h^2 = 0.13$  (red line) and  $\Omega_m h^2 = 0.13$  (blue line), all with  $\Omega_b h^2 = 0.024$ . Also a pure CDM model is shown in the plot (cyan line). The enhancement in the data at  $s \approx 100 h/\text{Mpc}$  was found to be significant. *Figure taken from Eisenstein et al. (2005).*

dominating force and dark matter started to trace the baryon density. In the two-point matter correlation function  $\xi(s)$  this leads to an increase, which can today be observed in galaxy surveys at a distance of  $s \approx 100 h/\text{Mpc}$ . This increase in correlation  $\xi(s)$  is shown in Fig 2.1. The SDSS data is shown in comparison to cosmological models with different values of  $\Omega_m h^2$  and a fixed value of  $\Omega_b h^2 = 0.024$ . Also the correlation function for a pure CDM universe is shown for comparison.

The evolution of the preferred correlation length with redshift contains valuable information about the expansion and acceleration history of the universe. The baryonic acoustic oscillations and their evolution have first been detected in the SDSS galaxy survey using spectroscopical redshifts (Eisenstein et al., 2005). In the power spectrum the acoustic peak translates to oscillatory features and their position and amplitude can be used as constraints on cosmological parameters.

# 3

## Chapter 3

---

# Perturbation theory trispectrum in the time renormalization group approach

An accurate theoretical description of structure formation at least in the mildly non-linear regime is essential for comparison with data from next generation galaxy surveys since most of the BAO and weak lensing signal is generated on non-linear scales. In a recent approach one follows the time evolution of correlators directly and finds a hierarchy of evolution equations with increasing order (Pietroni, 2008). So far, in this so called time renormalization group (TRG) method the trispectrum was neglected in order to obtain a closed set of equations. In this chapter we study the influence of the trispectrum on the evolution of the power spectrum. In order to keep the numerical cost at a manageable level we use the tree-level trispectrum from Eulerian perturbation theory. In comparison to numerical simulations we find improvement in the mildly non-linear regime up to  $k \simeq 0.25 h \text{ Mpc}^{-1}$ . Beyond  $k \simeq 0.25 h \text{ Mpc}^{-1}$  the perturbative description of the trispectrum fails and the method performs worse than without the trispectrum included. Our results reinforce the conceptual advantage of the time renormalization group method with respect to perturbation theory.

The contents of this chapter are published in Jürgens & Bartelmann (2012).

## 3.1. Introduction

In the contemporary picture of our Universe structures evolve from nearly Gaussian distributed small perturbations in the homogeneous density field. Sound waves formed in the coupled photon-baryon fluid before recombination left oscillatory features in the matter power spectrum, so called baryonic acoustic oscillations (BAO) (Eisenstein et al., 2005). Detections of this effect have become a valuable tool to constrain cosmological parameters since amplitude and position of the oscillations depend on the expansion history of the Universe (Eisenstein et al., 2005; Hütsi, 2006; Eisenstein et al., 2007; Padmanabhan et al., 2007; Blake et al., 2007). Current and upcoming galaxy surveys - such as BOSS<sup>4</sup>, WFIRST<sup>5</sup>, HETDEX (Hill et al., 2008) and WFMOS (Glazebrook et al., 2005) - will measure the power spectrum of the matter distribution to percent level accuracy in the region of the baryonic oscillations  $0.05 h \text{ Mpc}^{-1} < k < 0.25 h \text{ Mpc}^{-1}$  (Eisenstein et al., 1998; Seo & Eisenstein, 2003).

Since mode-coupling effects can significantly influence the position of the first peak at low redshifts (Croce & Scoccimarro, 2008), it is necessary to find a robust theoretical description of structure formation in the linear and mildly non-linear regime. While standard perturbation theory (Bernardeau et al., 2002) is a powerful tool for comparison with observations from galaxy surveys on large scales (Jeong & Komatsu, 2006, 2009), it breaks down at the scales of baryonic acoustic oscillations (Jain & Bertschinger, 1994).

---

<sup>4</sup><http://www.sdss3.org/surveys/boss.php>

<sup>5</sup><http://wfirst.gsfc.nasa.gov>

The increase of computational power and the efficiency of algorithms made  $N$ -body simulations the most established approach for structure formation (Springel, 2005; Huff et al., 2007; Heitmann et al., 2008; Takahashi et al., 2008; Evrard et al., 2008; Heitmann et al., 2010). However, to extract statistical information from numerical simulations, either large sets of initial conditions or large volumes are needed and it is difficult to control measurement uncertainties in the mildly non-linear regime (Angulo et al., 2008). In a recent work a simple physically motivated picture was used to reduce the sample variance to speed up the scanning for cosmological parameters with  $N$ -body simulations (Tassev & Zaldarriaga, 2011), but it remains a numerically expensive tool to predict non-linear structure formation. In contrast to numerical simulations, semi-analytical techniques are often faster and thus offer the possibility to study a wider range of models.

While the halo model approach (Peacock & Dodds, 1996; Smith et al., 2003) was found to be incapable of reaching the required accuracy (Huff et al., 2007), different attempts to include corrections of specific types to all orders at the same time have been presented over the last years. Field theoretical techniques motivated by the renormalization group (Matarrese & Pietroni, 2007, 2008; Anselmi et al., 2011b) and resummation methods (Croce & Scoccimarro, 2006a,b) improved the results for power spectra in the mildly non-linear regime significantly down to  $z = 0$  in comparison to  $N$ -body simulations. In the following also higher order statistics were studied in these frameworks (Valageas, 2008; Bernardeau et al., 2008; Guo & Jing, 2009). However, these approaches are formulated for an Einstein-de Sitter cosmology and are later generalized to other cosmologies by substituting the respective growth function. The accuracy of this approximation is hard to quantify at higher orders (Bernardeau et al., 2002).

Cross-correlating the fields to all powers with the time derivative of a field using the structure formation equations, leads to an infinite hierarchy of evolution equations for field correlators of all orders (Pietroni, 2008). This formalism of following the time evolution of correlators directly became known as time renormalization group method. The hierarchy - similar to the well known BBGKY hierarchy (Peebles, 1980) - was truncated at the level of the trispectrum to obtain a closed set of equations (Pietroni, 2008). The method can easily be generalized to a large set of different cosmologies including models with scale dependent growth functions. For example, this is important in the case of massive neutrinos (Lesgourgues & Pastor, 2006) which was also studied within this framework (Lesgourgues et al., 2009). However, recent studies showed that results strongly depend on initial conditions for the bispectrum (Audren & Lesgourgues, 2011) and show only little improvement with respect to the 1-loop results from perturbation theory.

The objective of this work is to study the effect of the trispectrum on the TRG approach. Including the entire time evolution of the trispectrum would lead to an immoderate numerical effort. We therefore include the tree-level trispectrum from perturbation theory into the evolution equation of the bispectrum and study its effects on the power spectrum in the BAO regime. We work in a standard  $\Lambda$ CDM cosmology ( $\Omega_m = 0.25$ ,  $\Omega_b h^2 = 0.0224$ ,  $h = 0.72$ ,  $n = 0.97$  and  $\sigma_8 = 0.8$ ) which we chose for a consistent comparison with power spectra obtained from  $N$ -body simulations (Carlson et al., 2009).

The chapter is organized as follows: In Section 3.2 we review the time renormalization approach introduced by Pietroni (2008). How the perturbation theory trispectrum can be included into this method will be subject of Section 3.3. In Section 3.4 we include the trispectrum into the formal analytic solution of the system and discuss the additional corrections in a diagrammatic representation and in Section 3.5 our numerical results and their comparisons to  $N$ -body simulations are presented. The results are summarized and discussed in Section 3.7.

## 3.2. Time renormalization

In this section we write the structure formation equations in a compact matrix form and review the time renormalization approach (Pietroni, 2008) as a starting point for our further calculations. We will concentrate on spatially flat cosmologies with a dark matter component and a non-clustering dark

energy fluid or  $\Lambda$ CDM. However, this method can be easily extended to more exotic cosmologies including such cosmologies with a scale-dependent growth function  $D_+(k, a)$  (Pietroni, 2008).

### 3.2.1. Structure formation in more general cosmologies

In Section 2.6 we introduced the fundamental equations of structure formation in a very compact form. However, the presented formulation is only valid for a one-component fluid cosmology, as for instance during matter domination. To open the description to a slightly wider and more authentic range of models only a few transformations are required.

In the case of a one-component dark matter fluid we have  $\Omega_m = 1$ . During the time of dark matter structure formation the two predominant energy constituents in the  $\Lambda$ CDM cosmology are given by dark matter and dark energy. Assuming a non-interacting dark energy fluid with a constant equation of state we only have to replace  $\Omega_m$  in eqn. (2.45) by

$$\begin{aligned}\Omega_m &\rightarrow \left[ 1 + \frac{\rho_{\Lambda 0}}{\rho_{m 0}} a^{-3w} \right]^{-1} \\ \eta &\rightarrow \ln \left[ \frac{D_+(a)}{D_+(a_{\text{in}})} \right] \\ \varphi_2 &\rightarrow -\frac{\theta}{\mathcal{H} f_+} \\ \Omega_{ab} &\rightarrow \begin{pmatrix} 1 & -1 \\ -\frac{3}{2} \frac{\Omega_m}{f_+^2} & \frac{3}{2} \frac{\Omega_m}{f_+^2} \end{pmatrix},\end{aligned}\tag{3.1}$$

which is shown in more detail in Section A.2. The quantities  $\rho_{\Lambda 0}$  and  $\rho_{m 0}$  represent the background densities today of the dark energy and dark matter fluid components, respectively.  $w$  denotes the equation of state parameter of the dark energy fluid,  $p_\Lambda = w\rho_\Lambda$ . Models with a cosmological constant, as for example in  $\Lambda$ CDM, can then simply be described by  $w = -1$ . For the one-component dark matter fluid one simply has to set  $\rho_{\Lambda 0} = 0$  and all quantities return automatically to the previous description.

The scale factor  $a_{\text{in}}$  may be chosen at a time when the system could still be well approximated to be Gaussian and in the linear regime. Here,  $f_+$  is the logarithmic derivative of the growth function  $D_+$  with respect to the scale factor  $a$ ,  $f_+ = d \ln D_+ / d \ln a$ . The factor  $e^{-\eta}$  now compensates for the linear evolution of the fields  $\varphi_i(\mathbf{k})$ . In other words, solving the linearized structure formation equations for these fields would lead to no time dependence in the doublet field at all. Therefore, any evolution away from the initial field doublet is explicitly due to non-linear effects. The set of equations (2.45) can now still be expressed in the same compact form as before,

$$\partial_\eta \varphi_a(\mathbf{k}) = \Omega_{ab} \varphi_b(\mathbf{k}) + e^\eta \tilde{\gamma}_{abc}(\mathbf{k}, -\mathbf{q}, -\mathbf{p}) \varphi_b(\mathbf{q}) \varphi_c(\mathbf{p}).\tag{3.2}$$

The time independent vertex functions  $\tilde{\gamma}_{abc}(\mathbf{k}, \mathbf{q}, \mathbf{p})$  are completely unaffected by the transformation in eqn. (3.1). They remain the same as in eqn. (2.59).

### 3.2.2. Hierarchy of correlators

While in standard perturbation theory one aims to solve the evolution equations of the fields themselves, in the time renormalization approach one formulates evolution equations directly for the final quantities of interest - the correlators of the fields. In order to do this, one can use eqn. (3.2) to write down a hierarchy of evolution equations for correlators of any order:

$$\begin{aligned}\partial_\eta \langle \varphi_a \varphi_b \rangle &= -\Omega_{ac} \langle \varphi_c \varphi_b \rangle - \Omega_{bc} \langle \varphi_a \varphi_c \rangle + e^\eta [\tilde{\gamma}_{acd} \langle \varphi_c \varphi_d \varphi_b \rangle + \tilde{\gamma}_{bcd} \langle \varphi_a \varphi_c \varphi_d \rangle] \\ \partial_\eta \langle \varphi_a \varphi_b \varphi_c \rangle &= -\Omega_{ad} \langle \varphi_d \varphi_b \varphi_c \rangle + \text{cyclic} \{a, b, c\} + e^\eta [\tilde{\gamma}_{ade} \langle \varphi_d \varphi_e \varphi_b \varphi_c \rangle + \text{cyclic} \{a, b, c\}] \\ \partial_\eta \langle \varphi_a \varphi_b \varphi_c \varphi_d \rangle &= \dots\end{aligned}\tag{3.3}$$

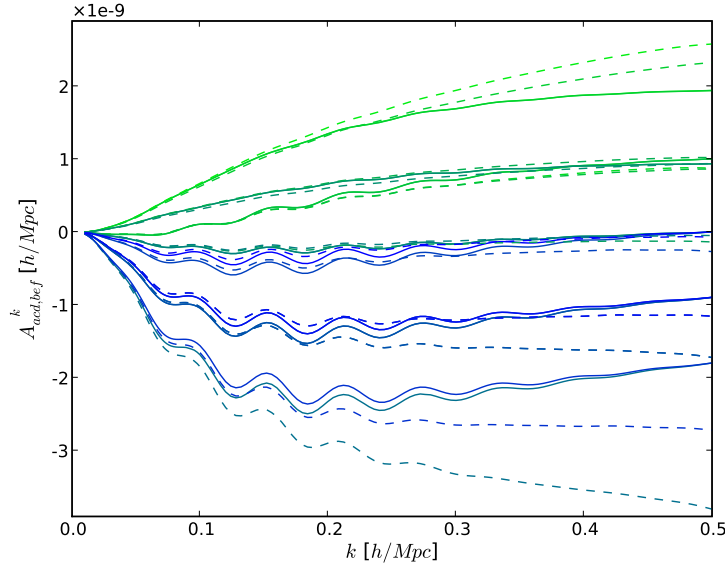


**Figure 3.1.:** The correction integrals  $A_{acd,bef}^k$  are depicted here. Ordering the indices  $acdbef$  as if they were increasing binary numbers, the non-vanishing integrals are shown from  $(acd, bef) = (001, 000)$  (green) up to  $(acd, bef) = (111, 111)$  (blue). One can observe the evolution from initial redshift  $z = 100$  (solid lines) to  $z = 1$  (dashed lines). Initially degenerate integrals split up due to non-linear evolution.

Here and in the following, we abbreviate the doublet field index  $a_1$  and the wave vector  $\mathbf{k}_1$  to a single number index, i.e.  $\varphi_1 \equiv \varphi_{a_1}(\mathbf{k}_1)$ . As a natural property of this hierarchy, for the evolution of a correlator of order  $n$  the knowledge of correlators of the next higher order  $n+1$  is needed. Therefore, one is obliged to truncate this hierarchy at a certain point in order to obtain a closed set of equations. Splitting up the four-point correlator into its connected and unconnected parts yields by Wick's theorem

$$\langle \varphi_1 \varphi_2 \varphi_3 \varphi_4 \rangle = \langle \varphi_1 \varphi_2 \varphi_3 \varphi_4 \rangle_c + \langle \varphi_1 \varphi_2 \rangle \langle \varphi_3 \varphi_4 \rangle + \langle \varphi_1 \varphi_3 \rangle \langle \varphi_2 \varphi_4 \rangle + \langle \varphi_1 \varphi_4 \rangle \langle \varphi_2 \varphi_3 \rangle. \quad (3.4)$$

For instance, one can close the system by neglecting the connected part of the four-point correlator, as done by [Pietroni \(2008\)](#). Due to this approximation, one is left with the first two equations of the hierarchy and the simplified system is then fully described by its power spectra  $P_{ab}^k$  and its bispectra  $B_{abc}^{k_1, k_2, k_3}$

$$\begin{aligned} \langle \varphi_1 \varphi_2 \rangle &= \delta_D(\mathbf{k}_1 + \mathbf{k}_2) P_{ab}^{k_1} \\ \langle \varphi_1 \varphi_2 \varphi_3 \rangle &= \delta_D(\mathbf{k}_1 + \mathbf{k}_2 + \mathbf{k}_3) B_{abc}^{k_1, k_2, k_3}. \end{aligned} \quad (3.5)$$

Due to isotropy the bispectrum will only depend on the absolute values of the wave vectors. Integrating eqn. (3.3) over one wave vector and using eqn. (3.4) with  $\langle \varphi_1 \varphi_2 \varphi_3 \varphi_4 \rangle_c = 0$  one finds a closed system of equations in which the four-point function is represented in terms of power spectra  $P_{ab}^k$ :

$$\begin{aligned} \partial_\eta P_{ab}^k &= -\Omega_{ac} P_{cb}^k - \Omega_{bc} P_{ac}^k + e^\eta \int d^3 q \left[ \gamma_{acd}^{k, q, p} B_{bcd}^{k, q, p} + (a \leftrightarrow b) \right] \\ \partial_\eta B_{abc}^{k, q, p} &= -\Omega_{ad} B_{dbc}^{k, q, p} - \Omega_{bd} B_{adc}^{k, q, p} - \Omega_{cd} B_{abd}^{k, q, p} \\ &\quad + 2 e^\eta \left[ \gamma_{ade}^{k, q, p} P_{db}^q P_{ec}^p + \gamma_{bde}^{q, p, k} P_{dc}^p P_{ea}^k + \gamma_{cde}^{p, k, q} P_{da}^k P_{eb}^q \right]. \end{aligned} \quad (3.6)$$

Here and in the following  $\mathbf{p}$  will denote the vector  $\mathbf{p} = -(\mathbf{k} + \mathbf{q})$ . How this system can be solved numerically will be the subject of the next subsection.

### 3.2.3. Solving the closed system

Formal and numerical solutions to the closed system in eqn. (3.6) have already been presented (Pietroni, 2008). We follow the same numerical path to investigate the solution's sensitivity to the perturbation theory trispectrum. Since we are mainly interested in the evolution of the power spectrum itself, one circumvents the necessity of tracking the total bispectrum by introducing auxiliary integrals,

$$I_{acd,bef}^k \equiv \frac{k}{4\pi} \int d^3q \frac{1}{2} \left[ \gamma_{acd}^{k,q,p} B_{bef}^{k,q,p} + (q \leftrightarrow p) \right]. \quad (3.7)$$

The introduction of these integrals encapsulates the one loop character of the power spectrum evolution equation (first equation in (3.6)), which numerically simplifies to the tree level equation

$$\partial_\eta P_{ab}^k = -\Omega_{ac} P_{cb}^k - \Omega_{bc} P_{ab}^k + e^\eta \frac{4\pi}{k} \left[ I_{acd,bcd}^k + I_{bcd,acd}^k \right]. \quad (3.8)$$

Differentiating the integrals  $I_{acd,bef}^k$  with respect to time  $\eta$  and using the evolution equation of the bispectrum from eqn. (3.6) gives the following time evolution of these integrals,

$$\partial_\eta I_{acd,bef}^k = -\Omega_{bg} I_{acd,gef}^k - \Omega_{eg} I_{acd,bgf}^k - \Omega_{fg} I_{acd,beg}^k + 2 e^\eta A_{acd,bef}^k. \quad (3.9)$$

The  $k$ -space loop integral which was originally in the evolution of the power spectrum now appears in the mode-coupling integrals  $A_{acd,bef}^k$ , which initially drive the system away from Gaussianity,

$$A_{acd,bef}^k = \frac{k}{4\pi} \int d^3q \frac{1}{2} \left[ \gamma_{acd}^{k,q,p} \left( \gamma_{bgh}^{k,q,p} P_{ge}^q P_{hf}^p + \gamma_{egh}^{q,p,k} P_{gf}^p P_{hb}^k + \gamma_{fgh}^{p,k,q} P_{gb}^k P_{hb}^q \right) + (q \leftrightarrow p) \right]. \quad (3.10)$$

The calculation of the integrals  $A_{acd,bef}^k$  is so far the only time consuming task in numerically solving the system.

In Fig. 3.1 the non-vanishing correction integrals are depicted for initial redshift  $z = 100$  and redshift  $z = 1$ , ordered with increasing binary number  $acdbef$  from  $(acd, bef) = (001, 000)$  (green) up to  $(acd, bef) = (111, 111)$  (blue). One can observe, that some initially degenerate integrals split up in the course of non-linear evolution. The correction integrals in units of a smooth linear power spectrum  $P_{L,nw}^k$  are shown in Fig. 3.2. In this representation, the increase of non-linear growth on small scales is obvious. Furthermore, one can observe that many integrals are of the same size and therefore many terms cancel in eqn. (3.9) due to  $\Omega_{i0} = -\Omega_{i1}$ .

### 3.2.4. Initial conditions and symmetries

We propagate the system of equations (3.8)-(3.9) forward in time starting from an initial time at which the dynamics of the fields could still be well approximated by the linearized evolution equations. As initial redshift we choose  $z_{in} = 100$  and start with linear growing mode initial conditions,

$$\begin{aligned} \varphi_{a,L}(\mathbf{k}, \eta = 0) &\equiv u_a \varphi(\mathbf{k}) \quad , \quad (u_1, u_2) = (1, 1) \\ \delta_D(\mathbf{k} + \mathbf{k}') P_{ab}^k(\eta = 0) &= \delta_D(\mathbf{k} + \mathbf{k}') u_a u_b P_L^k(\eta = 0) = u_a u_b \langle \varphi(\mathbf{k}) \varphi(\mathbf{k}') \rangle. \end{aligned} \quad (3.11)$$

Furthermore, we will assume Gaussian initial conditions. This implies a vanishing initial bispectrum  $B_{abc}^{k,q,p}$  and therefore also vanishing initial integrals  $I_{acd,bef}^k$ ,

$$I_{acd,bef}^k(\eta = 0) = B_{abc}^{k,q,p}(\eta = 0) = 0. \quad (3.12)$$

Following the next arguments, the full system of 64 integrals  $I_{acd,bef}^k$  and 3 power spectra  $P_{ab}^k$  can be reduced to 14 independent components. Since the only non-vanishing vertex contributions appear for the index triples  $(acd) \in \{(112), (121), (222)\}$  only the integrand  $I_{acd,bef}^k$  with these triples will evolve

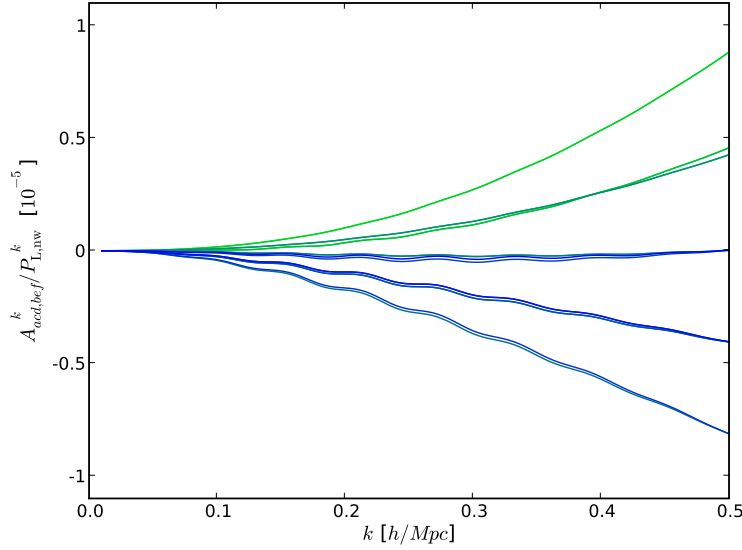


**Figure 3.2.:** The correction integrals  $A_{acd,bef}^k$  are depicted here in units of a smooth linear power spectrum  $P_{L,nw}^k$  (Eisenstein et al., 1998). Ordering the indices  $acdbef$  as if they were increasing binary numbers, the non-vanishing integrals are shown from  $(acd, bef) = (001, 000)$  (green) up to  $(acd, bef) = (111, 111)$  (blue). It is likely, that many terms in eqn. (3.9) will nearly cancel due to  $\Omega_{i0} = -\Omega_{i1}$ .

away from zero, which can be seen from equations (3.9)-(3.10). The remaining 24 components can be further reduced by symmetry arguments. Using the following symmetries in the vertex functions and the bispectrum

$$\gamma_{acd}^{k,q,p} = \gamma_{adc}^{k,p,q}, \quad B_{bef}^{k,q,p} = B_{bfe}^{k,p,q}, \quad (3.13)$$

we can find the following symmetry for the integrals  $I_{acd,bef}^k$ ,

$$I_{acd,bef}^k = I_{adc,bfe}^k. \quad (3.14)$$

Due to this symmetry, only 14 independent integrals remain to be followed. The independent integrals are identified by the direct product of  $(acd) = (112)$  and  $(bef) = (b11), (b12), (b21)$  and  $(b22)$ , ( $b = 1, 2$ ), and the direct product of  $(acd) = (222)$  and  $(bef) = (b11), (b12)$  and  $(b22)$ , ( $b = 1, 2$ ). Including the 3 independent power spectra  $P_{11}^k$ ,  $P_{12}^k$  and  $P_{22}^k$  implies a system of 17 components in total.

### 3.3. Trispectrum

The connected part<sup>6</sup> of the four-point correlator is called the trispectrum<sup>7</sup>. To investigate the method's sensitivity with respect to the trispectrum, we include the perturbation theory trispectrum to third order in the linear power spectrum  $P_L^k$ . Including the full time evolution of the non-perturbative trispectrum would increase the numerical effort disproportionately. This would be given by the third equation in the hierarchy of time evolution equations for correlators in eqn. (3.3). However, the time evolution of the tree-level perturbation theory trispectrum is exclusively given in terms of the growth function  $D_+(a)/D_+(a_{in}) = e^{\eta}$ . Therefore, using this approximation for the trispectrum it is sufficient to compute trispectrum corrections at the initial time  $a_{in}$ , whose time dependence is then determined by the growth factor only. These corrections can then be included into the routine without increasing the computational cost significantly.

<sup>6</sup>The connected parts of correlators are defined in Appendix A.1.2.

<sup>7</sup>See Section 2.8.4 for the definition of the pure density trispectrum.

### 3.3.1. Compact perturbation theory

In the following, we adapt standard perturbation theory <sup>8</sup> (Bernardeau et al., 2002) to the compact matrix formulation of structure formation. We expand the fields  $\varphi_a(\mathbf{k}, \eta)$  in  $n^{\text{th}}$  order perturbative contributions  $\varphi_a^{(n)}(\mathbf{k}, \eta)$ , which can be written in terms of the perturbation theory kernels  $F_a^{(n)}(\mathbf{k}_1, \dots, \mathbf{k}_n)$  and the initial linear fields  $\varphi_a^{(1)}(\mathbf{k}) = \varphi_{L,a}(\mathbf{k}, \eta = 0)$ :

$$\varphi_a(\mathbf{k}, \eta) = \sum_{n=1}^{\infty} e^{(n-1)\eta} \varphi_a^{(n)}(\mathbf{k}) \quad (3.15)$$

$$\varphi_a^{(n)}(\mathbf{k}) = \int d^3 q_1 \dots \int d^3 q_n \delta_{\text{D}}(\mathbf{k} - \mathbf{q}_{1\dots n}) F_a^{(n)}(\mathbf{q}_1, \dots, \mathbf{q}_n) \varphi_a^{(1)}(\mathbf{q}_1) \dots \varphi_a^{(1)}(\mathbf{q}_n) \quad (3.16)$$

with  $\mathbf{q}_{1\dots n} = \mathbf{q}_1 + \dots + \mathbf{q}_n$ . For this formulation, one has to drop the time dependence of  $\Omega_{ab}$  from eqn. (2.58) to obtain separability of the structure formation equations. However, the required relation  $f_+ = \Omega_{\text{m}}^{1/2}$  represents a good approximation in cosmologies close to  $\Lambda$ CDM (Bernardeau et al., 2002; Pietroni, 2008). For notational simplicity we combined the two standard kernels of each order into a vector, since we will also need trispectrum correlations to the velocity field components,

$$F_a^{(n)}(\mathbf{k}_1, \dots, \mathbf{k}_n) = \begin{pmatrix} F^{(n)}(\mathbf{k}_1, \dots, \mathbf{k}_n) \\ G^{(n)}(\mathbf{k}_1, \dots, \mathbf{k}_n) \end{pmatrix}, \quad (3.17)$$

with the standard perturbation theory kernels as they were defined in eqn. (2.48). When in eqn. (3.16)  $n$  different modes  $\mathbf{q}_1 \dots \mathbf{q}_n$  contribute to a mode  $\mathbf{k}$ , momentum conservation holds, enforced by the  $\delta_{\text{D}}$ -distribution:  $\mathbf{k} = \mathbf{q}_1 + \dots + \mathbf{q}_n$ . Similar to the renormalization vertex in eqn. (2.59), the last results also motivate a diagrammatic description for the mode coupling processes (see Fig. 3.3).

### 3.3.2. The four-point correlator in perturbation theory

For an analytic expression of the perturbation theory four-point correlator one has to expand the fields in the correlator. Due to the Gaussianity of the initial fields  $\varphi^{(1)}$  the correlators with an even number of fields  $\varphi^{(1)}$  will later simplify to products of initial power spectra  $P_{\text{L}}$  while all uneven contributions vanish ,

$$\langle \varphi_1 \varphi_2 \varphi_3 \varphi_4 \rangle = \langle (\varphi_1^{(1)} + e^\eta \varphi_1^{(2)} + \dots) (\varphi_2^{(1)} + e^\eta \varphi_2^{(2)} + \dots) (\varphi_3^{(1)} + e^\eta \varphi_3^{(2)} + \dots) (\varphi_4^{(1)} + e^\eta \varphi_4^{(2)} + \dots) \rangle. \quad (3.18)$$

Simple truncation of the expansion in eqn. (3.15) would lead to an inconsistent inclusion of powers of the linear power spectrum  $P_{\text{L}}^k$ . We take into account all terms up to third order in the linear power spectrum which is equivalent to including terms with initial fields up to sixth order. Since the disconnected part will be represented by the full power spectra in eqn. (3.4), we are interested in the connected part of the correlator only. The connected part can be split into two contributions

$$\begin{aligned} \langle \varphi_1 \varphi_2 \varphi_3 \varphi_4 \rangle_{\text{c}} &= \langle (\varphi_1^{(2)} \varphi_2^{(2)}) (\varphi_3^{(1)} \varphi_4^{(1)}) \rangle_{\text{c}} + \text{all pairs } \in \{1, 2, 3, 4\} \\ &+ \langle \varphi_1^{(3)} \varphi_2^{(1)} \varphi_3^{(1)} \varphi_4^{(1)} \rangle_{\text{c}} + \text{cyclic } \{1, 2, 3, 4\}. \end{aligned} \quad (3.19)$$

The first contribution originates from second order perturbation theory. In this case two of the fields in the correlator have been expanded to second order. The expressions in terms of the initial power spectra and the second order kernels are of the type

$$\begin{aligned} t_{a_1 a_2}^{(2)}((\mathbf{k}_1, \mathbf{k}_2), (\mathbf{k}_3, \mathbf{k}_4)) &= 4 e^{2\eta} P_{\text{L}}^{k_3} P_{\text{L}}^{k_4} \left( F_{a_1}^{(2)}(\mathbf{k}_{13}, -\mathbf{k}_3) F_{a_2}^{(2)}(\mathbf{k}_{24}, -\mathbf{k}_4) P_{\text{L}}^{k_{13}} \right. \\ &\quad \left. + F_{a_1}^{(2)}(\mathbf{k}_{14}, -\mathbf{k}_4) F_{a_2}^{(2)}(\mathbf{k}_{23}, -\mathbf{k}_3) P_{\text{L}}^{k_{14}} \right). \end{aligned} \quad (3.20)$$

<sup>8</sup>See also Section 2.7.

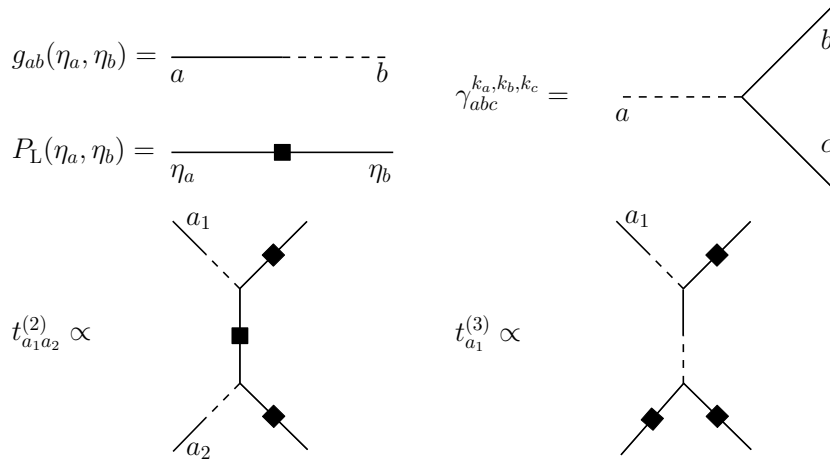


**Figure 3.3.:** Diagrammatic representation of the linear propagator  $g_{ab}(\eta_a, \eta_b)$ , the linear power spectrum to different times  $P_L^k(\eta_a, \eta_b)$ , the renormalization vertex  $\gamma_{abc}^{k_a, k_b, k_c}$  and the tree-level trispectrum contributions  $t_{a_1 a_2}^{(2)}((\mathbf{k}_1, \mathbf{k}_2), (\mathbf{k}_3, \mathbf{k}_4))$  and  $t_{a_1}^{(3)}(\mathbf{k}_1, \mathbf{k}_2, \mathbf{k}_3, \mathbf{k}_4)$ .

The second contribution is due to third order perturbation theory. Here, one field is expanded to third order while the other three remain at linear order. For this reason only one perturbation kernel appears in the expression for this type of contributions,

$$t_{a_1}^{(3)}(\mathbf{k}_1, \mathbf{k}_2, \mathbf{k}_3, \mathbf{k}_4) = 6 e^{2\eta} F_{a_1}^{(3)}(\mathbf{k}_1, \mathbf{k}_2, \mathbf{k}_3) P_L^{k_1} P_L^{k_2} P_L^{k_3}. \quad (3.21)$$

With these two functions the connected perturbation theory four-point correlator up to third order in the linear power spectrum  $P_L^k$  can be expressed by the following two tree-level contributions

$$\begin{aligned} \langle \varphi_1 \varphi_2 \varphi_3 \varphi_4 \rangle_c &= \delta_D(\mathbf{k}_{1\dots 4}) t_{a_1 a_2}^{(2)}((\mathbf{k}_1, \mathbf{k}_2), (\mathbf{k}_3, \mathbf{k}_4)) + \text{all pairs} \in \{1, 2, 3, 4\} \\ &+ \delta_D(\mathbf{k}_{1\dots 4}) t_{a_1}^{(3)}(\mathbf{k}_1, \mathbf{k}_2, \mathbf{k}_3, \mathbf{k}_4) + \text{cyclic} \{1, 2, 3, 4\}. \end{aligned} \quad (3.22)$$

### 3.3.3. Trispectrum in TRG

Our main objective is to investigate the influence of the perturbation theory trispectrum on the evolution of the power spectrum. Writing the connected four-point correlator in terms of the trispectrum  $T_{a_1 a_2 a_3 a_4}^{k_1, k_2, k_3}$ ,

$$\langle \varphi_1 \varphi_2 \varphi_3 \varphi_4 \rangle_c = \delta_D(\mathbf{k}_{1\dots 4}) T_{a_1 a_2 a_3 a_4}^{k_1, k_2, k_3}, \quad (3.23)$$

we can now include the corresponding corrections into our formalism. Taking the trispectrum in the hierarchy of eqn. (3.3) into account will change the closed system of eqn. (3.6) to

$$\begin{aligned} \partial_\eta P_{ab}^k &= -\Omega_{ac} P_{cb}^k - \Omega_{bc} P_{ac}^k + e^\eta \int d^3 q \left[ \gamma_{acd}^{k, q, p} B_{bcd}^{k, q, p} + (a \leftrightarrow b) \right] \\ \partial_\eta B_{abc}^{k, q, p} &= -\Omega_{ad} B_{dbc}^{k, q, p} - \Omega_{bd} B_{adc}^{k, q, p} - \Omega_{cd} B_{abd}^{k, q, p} \\ &+ 2 e^\eta \left[ \gamma_{ade}^{k, q, p} P_{db}^q P_{ec}^p + \gamma_{bde}^{q, p, k} P_{dc}^p P_{ea}^k + \gamma_{cde}^{p, k, q} P_{da}^k P_{eb}^q \right] \\ &+ e^\eta \int d^3 r \left[ \gamma_{agh}^{k, r, |r-k|} T_{bcgh}^{q, p, r} + \gamma_{bgh}^{q, r, |r-q|} T_{cagh}^{p, k, r} + \gamma_{cgh}^{p, r, |r-p|} T_{abgh}^{k, q, r} \right]. \end{aligned} \quad (3.24)$$

Since the trispectrum is taken from perturbation theory, the evolution of the next higher correlator is not needed for its description. One can stick to the same numerical solving procedure as presented in section (3.2.3). Modifications appear in the time evolution of the integrals  $I_{acd, bef}^k$  from eqn. (3.9) via

changing the correction integrals  $A_{acd,bef}^k$  from eqn. (3.10):

$$\begin{aligned}
 A_{acd,bef}^k &\rightarrow A_{acd,bef}^k + \Delta A_{acd,bef}^k & (3.25) \\
 \Delta A_{acd,bef}^k &= \frac{k}{8\pi} \int d^3q \int d^3r \times \\
 &\quad \left( \gamma_{acd}^{k,q,p} \left[ \gamma_{bgh}^{k,r,|r-k|} T_{efgh}^{q,p,r} + \gamma_{egh}^{q,r,|r-q|} T_{fbgh}^{p,k,r} + \gamma_{fgh}^{p,r,|r-p|} T_{begh}^{k,q,r} + (q \leftrightarrow p) \right] \right). & (3.26)
 \end{aligned}$$

While the former expression in eqn. (3.10) was a one loop integral only, we now have to integrate twice over the full Fourier-space. The reason for this are the additional  $\delta_D$ -functions in the disconnected parts of the four-point correlator in eqn. (3.4). The integration is performed numerically using Monte Carlo integration techniques from the multi-dimensional numerical integration library CUBA (Hahn, 2005).

### 3.4. Diagrammatic description

An analytic solution for the system in eqn. (3.6) can be formulated (Pietroni, 2008). This is still the case for the system in eqn. (3.24) with additional trispectrum terms. Solving first the linearized evolution equations (3.2) one can write down the linear solutions for the fields  $\varphi_{a,L}(\mathbf{k}, \eta)$  with the help of the linear propagator  $g_{ab}(\eta, \eta')$  (Matarrese & Pietroni, 2007; Crocce & Scoccimarro, 2006b), which was introduced in Section 2.8.3,

$$\varphi_{a,L}(\mathbf{k}, \eta) = g_{ab}(\eta, \eta') \varphi_{b,L}(\mathbf{k}, \eta'). \quad (3.27)$$

Furthermore, the linear propagator has the following properties,

$$\begin{aligned}
 \partial_\eta g_{ab}(\eta, \eta') &= -\Omega_{ac}(\eta) g_{cb}(\eta, \eta') \\
 g_{ab}(\eta, \eta) &= \delta_{ab} \\
 g_{ab}(\eta, \eta') g_{bc}(\eta', \eta'') &= g_{ac}(\eta, \eta''). & (3.28)
 \end{aligned}$$

With help of this linear propagator a formal analytic solution can be given for the system (3.24),

$$\begin{aligned}
 P_{ab}^k(\eta) &= g_{ac}(\eta, 0) g_{bd}(\eta, 0) P_{cd}^k(\eta = 0) \\
 &\quad + \int_0^\eta d\eta' e^{\eta'} \int d^3q g_{ae}(\eta, \eta') g_{bf}(\eta, \eta') \left[ \gamma_{ecd}^{k,q,p} B_{fcd}^{k,q,p}(\eta') + \gamma_{fcd}^{k,q,p} B_{ecd}^{k,q,p}(\eta') \right] & (3.29) \\
 B_{abc}^{k,q,p}(\eta) &= g_{ad}(\eta, 0) g_{be}(\eta, 0) g_{cf}(\eta, 0) B_{def}^{k,q,p}(\eta = 0) \\
 &\quad + \int_0^\eta d\eta' \int d^3q e^{\eta'} g_{ad}(\eta, \eta') g_{be}(\eta, \eta') g_{cf}(\eta, \eta') \\
 &\quad \left( 2 \left[ \gamma_{dgh}^{k,q,p} P_{eg}^q(\eta') P_{fh}^p(\eta') + \gamma_{egh}^{q,p,k} P_{fg}^p(\eta') P_{dh}^k(\eta') + \gamma_{fgh}^{p,k,q} P_{dg}^k(\eta') P_{eh}^q(\eta') \right] \right. \\
 &\quad \left. + \int d^3r \left[ \gamma_{dgh}^{k,r,|r-k|} T_{efgh}^{q,p,r} + \gamma_{egh}^{q,r,|r-q|} T_{fdgh}^{p,k,r} + \gamma_{fgh}^{p,r,|r-p|} T_{deg h}^{k,q,r} \right] \right). & (3.30)
 \end{aligned}$$

For a better understanding of the trispectrum corrections to the power spectrum it is useful to analyze the equations in a diagrammatic representation. In the upper part of Fig. 3.3 symbols for the linear propagator  $g_{ab}(\eta_a, \eta_b)$ , the renormalization vertex  $\gamma_{abc}^{k_a, k_b, k_3}$  and the linear power spectrum to different times  $P_L(\eta_a, \eta_b)$  are depicted. A diagrammatic representation for the perturbation theory kernels is also needed to describe the trispectrum. Since we used the perturbation theory trispectrum to third order in the power spectrum, the kernels of second and third order are sufficient.

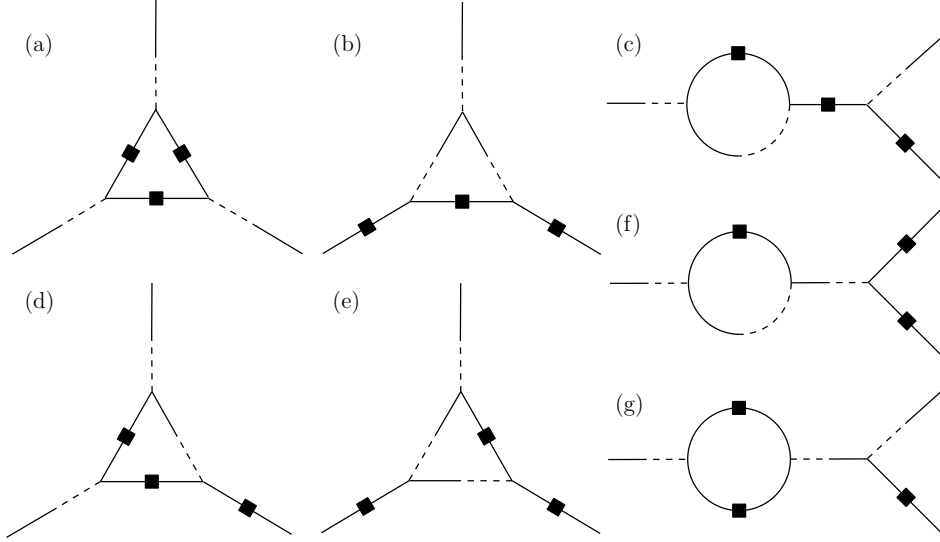


**Figure 3.4.:** The lowest order corrections to the bispectrum - as can be seen in eqn. (3.29) - originating from the trispectrum of tree-level perturbation theory in eqn. (3.22). The diagrams (a)-(c) originate from the second order kernels  $F_a^{(2)}$  in eqn. (3.20), diagram (c) can be formed from both second order kernels or third order kernels  $F_a^{(3)}$  in eqn. (3.21), while diagrams (e)-(f) are only due to the third order perturbation theory in the trispectrum. Also here, one can see that all perturbative corrections, which we included, are of third order in the linear power spectrum. All diagrams are third order in the initial power spectrum and third order in the renormalization vertex  $\mathcal{O}(\gamma^3)$ . The latter is due to the fact that the bispectrum evolution equation in eqn. (3.3) is first order in the vertex.

For time-independent  $\Omega_{ab}$ , i.e.  $f_+ = \Omega_m^{1/2}$ , one can invert the evolution matrix  $(\partial_\eta \delta_{ab} - \Omega_{ab})$  of the structure formation eqs. (3.2) in Laplace-space and finds the non-linear evolution as a time-convolution of the fields  $\varphi$  and the linear propagator  $\tilde{g}_{ab}$  in the following form

$$\varphi_a(\mathbf{k}, \eta) = \tilde{g}_{ab}(\eta, \eta_0) \varphi_b(\mathbf{k}, \eta_0) + \int_0^\eta d\eta' \tilde{g}_{ab}(\eta, \eta') \tilde{\gamma}_{bcd}^{k,-q,-p} \varphi_c(\mathbf{q}, \eta') \varphi_d(\mathbf{p}, \eta'). \quad (3.31)$$

This was shown in detail in Section 2.8.2. Solving these equations iteratively one can express the perturbation theory kernels from eqs. (2.50) in terms of the vertex  $\gamma_{abc}$  and the linear propagator  $\tilde{g}_{ab}$ , which is the linear propagator for time-independent  $\Omega_{ab}$ ,

$$\begin{aligned} F_a^{(2)}(\mathbf{k}_1, \mathbf{k} - \mathbf{k}_1) &= e^{-\eta} \int_0^\eta d\eta' \tilde{g}_{ab}(\eta, \eta') \gamma_{bcd}^{k,-k_1, k_1-k} u_c u_d \\ F_a^{(3)}(\mathbf{k}_1, \mathbf{k}_2, \mathbf{k} - \mathbf{k}_1 - \mathbf{k}_2) &= e^{-\eta} \int_0^\eta d\eta' \int_0^{\eta'} d\eta'' \tilde{g}_{ab}(\eta, \eta') u_c u_g u_h \\ &\quad \left[ \gamma_{bcd}^{k,-k_1, k_1-k} \tilde{g}_{df}(\eta', \eta'') \gamma_{fgh}^{k-k_1, -k_2, k_1+k_2-k} + (\mathbf{k}_1 \leftrightarrow \mathbf{k} - \mathbf{k}_1) \right]. \end{aligned} \quad (3.32)$$

In the diagrammatic representation only, we omit the difference between the linear propagators and set  $g_{ab} \approx \tilde{g}_{ab}$ . Then, the two trispectrum contributions from eqs. (3.20)-(3.21) can be expressed as in the last row of Fig. 3.3. The rules for the diagrams are:

- Time flows monotonically from the linear power spectra towards the external legs.
- All inner field indices are summed over.

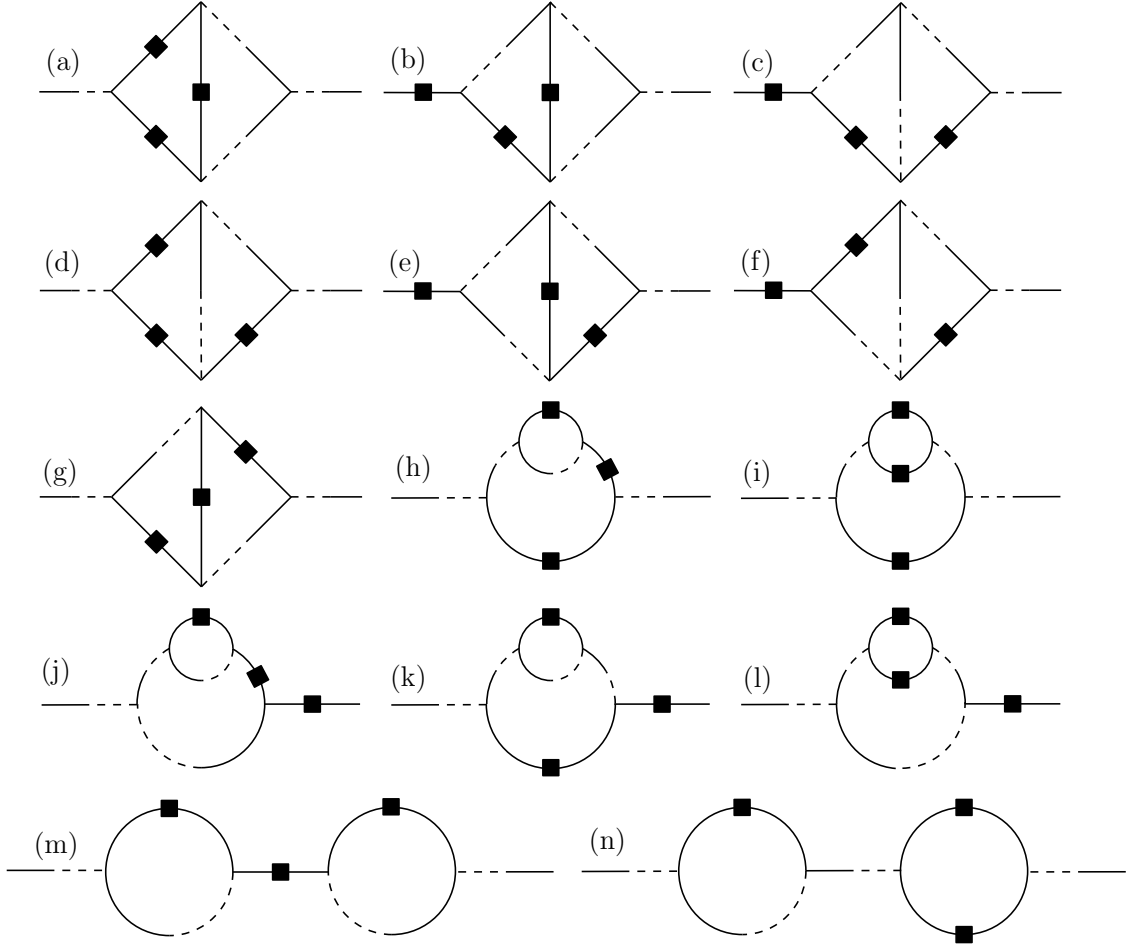


**Figure 3.5.:** The lowest order corrections to the power spectrum originating from the trispectrum of tree-level perturbation theory in eqn. (3.22). The diagrams (a)-(g) originate - as can be seen in eqn. (3.29) - from vertex contraction with the bispectrum correction diagrams (a),(b),(d) and (e) in Fig. 3.4, likewise diagrams (i)-(n) can be formed from the diagrams (c),(f) and (g) in Fig. 3.4. Also here, one can see that all perturbative corrections, which we included, are of third order in the linear power spectrum. All diagrams are third order in the renormalization vertex  $\mathcal{O}(\gamma^3)$ . The latter is due to the fact that the bispectrum evolution equation in eqn. (3.3) is first order in the vertex.

- All inner times at vertex intersections are integrated over in accordance with causality.
- Momentum conservation holds at each vertex and all inner momenta are integrated over.

The perturbation theory trispectrum terms lead to corrections in the bispectrum in eqn. (3.30). The lowest order corrections to the bispectrum are shown in Fig. 3.4. All the depicted terms are third order  $\mathcal{O}(\gamma^3)$  in the renormalization vertex since the trispectrum itself is second order in  $\gamma$  (Fig 3.3) and eqn. (3.30) is first order in  $\gamma$ . The diagrams (a)-(c) in Fig. 3.4 originate from the second order kernels  $F_a^{(2)}$  in eqn. (3.20), diagram (c) can be formed from both second order kernels or third order kernels  $F_a^{(3)}$  in eqn. (3.21), while diagrams (e)-(f) are only due to the third order perturbation theory in the trispectrum. Also here, one can see that all perturbative corrections, which we included, are of third order in the linear power spectrum. While the perturbation theory trispectrum is calculated at tree-level, both the evolution equations - for the bispectrum and for the power spectrum - introduce one momentum integration. Therefore, all the lowest order corrections to the bispectrum are one loop diagrams and the lowest order corrections to the power spectrum are two loop diagrams. The latter diagrams can easily be found by all possible contractions of the diagrams in Fig. 3.4 with a vertex  $\gamma$ ,

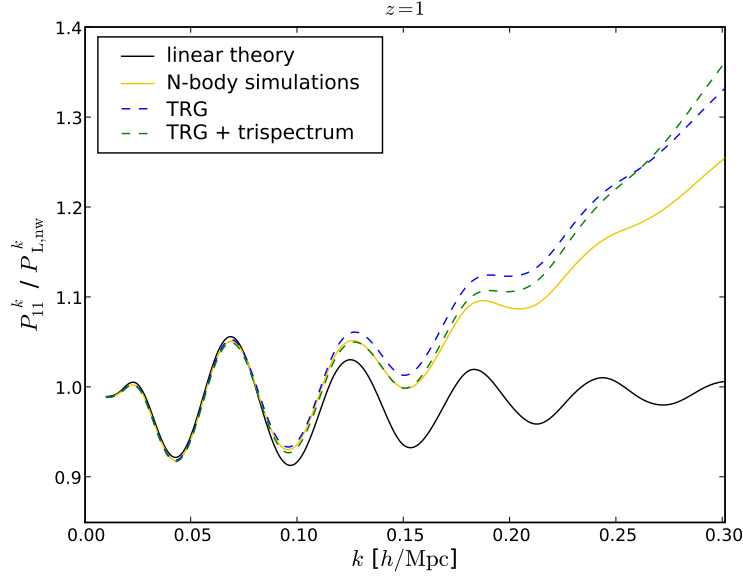


**Figure 3.6.:** Matter power spectra  $P_{11}^k$  divided by a linear spectrum without baryonic wiggles  $P_{L,nw}^k$  (Eisenstein & Hu, 1998) in the mildly non-linear regime for  $z = 1$ . The linear spectrum is depicted as solid (black) line. A spectrum from  $N$ -body simulations (Carlson et al., 2009) serves as reference (yellow). The dashed (blue) line is time-RG theory and the dashed (green) line is time-RG theory with trispectrum included.

leading to the corresponding  $\mathcal{O}(\gamma^4)$  corrections in the spectrum.

We want to emphasize at this point that the inclusion of the perturbation theory trispectrum does not lead to a simple perturbative correction only. At each time step the perturbative trispectrum corrects the evolution of bispectrum and power spectrum. Therefore, from that moment on these corrections will be involved in the non-perturbative method of time renormalization. In this work we only discuss the trispectrum corrections to this method, since the quality and performance of the original time renormalization technique has been thoroughly discussed already (Pietroni, 2008).

### 3.5. Numerical results

We solved the system of equations (3.24) starting from redshift  $z = 100$  well within the linear regime with Gaussian initial growing mode conditions. We evolved the system to redshifts  $z = 1$  and  $z = 0$  with and without trispectrum included and compared the power spectra with results from numerical simulations of the same  $\Lambda$ CDM cosmology (Carlson et al., 2009). Due to numerical complexity only power spectra up to  $k = 1 h \text{Mpc}^{-1}$  were included in the trispectrum integrals  $\Delta I_{acd,bef}^k$  from eqn. (3.26). However, in the integrals  $I_{acd,bef}^k$  from eqn. (3.10) modes up to  $k = 10 h \text{Mpc}^{-1}$  were taken into account, were the results saturate to percent accuracy.

The results are shown in Fig. 3.6 and Fig. 3.7 for redshifts  $z = 1$  and  $z = 0$ , respectively, where also the linearly evolved power spectrum is depicted. All spectra were divided by a linear power spectrum  $P_{L,nw}^k$  without wiggles from baryonic acoustic oscillations (Eisenstein & Hu, 1998, eqn. 29). For  $z = 1$  the results with the trispectrum included are in excellent agreement with numerical simulations up to  $k \simeq 0.17 h \text{Mpc}^{-1}$ . For  $0.17 h \text{Mpc}^{-1} \leq k \leq 0.25 h \text{Mpc}^{-1}$  the method performs still better than without trispectrum included. Beyond this regime the perturbative description of the trispectrum breaks down and the results are in strong disagreement with simulations.

It is not surprising that below a certain scale the method performs better without the perturbative trispectrum included. For larger  $k$ , also trispectra at smaller scales contribute to the integrals  $\Delta A_{acd,bef}^k$  in eqn. (3.26). Since in perturbation theory loop corrections become more and more important at

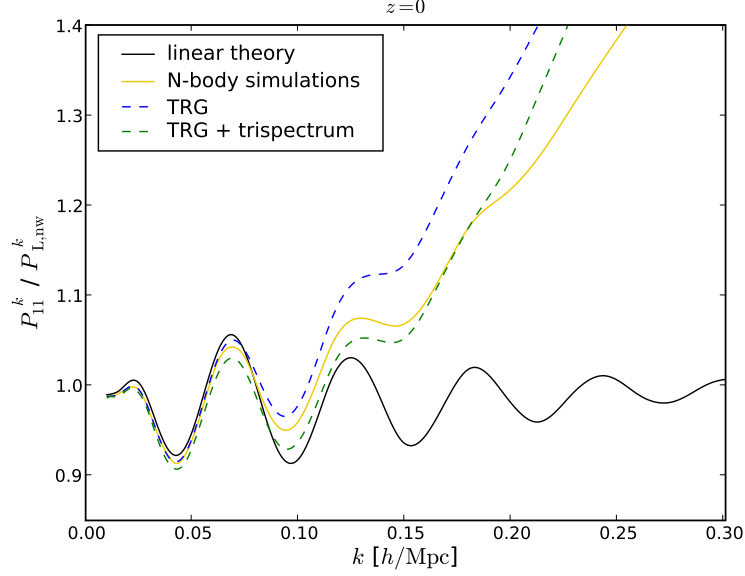


**Figure 3.7.:** Matter power spectra  $P_{11}^k$  divided by a linear spectrum without baryonic wiggles  $P_{L,nw}^k$  (Eisenstein & Hu, 1998) in the mildly non-linear regime for  $z = 0$ . The linear spectrum is depicted as solid (black) line. A spectrum from  $N$ -body simulations (Carlson et al., 2009) serves as reference (yellow). The dashed (blue) line is time-RG theory and the dashed (green) line is time-RG theory with trispectrum included.

smaller scales, the tree-level trispectrum description breaks down above a specific wave number. For this reason, beyond  $k \approx 0.25 h \text{Mpc}^{-1}$  time renormalization without trispectrum will lead to better results in comparisons to numerical simulations.

At  $z = 0$  trispectrum corrections overcompensate the too strong growth in the pure TRG approach on scales below  $k \approx 0.15 h \text{Mpc}^{-1}$  and lead to too little growth. In this regime our results agree with the numerical simulations within 2.5%. The better agreement for  $z = 1$  on these scales may simply be due to the breakdown of the tree-level perturbative description of the trispectrum at later times. Beyond  $k \approx 0.15 h \text{Mpc}^{-1}$  the inclusion of the trispectrum leads to a better agreement with simulations than pure TRG, while both methods show too strong growth further into the non-linear regime.

The results for pure TRG may differ from the results of Pietroni (2008), since only 12 instead of 14 independent integrals  $I_{acd,bef}^k$  were included in the original method. However, in later applications all 14 independent were taken into account.

### 3.6. Full trispectrum evolution - limits of contemporary numerics

The logical next step in the hierarchy would be the inclusion of the full time evolution of the trispectrum  $T_{a_1 a_2 a_3 a_4}^{k_1 k_2 k_3}$ . To achieve this, one would need to go to the next equation in the infinite hierarchy of evolution equations in eqn. (3.3). If one now neglects in analogy to the standard time renormalization approach the connected part of the five-point correlator, one can write the time evolution of the connected four-point correlator as

$$\begin{aligned} \partial_\eta \langle \varphi_a \varphi_b \varphi_c \varphi_d \rangle_c &= -\Omega_{ae} \langle \varphi_e \varphi_b \varphi_c \varphi_d \rangle_c + \text{cyclic} \{a, b, c, d\} \\ &+ e^\eta \tilde{\gamma}_{aef} \left[ \langle \varphi_e \varphi_b \rangle \langle \varphi_f \varphi_c \varphi_d \rangle + \text{cyclic} \{b, c, d\} + (e \leftrightarrow f) \right] \\ &+ \text{cyclic} \{a, b, c, d\}. \end{aligned} \quad (3.33)$$

In this way one would obtain a closed system, described by the power spectrum, bispectrum and trispectrum. For a numerical solution one can again circumvent the bookkeeping of the highest included correlator by introducing an integral quantity. As  $I_{acd,bef}^k$  was the integral quantity of the

bispectrum, we can define for the trispectrum  $L_{bgh,efij}^{kqp}$ ,

$$\begin{aligned} L_{bgh,efij}^{kqp} &\equiv \frac{1}{2} \int d^3r \frac{1}{2} \left[ \gamma_{bgh}^{k,r,|r+k|} T_{efij}^{q,k-q,r,-r-k} + (\mathbf{r} \leftrightarrow -\mathbf{r} - \mathbf{k}) \right] \\ A_{acd,bef}^k &= \frac{k}{4\pi} \int d^3q \frac{1}{2} \left[ \gamma_{acd}^{k,q,p} \left( \gamma_{bgh}^{k,q,p} P_{ge}^q P_{hf}^p + \gamma_{egh}^{q,p,k} P_{gf}^p P_{hg}^k + \gamma_{fgh}^{p,k,q} P_{gb}^k P_{he}^q \right. \right. \\ &\quad \left. \left. + L_{bgh,efgh}^{k,q,|k-q|} + L_{egh,bfgh}^{q,k,|q-k|} + L_{fgh,begh}^{|k+q|,k,q} \right) + (q \leftrightarrow p) \right], \end{aligned} \quad (3.34)$$

where  $\mathbf{p} = \mathbf{k} - \mathbf{q}$  was implied in the integration. As can be seen from eqn. (3.33), the time evolution of  $L_{bgh,efij}^{kqp}$  is now given by the full power spectrum and bispectrum. To lowest order, this time evolution could be approximated on tree-level,

$$\begin{aligned} P_{ab}^k &= P_L^k \\ B_{abc}^{k,q,p} &= B_{\text{tree}}^{k,q,p} = 2D_+(\eta) \left( F_0^{k,q} P_L^k P_L^q + \text{cyclic} \{b, c, d\} \right). \end{aligned} \quad (3.35)$$

However, it is demonstrated, that even going only to the next order evolution equation drives the numerical cost to an insensible level. The numerical bookkeeping of the integral quantity  $L_{bgh,efij}^{kqp}$  on a 3d-grid as well as the multiple higher order integrations are straightforward and possible. But the advantage of the method of being a fast technique to predict statistics in the mildly non-linear regime is certainly diminished by the increasing numerical effort, since results in reasonable accuracy are not available within days on normal computers.

### 3.7. Summary

In this chapter the influence of the tree-level trispectrum on the time renormalization method (Pietroni, 2008) has been studied. To keep the computational effort at a reasonable level we did not include the full trispectrum evolution from the hierarchy. Instead, we used tree-level perturbation theory for the trispectrum in the evolution of the bispectrum.

(1) The trispectrum was formulated in standard perturbation theory to third order in the linear power spectrum  $P_L^k$ . This was included in the evolution equation of the bispectrum.

(2) The numerical method for solving the system was extended by the trispectrum corrections. Due to the linear time dependence of the perturbation theory trispectrum it is sufficient to calculate the correction integrals at one fixed initial time. Once the corrections are derived the extended method operates at the same speed as the time renormalization method without trispectrum included. The diagrams for the lowest order corrections to the bispectrum were depicted in Fig. 3.4, from which all lowest order terms for the power spectrum originating from the tree-level trispectrum can be inferred. These 2-loop corrections to the power spectrum are of order  $\mathcal{O}(\gamma^4)$  in the renormalization vertex and third order in the linear power spectrum  $\mathcal{O}(P_L^3)$ .

(3) Perturbative trispectrum corrections are fed into the systems at all times. Once a correction has been included its evolution will be described by the non-perturbative formalism of time renormalization. Therefore, although the trispectrum was only taken into account perturbatively, its inclusion can not be interpreted as a pure perturbative correction disentangled from renormalization.

(4) We solved the system numerically starting with Gaussian initial conditions and a linear power spectrum at an initial redshift of  $z = 100$ . In comparison to numerical simulations (Carlson et al., 2009) the inclusions of the trispectrum generally improves the results up to  $k \approx 0.25 h \text{ Mpc}^{-1}$ . However, on larger scales the damping due to the perturbative tree-level trispectrum overcompensates the deviation of pure TRG from  $N$ -body simulations. The results agree with the simulations within 1% up to  $k \approx 0.18 h \text{ Mpc}^{-1}$  for  $z = 1$  and within 2.5% up to  $k \approx 0.2 h \text{ Mpc}^{-1}$  for  $z = 0$ .

(5) Beyond  $k \approx 0.25 h \text{ Mpc}^{-1}$  the perturbative description of the trispectrum breaks down and the method performs better without trispectrum included. This is due to the fact that loop corrections

to the trispectrum are not included in our method and become more and more important on smaller scales. Adding the perturbation theory trispectrum therefore predominantly pays off on large scales and at the beginning of the mildly non-linear regime.

(6) Although the prediction of the amplitude and position of the first two peaks in the baryonic acoustic oscillations was improved by the trispectrum, we are far from reaching percent accuracy over the entire BAO regime. Also the speed of this method was reduced by including the trispectrum, since the 2-loop trispectrum corrections have to be derived. Finding a better analytical estimator for the trispectrum from other renormalization approaches, which includes higher order corrections, could improve the results of this method further into the mildly non-linear regime. Besides this, studying the dependence of our results on the initial bispectrum would be an interesting objective for future work.



# 4

## Chapter 4

# Introduction to the integrated Sachs-Wolfe effect

For a thorough understanding of the integrated Sachs-Wolfe effect and its measurements, which will be the subject of Chapters 5-6, we will in this chapter firstly review the origin of the cosmic microwave background in Section 4.1 and its anisotropies in Section 4.2. The tracer density field and the iSW effect itself are introduced in Section 4.3 and Section 4.4, respectively. Furthermore, we introduce the description of statistical fluctuations on the sphere (Section 4.5), the flat sky to full sky correspondence (Section 4.6) and the Limber equation (Section 4.7). More details about the processes described in this chapter can be found in [Coles & Lucchin \(2002\)](#); [Durrer \(2008\)](#); [Weinberg \(2008\)](#).

## 4.1. Cosmic microwave background

After the discovery of Hubble's law, one of the next milestones in astrophysics was most certainly the detection of the cosmic microwave background in 1965. Before that event almost all cosmological information was obtained from the observation of distances and redshifts of galaxies. An almost perfectly isotropic microwave source was observed, which was later found to follow a likewise perfect black-body spectrum at a temperature of 2.725 K. The objective of this section is to give a grasp of the physical origin and the vast range of valuable information to be withdrawn from this source.

### 4.1.1. Recombination

As mentioned earlier, the expansion of the Universe was indicated by the observation of increasing galaxy redshifts with increasing distance. By the observation of distant quasars with a redshift of up to  $z \approx 9$  this expansion was proven to last since the Universe was at least ten times smaller than today. Under these conditions, within the framework of General Relativity, the Universe even has to have expanded from a very small initial scale.

As the Universe expands, it loses thermal energy while it performs work against pressure. Consequently, it was much hotter in its early days. Before a redshift of  $z \approx 1089$  ([Spergel et al., 2003](#)) it was so hot that rapid collisions of electrons with highly energetic photons were too likely for stable hydrogen to form. The hot dense matter at that time was in thermal equilibrium with the photons. In other words the process of ionizing a hydrogen atom was as likely as a recombination process,



The density of photons at that time was then given by the black-body spectrum,

$$n_{T_L}(\omega, a_L) d\omega = \frac{8\pi\omega^2}{\exp(h\omega/k_B T_L) - 1} d\omega \quad (4.2)$$

As the Universe had cooled down sufficiently at a scale factor of about  $a_L \approx 1/1000$ , stable hydrogen formed and photons were not energetic and dense enough anymore to reionize the gas. For this reason the matter content of the Universe decoupled from radiation. The photon frequency of  $\omega$  at the last scattering surface was shifted to  $\omega a/a_L$  by the expansion of the Universe. Likewise, the photon density was diluted by a factor of  $(a/a_L)^3$ . Therefore, the spectrum at time  $a$  was given by

$$\begin{aligned} n_{T_a}(\omega, a) d\omega &= (a_L/a)^3 n_{T_L}(\omega a/a_L, a_L) d(\omega a/a_L) \\ &= \frac{8\pi \omega^2}{\exp(h\omega/k_B T_a) - 1} d\omega, \end{aligned} \quad (4.3)$$

with

$$T_a = T_L a_L/a. \quad (4.4)$$

For this reason, we still observe a black-body spectrum, even though the photons are not in thermal equilibrium with matter any more.

## 4.2. Anisotropies

The cosmic microwave background, however, as it is observed by us, is not completely isotropic. To obtain a feeling of how the observation of the CMB or the cosmic radiation itself can be subjected to anisotropic effects, the most important sources of anisotropy shall be shortly motivated in this Section. More details about these effects can be found in cosmology text books (Coles & Lucchin, 2002; Weinberg, 2008).

The largest contribution to anisotropy is given by the motion of our Earth with respect to the CMB rest frame, which was found to be  $(371 \pm 1)$  km/s. For this reason, the observed temperature is shifted to a dipole,

$$T_{\text{obs}}(\omega_{\text{obs}}) = \frac{T}{\gamma(1 + \beta \cos \theta)}, \quad (4.5)$$

where  $\beta = v/c$  denotes the velocity of the observer with respect to the CMB rest frame and  $\theta$  the observation angle with respect to the direction of motion. Fortunately, since this effect is not statistical, it can be corrected for.

In addition to this, also statistical effects can cause anisotropies in the CMB. When the cosmic microwave background was generated, the density field was not perfectly homogeneous, due to small density perturbations originating from quantum fluctuation in the young Universe. Small perturbations in the density field  $\delta\rho$  induce metric perturbations proportional to the corresponding potential perturbation. These changes in the metric will alter the frequency of a photon at the last scattering surface in two different ways. First, photons climbing out of a metric perturbation experience a redshift, which corresponds to a observed relative temperature fluctuation of

$$\frac{\Delta T}{T} = \frac{\delta\phi}{c^2}. \quad (4.6)$$

Second, the photons suffer from a time dilatation effect. One effectively observes the photons at a different time depending on the potential depth they are climbing out of. One therefore observes today photons which decoupled from matter at slightly different time and thus different temperatures. This effect can be quantified to

$$\frac{\Delta T}{T} = -\frac{\delta a}{a} = -\frac{2}{3} \frac{\delta t}{t} = -\frac{2}{3} \frac{\delta\phi}{c^2}. \quad (4.7)$$

In total, a temperature perturbation of

$$\frac{\Delta T}{T} = \frac{1}{3} \frac{\delta\phi}{c^2} \quad (4.8)$$

is induced. This effect is called early time Sachs-Wolfe effect (Sachs & Wolfe, 1967) and is completed after recombination. The Sachs-Wolfe effect couples to the gravitational potential perturbations  $\delta\phi$ , which is varying on larger scales than the matter density itself.

Furthermore, the density perturbations at the last scattering surface also induce velocity perturbations. These contribute to the anisotropy by simple Doppler effect at the time of recombination,

$$\frac{\Delta T}{T} \simeq \frac{v}{c}. \quad (4.9)$$

All the effects mentioned so far can act as a valuable probe of the Universe as it was at the time of the last scattering surface. These primary anisotropies can be observed in the cosmic microwave background (CMB) in form of temperature fluctuations  $\Delta T/T_{\text{CMB}} \simeq 10^{-5}$  on large scales around its mean temperature  $T_{\text{CMB}} = 2.725$  K (Fixsen, 2009). Cosmological models can be constrained by comparison of theoretical predictions and measurements. The impressive homogeneity of the CMB or the weakness of the density perturbations at the time of its creation turned out to be a strong argument for the existence of dark matter. The baryonic matter content of the Universe alone would not have managed to generate the large and pronounced structures we find in our late Universe.

But the CMB carries even more information, which the photons have collected on their way from the last scattering surface to the observer. One example is gravitational lensing (Seljak, 1996a; Stompor & Efstathiou, 1999; Hu, 2000), where the geodesic of the photon is perturbed by gravitational wells, and it is therefore observed at a different angle on the sky. Another secondary anisotropy originated from hot electron plasmas in galaxy clusters. The relatively low energetic entering photons are Compton scattered to higher energies. This implies a dip in the *Planck* spectrum in the lower range and an increase in the photon density at higher frequencies. The division frequency between the two ranges lies at  $\sim 217$  GHz. This is the so-called thermal *Sunyaev-Zel'dovich* effect (Sunyaev & Zeldovich, 1980), which can be easily distinguished observationally from all achromatic anisotropies due to the change of the spectrum's shape.

The last effect, which should be mentioned here, is sensitive to the time evolution of potential wells. Therefore, it is particularly interesting, since it delivers information about the expansion history of the Universe and the structure formation of the dark matter component. The so-called integrated *Sachs-Wolfe* effect or late time *Sachs-Wolfe* effect will be the main subject of this and the next chapters.

### 4.3. Galaxy distribution

Galaxies form when high peaks in the density field decouple from the Hubble expansion due to self-gravity. These so called protohalos approximately undergo an elliptical collapse (Mo et al., 1997; Sheth et al., 2001).

In contrary to the dissipation-less dark matter component the baryons inside a dark matter halo can lose energy via radiative cooling and form stars. Because of this different behavior, strictly speaking, one can not deduce the fractional perturbation  $\Delta n/\langle n \rangle$  in the mean number density of galaxies  $\langle n \rangle$  from the dark matter over-density  $\delta = \Delta\rho/\rho$ . In a very simple way, however, the linear relation between the two quantities,

$$\frac{\Delta n}{\langle n \rangle} = b \frac{\Delta\rho}{\langle \rho \rangle}, \quad (4.10)$$

is a good approximation in most cases and was proposed by Bardeen et al. (1986). The bias parameter  $b$  can generally depend on scale (Lumsden et al., 1989), time (Fry, 1996; Tegmark & Peebles, 1998) as well as the galaxies luminosity and morphology. For simplicity we set the galaxy bias to unity throughout this paper,  $b \equiv 1$ . An established parametrization of the redshift distribution  $n(z) dz$  of galaxies is

$$n(z) dz = n_0 \left(\frac{z}{z_0}\right)^2 \exp\left[-\left(\frac{z}{z_0}\right)^\beta\right] dz \quad \text{with} \quad \frac{1}{n_0} = \frac{z_0}{\beta} \Gamma\left(\frac{3}{\beta}\right), \quad (4.11)$$

which was introduced by [Smail et al. \(1995\)](#) and will be used in this thesis. The parameter  $z_0$  is related to the median redshift of the galaxy sample  $z_{\text{med}} = 1.406 z_0$  if  $\beta = 3/2$ . Finally, the  $\Gamma$ -function ([Abramowitz & Stegun, 1972](#)) determines the normalization parameter  $n_0$ .

#### 4.4. Integrated Sachs-Wolfe effect

Assuming a completely transparent space, i.e. vanishing optical depth due to Compton scattering  $\tau_{\text{opt}}(\eta) = 0$ , the temperature fluctuations  $\tau(\hat{\theta})$  generated by the iSW-effect can be expressed by the line-of-sight integral ([Sachs & Wolfe, 1967](#))

$$\tau(\boldsymbol{\theta}) \equiv \frac{\Delta T_{\text{iSW}}}{T_{\text{CMB}}} = \frac{2}{c^3} \int_0^{\chi_H} d\chi a^2 H(a) \frac{\partial}{\partial a} \Phi(\boldsymbol{\theta}\chi, \chi), \quad (4.12)$$

where the comoving distance integration reaches out to the Hubble distance  $\chi_H = c/H_0$ . The Hubble distance is chosen for the Newtonian limit since retardation effects become dominant at larger distances. Using the Poisson equation we can write this integral in terms of the dimensionless potential  $\phi = \Phi/\chi_H^2 = \Delta^{-1} \delta/\chi_H^2$  from the density field  $\delta$ ,

$$\tau(\boldsymbol{\theta}) = \frac{3\Omega_m}{c} \int_0^{\chi_H} d\chi a^2 H(a) \frac{d}{da} \frac{D_+}{a} \phi(\boldsymbol{\theta}\chi, \chi). \quad (4.13)$$

Heuristically, the effect originates from an imbalance between the photon's blue-shift when entering a time varying potential well and the red-shift experienced at the exit.

The effect vanishes identically in matter dominated universes  $\Omega_m = 1$ , since then  $D_+/a$  is a constant. Therefore, a non-zero iSW-signal will be an indicator of a cosmological fluid with  $w \neq 0$ . After the radiation dominated era it will thus be a valuable tool for investigating dark energy cosmologies. The inverse Laplacian, which solves for the potential in the Poisson equation, introduces a  $k^{-2}$  term. For this reason, small scale fluctuations will be quadratically damped and the iSW-effect provides a signal on large scales and will be negligible above  $\ell \approx 100$ .

In order to verify the existence of the effect it is necessary to investigate the cross-correlation of the iSW amplitude with the line-of-sight projected relative galaxy over-density  $\gamma$ ,

$$\gamma(\boldsymbol{\theta}) = b \int_0^{\chi_H} d\chi n(z) \frac{dz}{d\chi} D_+ \delta(\boldsymbol{\theta}\chi, \chi). \quad (4.14)$$

We obtain the dimensionless observables  $\gamma$  and  $\tau$  from a line-of-sight integration of the two dimensionless source fields  $\delta$  and  $\phi$  weighted by functions which carry units of inverse length. For rather small angular scales on the sphere one can approximate the sphere locally as being plane. One can then work in the so-called flat sky approximation,

$$\gamma(\boldsymbol{\ell}) = \int d^2\theta \gamma(\boldsymbol{\theta}) e^{-i(\boldsymbol{\ell}\cdot\boldsymbol{\theta})}. \quad (4.15)$$

Due to statistical isotropy, there is no directional dependence,  $\gamma(\boldsymbol{\ell}) = \gamma(\ell)$ , and one can define the spectrum  $C_{\gamma\gamma}(\ell)$ :

$$\langle \gamma(\ell) \gamma^*(\ell') \rangle = (2\pi)^2 \delta_D(\ell - \ell') C_{\gamma\gamma}(\ell) \quad (4.16)$$

The observable  $\tau$  can be transformed in an analogous way. With the two weighting functions

$$\begin{aligned} W_\gamma(\chi) &= n(z) \frac{H(z)}{c} D_+(z) \\ W_\tau(\chi) &= 3\Omega_m a^2 \frac{H}{c} \frac{d}{da} \frac{D_+}{a} \end{aligned} \quad (4.17)$$

we can now derive the spectra (Limber, 1953),

$$\begin{aligned}
 C_{\gamma\gamma}(\ell) &= \int_0^{\chi_H} \frac{d\chi}{\chi^2} W_\gamma^2(\chi) P^{k=\ell/\chi} \\
 C_{\tau\gamma}(\ell) &= \int_0^{\chi_H} \frac{d\chi}{\chi^2} W_\tau(\chi) W_\gamma(\chi) P_{\delta\phi}^{k=\ell/\chi} \\
 C_{\tau\tau}(\ell) &= \int_0^{\chi_H} \frac{d\chi}{\chi^2} W_\tau^2(\chi) P_{\phi\phi}^{k=\ell/\chi}.
 \end{aligned} \tag{4.18}$$

The power spectra can be related to the density power spectrum:

$$P_{\phi\phi}^k = \frac{P^k}{(\chi_H k)^4}, \quad P_{\delta\phi}^k = \frac{P^k}{(\chi_H k)^2}. \tag{4.19}$$

The multiplication factors  $k^{-2}$  and  $k^{-4}$  tilt the spectra to smaller values for increasing multipole order  $\ell$  and show once again the iSW-effect to be a large scale phenomenon.

## 4.5. Statistics of fluctuations on the sky

The iSW effect is an integrated quantity observed as an additional anisotropy of the CMB on the sphere. For this reason, it is reasonable to describe its statistics in form of angular correlations on the sphere. In order to do this, we define the two point correlation function of a homogeneous and isotropic random field  $X(\hat{\theta})$  in angular space as

$$C_{XX}(\alpha) = \langle X(\hat{\theta})X^*(\hat{\theta}') \rangle, \tag{4.20}$$

where the separation angle  $\alpha = \langle \hat{\theta}, \hat{\theta}' \rangle$  was defined. The field  $X(\hat{\theta})$  will later be substituted by our two scalar fields of interest  $\gamma(\hat{\theta})$  and  $\tau(\hat{\theta})$ . In analogy to the three dimensional case in Section 2.3 the correlator does not depend on the absolute direction  $\hat{\theta}$  on the sky, but only depends on the absolute value of the separation angle  $\alpha$  - due to isotropy and homogeneity. Again, the brackets indicate the average over the ensemble of the random field. Under the assumption of ergodicity, an estimate of this correlator can be obtained likewise by a measured spatial average of one realization - for instance our Universe. However, this applies only under the assumption of a continuous correlation function (Adler, 1981; Marinucci & Peccati, 2009).

The angular power spectrum  $C_{XX}(\alpha)$  is now defined as the decomposition of the two-point correlator into Legendre polynomials  $P_\ell(\cos \alpha)$ ,

$$C_{XX}(\ell) = 2\pi \int d\cos \alpha C_{XX}(\alpha) P_\ell(\cos \alpha) \quad \leftrightarrow \quad C_{XX}(\alpha) = \frac{1}{4\pi} \sum_{\ell=0}^{\infty} (2\ell + 1) C_{XX}(\ell) P_\ell(\cos \alpha), \tag{4.21}$$

where the orthonormality relation of the Legendre polynomials is used,

$$\int_{-1}^{+1} dx P_\ell(x) P_{\ell'}(x) = \frac{2}{2\ell + 1} \delta_{\ell\ell'}. \tag{4.22}$$

Our random fields are fluctuations on the celestial sphere with homogeneous fluctuation properties. Averaging first over orientations, one can also decompose the fields into spherical harmonics  $Y_{\ell m}(\hat{\theta})$ ,

$$X(\hat{\theta}) = \sum_{\ell=0}^{\infty} \sum_{m=-\ell}^{+\ell} X_{\ell m} Y_{\ell m}(\hat{\theta}) \quad \leftrightarrow \quad X_{\ell m} = \int_{4\pi} d\Omega X(\hat{\theta}) Y_{\ell m}^*(\hat{\theta}). \tag{4.23}$$

Also the spherical harmonics  $Y_{\ell m}(\hat{\theta})$  are orthonormal

$$\int_{4\pi} d\Omega Y_{\ell m}(\hat{\theta}) Y_{\ell' m'}^*(\hat{\theta}) = \delta_{\ell\ell'} \delta_{mm'} \quad (4.24)$$

and represent a complete set of basis functions,

$$\sum_{\ell=0}^{\infty} \sum_{m=-\ell}^{+\ell} Y_{\ell m}(\hat{\theta}) Y_{\ell m}^*(\hat{\theta}') = \delta(\hat{\theta} - \hat{\theta}'). \quad (4.25)$$

For continuous basis systems the orthonormality and completeness relations are mathematically identical and are given in eqn (C.3). As a natural next step, one introduces correlators of the spherical harmonic of the field  $X_{\ell m}$  and relates them to the power spectrum,

$$\langle X_{\ell m} X_{\ell' m'}^* \rangle = \int_{4\pi} d\Omega \int_{4\pi} d\Omega' C_{XX}(\alpha) Y_{\ell m}(\hat{\theta}) Y_{\ell' m'}^*(\hat{\theta}'). \quad (4.26)$$

This was obtained by substituting eqn. (4.23) and employing the definition of the correlation function in eqn. (4.20). If one further uses the addition theorem of the spherical harmonic functions,

$$\sum_{m=-\ell}^{+\ell} Y_{\ell m}(\hat{\theta}) Y_{\ell m}^*(\hat{\theta}') = \frac{2\ell + 1}{4\pi} P_{\ell}(\cos \alpha), \quad (4.27)$$

and replaces the correlator  $C_{XX}(\alpha)$  in terms of the power spectrum  $C_{XX}(\ell)$  via eqn. (4.21), one finds

$$\langle X_{\ell m} X_{\ell' m'}^* \rangle = \delta_{\ell\ell'} \delta_{mm'} C_{XX}(\ell). \quad (4.28)$$

This equation states, that all cross-correlations between different harmonic modes of a homogeneous and isotropic field have to vanish. In addition to this, the variance of the spherical harmonics is given by the power spectrum  $C_{XX}(\ell)$ .

## 4.6. Flat sky to full sky correspondence

Throughout this thesis, we will work in the flat sky approximation only, which was found to be justified for iSW applications (Rassat, 2009). If very large scales are not important it represents a good transformation to the rigorous full sky harmonic representation in eqn. (4.23). In this approximation the angular field is simply decomposed into its 2d-Fourier modes,

$$X(\boldsymbol{\ell}) = \int d^2\theta X(\boldsymbol{\theta}) e^{-i(\boldsymbol{\ell} \cdot \boldsymbol{\theta})}. \quad (4.29)$$

In this section we are pointing out the correspondence between the full sky representation of the field from eqn. (4.23) and its flat sky analogon from eqn. (4.29) following (Hu, 2000). To find out this correspondence, one has to understand that the following transformation leads to the flat sky representation,

$$\begin{aligned} X(\boldsymbol{\ell}) &= \sqrt{\frac{4\pi}{2\ell + 1}} \sum_m i^{-m} X_{\ell m} e^{im\phi_{\ell}} \\ X_{\ell m} &= \sqrt{\frac{2\ell + 1}{4\pi}} i^m \int \frac{d\phi_{\ell}}{2\pi} e^{-im\phi_{\ell}} X(\boldsymbol{\ell}). \end{aligned} \quad (4.30)$$

Both our fields of interest are scalar fields. Therefore, their description in spherical harmonics is

$$X(\hat{\boldsymbol{n}}) = \sum_{\ell m} X_{\ell m} Y_{\ell}^m(\hat{\boldsymbol{n}}). \quad (4.31)$$

For small angles close to the pole one can approximate the spherical harmonics,

$$Y_\ell^m = j_m(\ell\theta) \sqrt{\frac{\ell}{2\pi}} e^{im\phi}. \quad (4.32)$$

Using the expansion of plane waves into spherical harmonics,

$$e^{i\ell\hat{\mathbf{n}}} = \sum_m i^m j_m(\ell\theta) e^{im(\phi-\phi_\ell)} \approx \sqrt{\frac{2\pi}{\ell}} \sum_m i^m Y_\ell^m e^{im\phi_\ell}, \quad (4.33)$$

one can finally write

$$\begin{aligned} X(\hat{\mathbf{n}}) &= \sum_{\ell m} X_{\ell m} Y_\ell^m(\hat{\mathbf{n}}) \\ &\approx \sum_\ell \frac{\ell}{2\pi} \int \frac{d\phi_\ell}{2\pi} X(\boldsymbol{\ell}) \sum_m j_m(\ell\phi) i^m e^{im(\phi-\phi_\ell)} \\ &\approx \int \frac{d^2\ell}{(2\pi)^2} X(\boldsymbol{\ell}) e^{i\ell\hat{\mathbf{n}}}. \end{aligned} \quad (4.34)$$

So we have found the required correspondence. Having the correspondence of the fields at hand, one can now find the relations between the flat sky and full sky correlators. In case of the power spectrum, we use eqn. (4.30) in the definition of the two-point correlator,

$$\langle X_{\ell m}^* X'_{\ell' m'} \rangle = i^{m'-m} \frac{\sqrt{\ell\ell'}}{2\pi} C_{XX'}^\ell \int d\phi_\ell e^{im\phi_\ell} \int d\phi_{\ell'} e^{im'\phi_{\ell'}} \delta_{\mathbb{D}}(\boldsymbol{\ell} - \boldsymbol{\ell}'). \quad (4.35)$$

One can now use an expansion of the  $\delta_{\mathbb{D}}$ -function in spherical harmonics,

$$\begin{aligned} \delta_{\mathbb{D}}(\boldsymbol{\ell} - \boldsymbol{\ell}') &= \int \frac{d\hat{\mathbf{n}}}{(2\pi)^2} e^{i(\boldsymbol{\ell}-\boldsymbol{\ell}')\hat{\mathbf{n}}} \\ &\approx \frac{2\pi}{\sqrt{\ell\ell'}} \int \frac{d\hat{\mathbf{n}}}{(2\pi)^2} \sum_{mm'} i^{m-m'} Y_{\ell'}^{m'*} Y_\ell^m e^{im\phi_\ell - im'\phi_{\ell'}}. \end{aligned} \quad (4.36)$$

By integration over the azimuthal angles  $\phi_\ell$  and  $\phi_{\ell'}$ , one can now compare the full sky power spectrum  $C_{XX'}(\ell)$  to the flat sky representation  $C_{XX'}^\ell$ ,

$$\begin{aligned} \langle X_{\ell m}^* X'_{\ell' m'} \rangle &= \delta_{\ell\ell'} \delta_{mm'} C_{XX'}(\ell) \\ &\approx C_{XX'}^\ell \int d\hat{\mathbf{n}} Y_{\ell'}^{m'*} Y_\ell^m \\ &= \delta_{\ell\ell'} \delta_{mm'} C_{XX'}^\ell. \end{aligned} \quad (4.37)$$

This leads to the approximation

$$C_{XX'}(\ell) \approx C_{XX'}^\ell. \quad (4.38)$$

In case of the bispectrum one follows the analogous line of arguments but one has to replace  $\delta_{\mathbb{D}}(\boldsymbol{\ell} - \boldsymbol{\ell}')$  by  $\delta_{\mathbb{D}}(\boldsymbol{\ell} + \boldsymbol{\ell}' + \boldsymbol{\ell}'')$ . One obtains

$$\begin{aligned} \langle X_{\ell m} X'_{\ell' m'} X''_{\ell'' m''} \rangle &= \begin{pmatrix} \ell & \ell' & \ell'' \\ m & m' & m'' \end{pmatrix} B_{XX'X''}(\ell, \ell', \ell'') \\ &\approx B_{XX'X''}^{\ell, \ell', \ell''} \int d\hat{\mathbf{n}} Y_\ell^{-m} Y_{\ell'}^{-m'} Y_{\ell''}^{-m''} \\ &\approx B_{XX'X''}^{\ell, \ell', \ell''} \begin{pmatrix} \ell & \ell' & \ell'' \\ 0 & 0 & 0 \end{pmatrix} \begin{pmatrix} \ell & \ell' & \ell'' \\ m & m' & m'' \end{pmatrix} \sqrt{\frac{(2\ell+1)(2\ell'+1)(2\ell''+1)}{4\pi}}. \end{aligned}$$

This implies the correspondence between the bispectra,

$$B_{XX'X''}(\ell, \ell', \ell'') = \begin{pmatrix} \ell & \ell' & \ell'' \\ 0 & 0 & 0 \end{pmatrix} \sqrt{\frac{(2\ell+1)(2\ell'+1)(2\ell''+1)}{4\pi}} B_{XX'X''}^{\ell, \ell', \ell''}. \quad (4.39)$$

## 4.7. Limber equation

Both of our two random fields of interest, the galaxy density fluctuation field  $\gamma(\hat{\theta})$  and the iSW temperature fluctuation  $\tau(\hat{\theta})$ , are line-of-sight integrated quantities,

$$\gamma(\hat{\theta}) = \int_0^{\chi_H} d\chi W_\gamma(\chi) \delta(\chi\hat{\theta}, \chi) \quad \text{and} \quad \tau(\hat{\theta}) = \int_0^{\chi_H} d\chi W_\tau(\chi) \varphi(\chi\hat{\theta}, \chi), \quad (4.40)$$

generated by the three dimensional source fields  $\delta(\chi\hat{\theta}, \chi)$  and  $\varphi(\chi\hat{\theta}, \chi)$  and weighted by the functions  $W_\gamma(\chi)$  and  $W_\tau(\chi)$ , respectively. Knowing the statistics of the 3d source fields, it is convenient to relate these to the 2d-statistics on the celestial sphere. This relation is given by the so-called Limber equation, which we will motivate here (Limber, 1953; Bartelmann & Schneider, 2001). As a first step, the angular correlator  $C_{XX}(\alpha)$  can directly be related to the power spectrum  $P^k$  of the density source field,

$$C_{XX}(\alpha) = \int_0^{\chi_H} d\chi W_X(\chi) \int_0^{\chi_H} d\chi' W_X(\chi') \int dk k^2 P^k(\chi, \chi') \int_{4\pi} d\Omega_k \exp(i\mathbf{k}(\mathbf{x} - \mathbf{x}')), \quad (4.41)$$

where  $\mathbf{x} = (\hat{\theta}\chi, \chi)$  denotes the spatial comoving coordinates and  $\Omega_k$  indicates the solid angle element in Fourier space. We remind that the power spectrum  $P^k(\chi, \chi')$  represents the Fourier transform of the real space correlation function, as it was defined in Section 2.4. Our aim is now to perform the angular integration. This can be done with help of the Rayleigh expansion, which expresses plane waves in terms of spherical harmonics,

$$\exp(i\mathbf{k}\mathbf{x}) = 4\pi \sum_{\ell=0}^{\infty} i^\ell j_\ell(kx) \sum_{m=-\ell}^{+\ell} Y_{\ell m}(\hat{k}) Y_{\ell m}^*(\hat{\theta}). \quad (4.42)$$

Using once more the addition theorem from eqn (4.27), we can now write the angular integral as

$$\begin{aligned} \int_{4\pi} d\Omega_k \exp(i\mathbf{k}(\mathbf{x} - \mathbf{x}')) &= (4\pi)^2 \sum_{\ell=0}^{\infty} j_\ell(k\chi) j_\ell(k\chi') \sum_{m=-\ell}^{+\ell} Y_{\ell m}(\hat{\theta}) Y_{\ell m}^*(\hat{\theta}') \\ &= 4\pi \sum_{\ell=0}^{\infty} j_\ell(k\chi) j_\ell(k\chi') (2\ell + 1) P_\ell(\cos \alpha). \end{aligned} \quad (4.43)$$

Plugging this into eqn. (4.41) for the angular correlator, one obtains

$$\begin{aligned} C_{XX}(\alpha) &= 4\pi \int_0^{\chi_H} d\chi W_X(\chi) \int_0^{\chi_H} d\chi' W_X(\chi') \int dk k^2 \times \\ &P^k(\chi, \chi') \sum_{\ell=0}^{\infty} j_\ell(k\chi) j_\ell(k\chi') (2\ell + 1) P_\ell(\cos \alpha). \end{aligned} \quad (4.44)$$

Multiplication with  $P_\ell(\cos \alpha)$  and integration over  $d(\cos \alpha)$  lead us to the so-called Limber equation for the angular power spectrum

$$C_{XX}^\ell = (4\pi)^2 \int_0^{\chi_H} d\chi W_X(\chi) \int_0^{\chi_H} d\chi' W_X(\chi') \int dk k^2 P^k(\chi, \chi') j_\ell(k\chi) j_\ell(k\chi'), \quad (4.45)$$

where again the orthonormality of the Legendre polynomials was used. For a slowly varying power spectrum  $P^k(\chi, \chi')$  in comparison to the spherical Bessel functions  $j_\ell(k\chi)$  an approximate projection can be found for the angular power spectrum (Limber, 1953),

$$C_{XX}^\ell \simeq \int_0^{\chi_H} \frac{d\chi}{\chi^2} W_X^2(\chi) P^k(\chi, \chi). \quad (4.46)$$

The approximation generally slightly overestimates the cross-power spectrum  $C_{\tau\gamma}^\ell$  by 10% (Rassat, 2009) in comparison to the exact expression in eqn. (4.45). This is, however, sufficient for the applications in this thesis.

# 5

## Chapter 5

# Integrated Sachs-Wolfe tomography with orthogonal polynomials

The topic of this chapter is the tomographic measurement of the integrated Sachs-Wolfe effect (iSW) with specifically designed, orthogonal polynomials that project out statistically independent modes of the galaxy distribution. The polynomials are constructed using the Gram-Schmidt orthogonalization method. To quantify the power of the iSW effect in constraining cosmological parameters, we perform a combined Fisher-matrix analysis for the iSW, galaxy and cross-spectra for  $w$ CDM cosmologies using the survey characteristics of *Planck* and *Euclid*. The signal-to-noise ratio has also been studied for other contemporary galaxy surveys, such as the Sloan Digital Sky Survey (SDSS), NRAO VLA Sky Survey (NVSS) and Two Micron All-Sky Survey (2MASS). For  $w = -0.9$  our tomographic method provides a 15% increase in the signal-to-noise ratio for the cross-spectra (10% for  $w = -1.0$ ) and an improvement of up to 30% in the conditional errors on the parameters for a *Euclid*-like galaxy survey. Including all spectra, the marginalized errors approach an inverse square-root dependence with increasing cumulative polynomial order, which underlines the statistical independence of the weighted signal spectra.

The results of this chapter are published in [Jürgens & Schäfer \(2012b\)](#).

## 5.1. Introduction

The integrated Sachs-Wolfe (iSW) effect, which has been introduced in Chapter 4, is one of the secondary anisotropies of the cosmic microwave background. It is a valuable tool for investigating dark energy and non-standard cosmologies since it is sensitive to fluids with non-zero equation of state ([Crittenden & Turok, 1996](#)). For this reason, its detection is of particular relevance for cosmology and our understanding of the nature of gravity ([Lue et al., 2004](#); [Zhang, 2006](#)) even if its signal strength is very low.

Since the iSW-effect is generated in time-evolving potential wells for photons on their way from the last scattering surface to us, it will be strongly correlated with the galaxy density field. Therefore, the cross-spectrum will provide valuable additional cosmological information. The iSW effect has been measured in such cross-correlation studies ([Boughn et al., 1998](#); [Boughn & Crittenden, 2004](#); [Vielva et al., 2006](#); [McEwen et al., 2007](#); [Giannantonio et al., 2008](#)). There are, however, doubts on detection claims formulated by [Hernández-Monteagudo \(2010\)](#) and [López-Corredoira et al. \(2010\)](#), who point out that the iSW-signal seems to be absent on low multipoles below 10, and that field-to-field fluctuations and sampling errors can be important. These facts may correct the detection significance to-date to a number less than two.

Due to the line-of-sight integration, a detailed distance resolution of the processes can not be extracted from these spectra. A previous approach correlated large scale structure observations from various surveys with the CMB anisotropies to study the iSW-effect as a function of redshift and to set

up a reliable likelihood formulation for parameter constraints (Ho et al., 2008). Also recently, Frommert et al. (2008) presented an optimal method to reduce the local variance effect and gained 7% in the signal-to-noise ratio for the cross-spectra.

In this work we aim to formulate a tomographic approach with the help of an orthogonal set of weighting polynomials, which is similar to a former application to weak lensing spectra (Schäfer et al., 2011). The orthogonality of the polynomials will generically lead to a diagonal signal covariance matrix and will therefore provide cumulative, statistically independent measurements with increasing polynomial order. In contrast to our approach, redshift-binning of the signal will diagonalize the noise part of the covariance if the assignment to the bins is exact. Increasing the number of polynomials and of redshift-bins sufficiently, both methods will lead to the same signal-to-noise ratio, since the methodical difference can be mathematically described by a simple change of basis system for the covariance. However, diagonalization of the signal covariance will illustrate how the signal builds up and how the covariance depends on cosmological parameters.

This chapter has the following structure: The orthogonal polynomials are motivated and constructed in Section 5.2.1 and 5.2.2, respectively. Their most important properties are discussed in Section 5.2.3. In Section 5.3 we discuss how tomography with orthogonal polynomials can improve statistical constraints on cosmological parameters. After calculating the noise contributions (Section 5.3.1) we perform a Fisher matrix analysis (Section 5.3.2) and discuss signal-to-noise ratios and statistical errors (Section 5.3.3-5.3.4). The results are summarized in Section 5.4.

The reference cosmological model used is a spatially flat  $w$ CDM cosmology with Gaussian adiabatic initial perturbations in the cold dark matter density field. The specific parameter choices are  $\Omega_m = 0.25$ ,  $n_s = 1$ ,  $\sigma_8 = 0.8$ ,  $\Omega_b = 0.04$  and  $H_0 = 100 h$  km/s/Mpc, with  $h = 0.72$ . The dark energy equation of state is set to  $w = -0.9$ .

## 5.2. Tomography with orthogonal polynomials

### 5.2.1. Motivation

Measurements of the iSW-effect provide integrated information about the structure formation history of our universe since the last scattering surface. Due to the fact that both the cross-correlation spectrum and the galaxy spectrum are line-of-sight integrated quantities, traces of interesting physical processes - as for example non-linear effects of parameters on the signal - could be averaged out. In this way valuable tomographical information would be lost. A counter example would be  $\sigma_8$ , which acts merely as a factor and does not change in its influence with redshift.

Tomographic methods split up the signal from different distances and are therefore able to increase the signal-to-noise ratio and the sensitivity with respect to cosmological parameters. In case of the galaxy spectra this implies that covariances between the different spectra have to be taken into account.

For a direct tomography in the line-of-sight integration of the iSW signal the knowledge of the large scale structure potential would be necessary. A reconstruction of the potential from the observed galaxy field, however, would not reach the required accuracy due to the inversion of the Poisson equation. Also the poor statistics of the galaxy spectrum for large modes should be a problem for a thorough reconstruction.

To circumvent this issue we perform tomography in the galaxy field and cross-correlate it with the iSW signal. Thereby, we are able to extract tomographical information also from the iSW signal. We use specifically designed polynomials for a distance weighting of the galaxy distribution. Defining the weighted galaxy covariances as a scalar product of the polynomials will lead to statistically independent galaxy spectra once the polynomials are orthogonalized. This non-local binning of the galaxies leads to a diagonalization of the galaxy signal covariance matrix. The polynomials can then also be used for tomographical measurements in the iSW-galaxy cross-correlations.

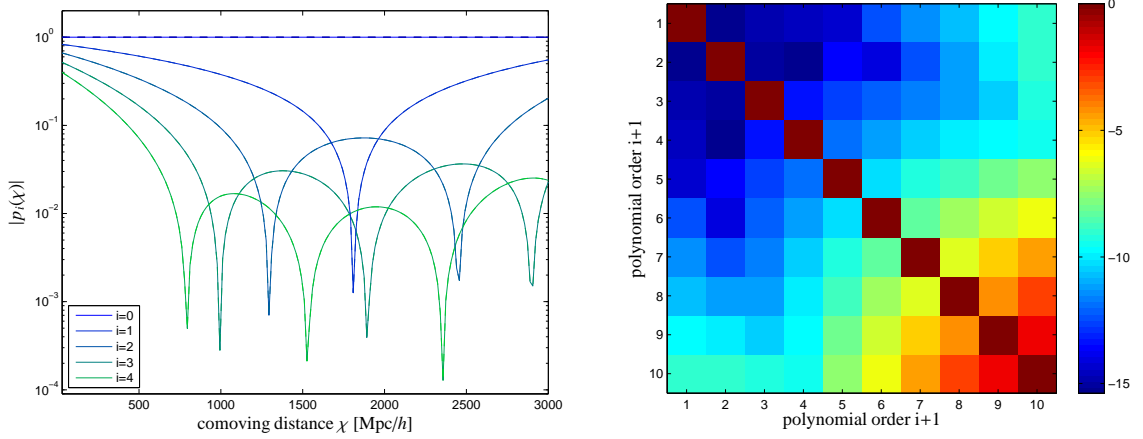


**Figure 5.1.:** *Left panel:* Orthogonal polynomials  $p_i(\chi)$ ,  $i = 0..4$ , as a function of comoving distance  $\chi$ . The construction was performed with the Gram-Schmidt algorithm at multipole order  $\ell = 100$ . The lowest order polynomial is shown in blue, the highest order in green. *Right panel:* Numerical accuracy for the orthogonality relation  $\langle p_i, p_j \rangle$  at  $\ell = 20$  in logarithmic representation. The accuracy imposes a limit on the number of included polynomials.

### 5.2.2. Construction of orthogonal sets of polynomials

Weighting the given galaxy distribution function  $n(\chi) = n(z) dz/d\chi = n(z) H(z)/c$  with a polynomial  $p_i(\chi)$  modifies the galaxy weighting function to

$$W_\gamma^{(i)}(\chi) = p_i(\chi) W_\gamma(\chi) = p_i(\chi) n(z) \frac{H(z)}{c} D_+(z). \quad (5.1)$$

For the polynomials  $p_i(\chi)$  and  $p_j(\chi)$  we require orthogonality

$$\langle p_i, p_j \rangle = 0 \text{ for } (i \neq j) \quad (5.2)$$

with respect to the following scalar product for the polynomials,

$$\langle p_i, p_j \rangle \equiv S_{\gamma\gamma}^{(ij)}(\ell) \equiv \int_0^{\chi_H} \frac{d\chi}{\chi^2} W_\gamma^{(i)}(\chi) W_\gamma^{(j)}(\chi) P^{k=\ell/\chi}. \quad (5.3)$$

As in Chapter 4 we work also here in the flat sky approximation, which was found to provide results within 10% accuracy on the relatively large iSW-relevant scales ( $\ell > 10$ ) (Rassat, 2009). The scalar product depends on the multipole order  $\ell$  and is constructed such that modes contributing to the auto-spectra are independent. The necessary properties for a scalar product are obviously fulfilled ( $\langle p_i, p_i \rangle \geq 0$ ,  $\langle p_i, p_i \rangle = 0 \Leftrightarrow p_i \equiv 0$  and linearity). We use the Gram-Schmidt procedure to construct orthogonal polynomials out of the family of monomials

$$p'_i(\chi) = \left( \frac{\chi}{\chi_{\text{node}}} \right)^i, \quad (5.4)$$

where  $\chi_{\text{node}}$  sets the position of the node of the first polynomial. It is in our case set to the median value of the redshift distribution. However, a change in  $\chi_{\text{node}}$  is completely absorbed in the coefficient and has no influence on the polynomials. Starting with the zero-order monomial

$$p_0(\chi) = p'_0(\chi) \equiv 1, \quad (5.5)$$

the polynomials are constructed iteratively,

$$p_i(\chi) = p'_i(\chi) - \sum_{j=0}^{i-1} \frac{\langle p'_i, p_j \rangle}{\langle p_j, p_j \rangle} p_j(\chi). \quad (5.6)$$

The procedure has to be performed for every multipole  $\ell$ . The dependence of the polynomials  $p_i(\chi)$  on  $\ell$  has been omitted for clarity. As one can see, the zero-order scalar product is equal to the galaxy spectrum,

$$\langle p_0, p_0 \rangle = S_{\gamma\gamma}(\ell). \quad (5.7)$$

Therefore, the unweighted case is already contained in the first weighting function. Finally, we can weight also the tracer density modes  $\gamma(\ell)$  themselves with a polynomial  $p_i(\chi)$ ,

$$\gamma^{(i)}(\ell) = \int_0^{\chi_H} d\chi W_\gamma^{(i)}(\chi) \delta(\ell, \chi), \quad (5.8)$$

for which a generalized version of the well known expression for the covariance holds in case of homogeneous and isotropic random fields,

$$\langle \gamma^{(i)}(\ell) \gamma^{(j)*}(\ell') \rangle = (2\pi)^2 \delta_D(\ell - \ell') S_{\gamma\gamma}^{(ij)}(\ell) \quad (5.9)$$

with  $S_{\gamma\gamma}^{(ij)}(\ell) \propto \delta_{ij}$ .

### 5.2.3. Properties of orthogonal polynomials

In Fig. 5.1 the orthogonal polynomials are shown up to a polynomial order of  $i = 4$ . They show an increasing number of roots roughly at the positions where the previous polynomial reaches a local maximum or minimum, which illustrates their orthogonality.

As one can see in Fig. 5.1 orthogonality is fulfilled until numerical limitations become significant at a polynomial order of  $q \approx 9$ . The increasing numerical deviations from the orthogonality condition ( $\langle p_i, p_j \rangle = 0$  for  $i \neq j$ ) is due to the iterative method, which cumulates errors throughout the process. This implies the accuracy to shrink from  $10^{-15}$  for  $i = 0$  to  $10^{-3}$  for  $i = 8$ . This is a well known disadvantage of the Gram-Schmidt orthogonalization method, especially when dealing with functions as opposed to vectors, since there is larger numerical noise in the evaluation of the scalar products. However, as we shall see later, it is not necessary for our application to go to even higher orders.

In Fig. 5.2 the weighted galaxy efficiency functions  $W_\gamma^{(i)}(\chi)$  are depicted, which are modified by the polynomials  $p_i(\chi)$  at the arbitrarily chosen multipole  $\ell = 20$ . The case  $i = 0$  refers to the weighting function without tomography,  $W_\gamma^{(0)}(\chi) = W_\gamma(\chi)$ . One can easily observe the order of the polynomial hierarchy at the distant end of the functions, where one after another approaches zero.

The modified spectra  $C_{\gamma\gamma}^{(ii)}(\ell)$  and  $C_{\tau\gamma}^{(i)}(\ell)$  are shown in Fig. 5.3. The drop in amplitude is mainly an effect of the absence of normalization, while one can in fact observe slight differences in shape. However, these differences are small, since the polynomials only mildly depend on the multipole order  $\ell$ . Therefore, the overall shape of the spectra is still dominated by the zero-order spectra  $C_{\gamma\gamma}^{(00)}(\ell)$  and  $C_{\tau\gamma}^{(0)}(\ell)$ , respectively. Thanks to the orthogonalization these spectra now provide statistically independent information. In the next section we aim to combine signals from the galaxy distribution, the iSW-effect and the cross-spectra to investigate statistical bounds on cosmological parameters.

For the cosmological parameters under consideration - except the equation of state parameter  $w$  - we choose values close to the best-fitting parameters:  $\Omega_m = 0.25$ ,  $n_s = 1$ ,  $\sigma_8 = 0.8$ ,  $\Omega_b = 0.04$  and  $H_0 = 100 h$  km/s/Mpc, with  $h = 0.72$ . Later, in the Fisher matrix formalism the derivatives of the covariance matrix with respect to the cosmological parameters are needed and Fisher ellipses are drawn around the reference values. To keep the cosmological model outside the physical phantom region for values  $w < -1$ , we used  $w = -0.9$  as reference value. In Fig. 5.3 the iSW cross-spectra

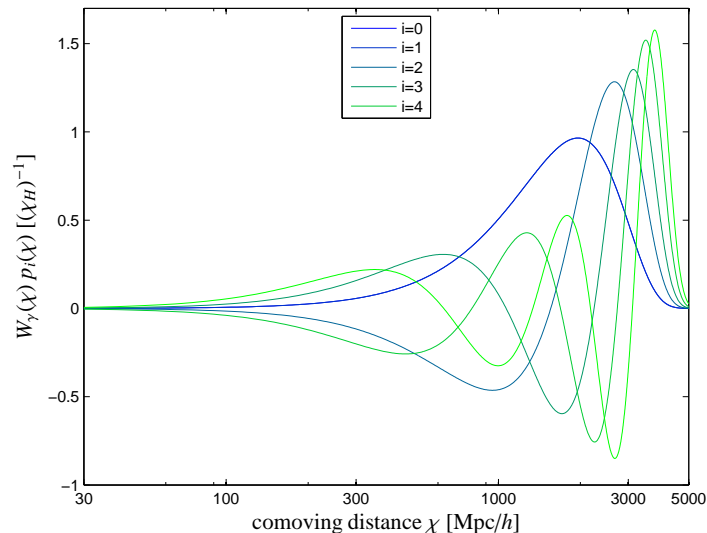


**Figure 5.2.:** Weighted galaxy efficiency functions  $W_\gamma^{(i)}(\chi)$ ,  $i = 0..4$ , as a function of comoving distance at multipole order  $\ell = 20$ .

are shown for both equation of state parameters  $w = -0.9$  (solid lines) and  $w = -1.0$  (dashed lines). Since a lower value of  $w$  damps linear structure formation, also the correlations are smaller than for  $w = -0.9$ . While the spectrum  $C_{\tau\gamma}^{(0)}(\ell)$  is changed by only 10%, the damping increases to higher polynomial orders to 70% for  $C_{\tau\gamma}^{(8)}(\ell)$ . However, since the spectra show the same characteristic behavior, the qualitative improvement due to our tomographical method should be similar to the case  $w = -0.9$ .

## 5.3. Statistics

This section aims to connect cosmic variance and statistical noise with the iSW-signal and its cross-correlations into a meaningful statistical formulation. We construct covariance matrices for the polynomial-weighted spectra. Statistical errors on cosmological parameters are estimated in the Fisher-matrix formalism. Furthermore, we investigate the signal strength of the different spectra and their dependence on the number of polynomials used.

### 5.3.1. Variances of galaxy number counts

For forecasting statistical errors, we need to derive expressions for the signal covariance and noise. We will start from a discrete formulation with a set of weighting coefficients  $w_m$  for the counted galaxy number  $m$ . Clearly, the weighting coefficient  $w_m$  will depend on the distance of the respective galaxy. Later, we will generalize the formalism to the continuous case, in which the weighting procedure is performed by the polynomials  $p_i(\chi)$ . The standard deviation  $\sigma_{ww}$  of a weighted galaxy count with weighting coefficients  $w_m$  is given by

$$\sigma_{ww}^2 = \frac{1}{\sum_m w_m \sum_n w_n} \sum_{m,n} w_m w_n \delta_{mn} \quad (5.10)$$

with the Kronecker delta  $\delta_{mn}$ . This reduces to a Poissonian result in the case of  $w_m$  being either 0 or 1,

$$\sigma_{ww}^2 = \frac{1}{\bar{n}} \quad \text{with} \quad \bar{n} = \sum_n w_n. \quad (5.11)$$

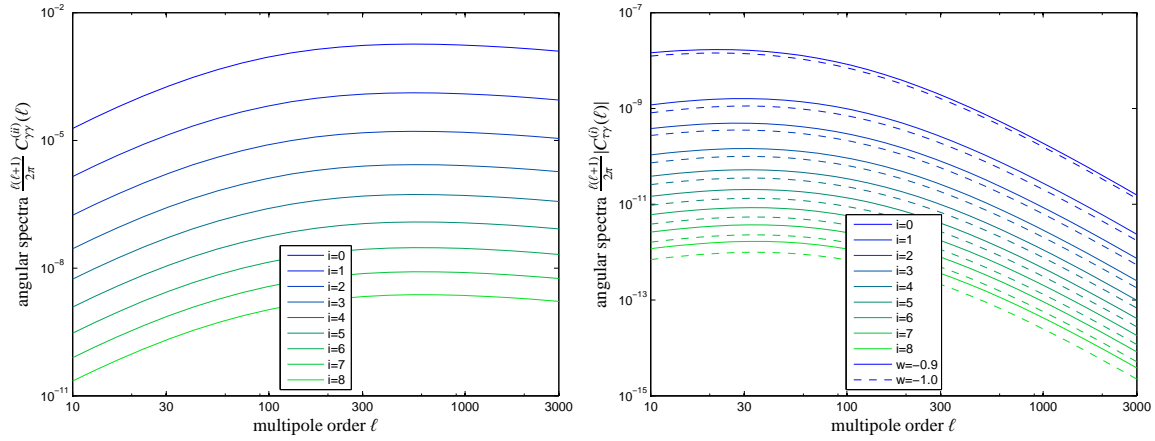


**Figure 5.3.:** *Left Panel:* Pure galaxy-galaxy spectra  $S_{\gamma\gamma}^{(ii)}(\ell)$ ,  $i = 0..8$ , weighted with orthogonal polynomials  $p_i(\chi)$ , as a function of the multipole order  $\ell$ .  $S_{\gamma\gamma}^{(00)}(\ell)$  (blue) refers to the non-tomographic spectrum  $S_{\gamma\gamma}(\ell)$ . One can see a decrease in amplitude for increasing multipole order  $\ell$ .

*Right panel:* Galaxy-iSW cross-spectra  $C_{\gamma\gamma}^{(i)}(\ell)$ ,  $i = 0..8$ , weighted with orthogonal polynomials  $p_i(\chi)$ , as a function of the multipole order  $l$  for  $w = -0.9$  (solid lines) and  $w = -1.0$  (dashed lines).  $C_{\gamma\gamma}^{(0)}(\ell)$  (blue) refers to the non-tomographic spectrum  $C_{\gamma\gamma}(\ell)$ .

The counted quantity  $\bar{n}$  in our case is defined as the mean density of galaxies per steradian, for which we will substitute  $\bar{n} = 40/\text{arcmin}^2$ , which is characteristic for the *Euclid* galaxy survey. Considering two different sets of weighting factors  $w_m$  and  $v_n$ , we generalize the standard deviation to

$$\sigma_{wv}^2 = \frac{1}{\sum_m w_m \sum_n v_n} \sum_m w_m v_m, \quad (5.12)$$

which will in the continuum limit be a cross-variance weighted with two different polynomials. For the continuum limit the transition

$$\sum_m \dots \rightarrow \bar{n} \int d\chi n(\chi) \dots \quad (5.13)$$

is performed which conserves the total number count  $\bar{n}$  due to the unit normalized galaxy distribution function  $n(\chi)$ . The discrete weighting sets  $w_m$  and  $v_n$  are then represented by  $p_i(\chi)$  and  $p_j(\chi)$  so that the noise covariance in the continuous case reads

$$N_{\gamma\gamma}^{(ij)}(\ell) \equiv \sigma_{ij}^2 = \frac{1}{\bar{n}} \frac{\int d\chi n(\chi) p_i(\chi) p_j(\chi)}{\int d\chi n(\chi) p_i(\chi) \int d\chi n(\chi) p_j(\chi)}. \quad (5.14)$$

The noise term  $N_{\gamma\gamma}^{(ij)}(\ell)$  still depends on  $\ell$  since the polynomials are constructed for each multipole order separately. We omit the  $\ell$ -dependence of the polynomials  $p_i(\chi)$  for clarity. Eqn. (5.14) motivates the following choice of normalization for our polynomials,

$$p_i(\chi) \leftarrow \frac{p_i(\chi)}{\int d\chi n(\chi) p_i(\chi)}. \quad (5.15)$$

In this normalization the galaxy number noise reads

$$N_{\gamma\gamma}^{(ij)}(\ell) = \frac{1}{\bar{n}} \int d\chi n(\chi) p_i(\chi) p_j(\chi), \quad (5.16)$$

while the galaxy spectrum can be written as

$$S_{\gamma\gamma}^{(ij)}(\ell) = \int_0^{\chi_H} \frac{d\chi}{\chi^2} W_\gamma^{(i)}(\chi) W_\gamma^{(j)}(\chi) P^{k=\ell/\chi}. \quad (5.17)$$

The limitation in polynomial order due to increasing noise in the polynomials  $p_i(\chi)$  can already be illustrated. Since  $n(\chi)$  is a slowly varying function the rapid oscillations of high order polynomials will drive the values of the integrals  $\int d\chi n(\chi) p_i(\chi)$  to smaller numbers and will therefore increase the noise in  $p_i(\chi)$ . We point out that for order zero the non-tomographic case is recovered, giving the standard Poissonian expression for the noise  $N_{00} = 1/\bar{n}$  and the integrated galaxy spectrum in the signal part  $S_{\gamma\gamma}^{(00)}(\ell) = S_{\gamma\gamma}(\ell)$ .

While the orthogonalization procedure leads to a diagonal galaxy signal covariance, the noise part will not be diagonal any more,  $N_{\gamma\gamma}^{(ij)} \neq 0$  for  $i \neq j$ . Contrary to this method, a traditional binning in  $z$  would lead to a diagonal noise contribution and off-diagonals in the signal part.

### 5.3.2. Fisher analysis

In order to use both iSW signals and galaxy spectra in our Fisher analysis, we now define an extended data vector

$$\mathbf{x}(\ell) = \begin{pmatrix} \tau(\ell) \\ \gamma^{(i)}(\ell) \end{pmatrix}. \quad (5.18)$$

The total covariance matrix,  $\mathbf{C}(\ell) = \mathbf{S}(\ell) + \mathbf{N}(\ell)$ , for these data vectors is block-diagonal due to the independence of the  $\ell$ -modes: Each block

$$\mathbf{C}(\ell) = \begin{pmatrix} C_{\tau\tau}(\ell) & C_{\tau\gamma}^{(j)}(\ell) \\ C_{\tau\gamma}^{(i)}(\ell) & C_{\gamma\gamma}^{(ij)}(\ell) \end{pmatrix} \quad (5.19)$$

consists of a signal part

$$\mathbf{S}(\ell) = \begin{pmatrix} S_{\tau\tau}(\ell) & C_{\tau\gamma}^{(j)}(\ell) \\ C_{\tau\gamma}^{(i)}(\ell) & S_{\gamma\gamma}^{(ij)}(\ell) \end{pmatrix}, \quad (5.20)$$

where  $S_{\gamma\gamma}^{(ij)}(\ell) \propto \delta_{ij}$  by construction, and a noise contribution

$$\mathbf{N}(\ell) = \begin{pmatrix} N_{\tau\tau}(\ell) & 0 \\ 0 & N_{\gamma\gamma}^{(ij)}(\ell) \end{pmatrix} \quad (5.21)$$

with polynomial orders  $0 \leq i, j \leq q$ . Due to uncorrelated noise in the CMB and the galaxy density field the noise of the cross-spectra vanishes. The CMB part consists of the pure iSW signal

$$S_{\tau\tau}(\ell) = \int_0^{\chi_H} \frac{d\chi}{\chi^2} W_\tau^2(\chi) P_{\phi\phi}^{k=\ell/\chi} \quad (5.22)$$

with  $P_{\phi\phi}^{k=\ell/\chi} = P^k / (\chi_H k)^4$  while the noise can be split into the primary CMB fluctuations  $C_{\text{CMB}}(\ell)$  and an instrumental noise term  $C_{\text{beam}}(\ell)$  of *Planck* (Planck Collaboration et al., 2011),

$$N_{\tau\tau}(\ell) = C_{\text{CMB}}(\ell) + \omega^{-1} \exp(-\Delta\theta^2 \ell^2), \quad (5.23)$$

with the beam size  $\Delta\theta = 8.77 \times 10^{-4}$  and the squared pixel noise  $\omega^{-1} = 0.2 \mu\text{K}/T_{\text{CMB}}$  (Knox, 1995). The noiseless cross-spectra are formed by one modified weighting function only,

$$C_{\tau\gamma}^{(i)}(\ell) = \int_0^{\chi_H} \frac{d\chi}{\chi^2} W_\tau(\chi) W_\gamma^{(i)}(\chi) P_{\delta\phi}^{k=\ell/\chi} \quad (5.24)$$

with  $P_{\delta\phi}^k = P^{k=\ell/\chi} / (k\chi_H)^2$ . We point out that only the galaxy part of the signal covariance was diagonalized by our method. Consequently, the cross-spectra  $C_{\tau\gamma}^{(i)}(\ell)$  are the only off-diagonal entries in the covariance matrix.

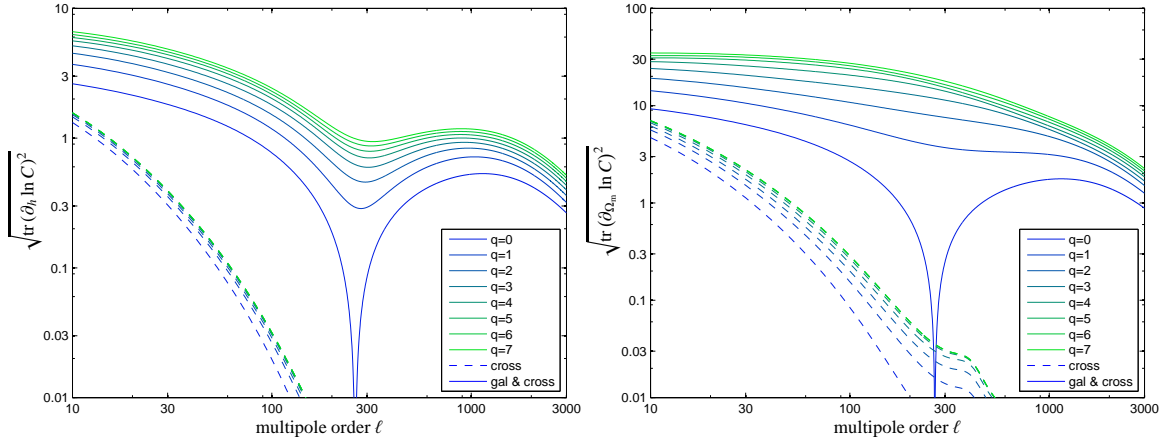


**Figure 5.4.:** Sensitivity of the Fisher matrix with respect to the Hubble parameter  $h$  (left panel) and the matter density parameter  $\Omega_m$  (right panel) as a function of the multipole order  $\ell$ , and cumulative polynomial order  $q$ . Sensitivities are shown with derivatives of all spectra taken into account (solid lines) in comparison to the case where only the cross-spectra were considered in the signal part (dashed lines). For the covariance the survey properties of *Euclid* have been assumed.

Assuming a centered Gaussian random field  $\mathbf{x}(\ell)$ , the likelihood for observing the modes  $\mathbf{x}(\ell)$  for a given parameter set  $\mathbf{p}$  is defined as (Tegmark et al., 1997):

$$\mathcal{L}(\mathbf{x}(\ell) | \mathbf{p}) = \frac{1}{\sqrt{(2\pi)^N \det \mathbf{C}(\ell)}} \exp\left(-\frac{1}{2} \mathbf{x}^T(\ell) \mathbf{C}^{-1}(\ell) \mathbf{x}^*(\ell)\right). \quad (5.25)$$

We define the data matrix as  $D_{ij}(\ell) = x_i(\ell) x_j^*(\ell)$  with  $\langle \mathbf{D} \rangle = \mathbf{C}$ . One can write the  $\chi^2$ -functional  $\mathcal{L} \propto \exp(-\chi^2/2)$  with the help of the logarithmic likelihood  $L \equiv -\ln \mathcal{L}$ ,

$$\chi^2 = 2L = \text{tr} \sum_{\ell} [\ln \mathbf{C} + \mathbf{C}^{-1} \mathbf{D}], \quad (5.26)$$

where the relation  $\ln \det(\mathbf{C}) = \text{tr} \ln(\mathbf{C})$  was used. Each multipole  $\ell$  provides  $(2\ell + 1)$  independent  $m$ -modes. Assuming also the likelihood as a function of parameters  $p_\nu$  to be Gaussian around the most likelihood estimate  $p_{\nu, \text{fid}}$ , it is determined by the Hesse matrix of  $L$  at this point, which is given by the inverse parameter covariance matrix,

$$(T^{-1})_{\mu\nu} \equiv \frac{\partial^2 L}{\partial p_\mu \partial p_\nu}. \quad (5.27)$$

The Fisher information matrix is then given as the expectation value of this quantity summed over all angular wave numbers  $\ell$ ,

$$F_{\mu\nu} = \left\langle \frac{\partial^2 L}{\partial p_\mu \partial p_\nu} \right\rangle = \sum_{\ell} \frac{2\ell + 1}{2} \text{tr} \left( \frac{\partial}{\partial p_\mu} \ln \mathbf{C}(\ell) \frac{\partial}{\partial p_\nu} \ln \mathbf{C}(\ell) \right). \quad (5.28)$$

For each  $\ell$  the  $(2\ell + 1)$   $m$ -modes provide statistically independent information. In the course of our Fisher matrix calculations we will work in the limit  $\partial S_{ij}/\partial p_\mu \gg \partial N_{ij}/\partial p_\mu$  and therefore neglect the noise dependence on the cosmological parameters. This approximation is well justified in our case, since the noise can be considered independent of the cosmological parameters.

Next we have a look at the ratio of the sensitivities of the spectra with respect to cosmological parameters and the covariance. This quantity equals the contribution of a certain angular wave number  $\ell$  to the respective Fisher matrix diagonal element,

$$\sqrt{\text{tr} \left( \frac{\partial \ln \mathbf{C}(\ell)}{\partial p_\mu} \right)^2} = \sqrt{\frac{2}{2\ell + 1} \frac{dF_{\mu\mu}}{d\ell}}, \quad (5.29)$$

where derivative is taken with respect to the absolute value  $\ell$  of the flat sky wave number  $\ell$ , which should not be mistaken for a discrete multipole order. In Fig. 5.4 we show these sensitivities as solid lines for the full information from galaxy spectra, cross-spectra and iSW-effect included for the parameters  $h$  and  $\Omega_m$ , respectively. At zero order they all exhibit a certain  $\ell$ -range where the covariance is insensitive to variations of the respective cosmological parameter. Mathematically, at these  $\ell$ -values the covariance matrix assumes an extremal value with respect to the respective parameter  $p_\mu$ . Physically, in the line-of-sight integration the response of a certain  $\chi$ -range on a change in the parameter  $p_\mu$  cancels the response of the complementary  $\chi$ -range. Naturally, angular scales in the vicinity of this zero point do not contribute much sensitivity to the Fisher matrix. This effect is cured if we include all polynomials  $0 \leq i \leq q$ . The combination of multiple line-of-sight-weighted measurements lifts the sensitivities at these points continuously with increasing number of involved polynomials until the effect saturates.

For multipole orders  $\ell$  reaching higher values ( $\ell \approx 3000$ ) the sensitivity drops rapidly. On these small scales the noise contribution begins to dominate and the Fisher matrix ceases to grow further.

In dashed lines the sensitivities are shown if only the cross-spectra are included in the derivatives. Again the sensitivities grow with increasing cumulative polynomial order  $q$ , although in this case the zero order sensitivity does not suffer from any singular effects. Characteristic properties of the iSW-effect are recovered showing it to be a large scale effect due to the  $k^{-2}$  proportionality originating in the Poisson equation. Above multipoles of about  $l \approx 100$  the information provided by the cross-spectra becomes negligible. Clearly, the cross-spectra Fisher matrix is most sensitive to the matter density parameter  $\Omega_m$ , which shows the strongest increase in sensitivity for increasing cumulative polynomial order  $q$ .

### 5.3.3. Signal-to-noise ratio

A signal's power to constrain cosmological parameters is most reliably quantified by the signal-to-noise ratio

$$\Sigma^2 = f_{\text{sky}} \sum_{\ell} \frac{2\ell + 1}{2} \text{tr}(\mathbf{C}^{-1}(\ell) \mathbf{S}(\ell))^2. \quad (5.30)$$

Apart from the physical process the signal-to-noise ratio strongly depends on the characteristics of the survey at hand. In the case of galaxy surveys the most important survey parameters are the sky coverage  $f_{\text{sky}}$  and the median redshift  $z_{\text{med}}$ . In Fig 5.5 the signal-to-noise ratios for the survey characteristics of *Euclid*, 2MASS ( $z_{\text{med}} \approx 0.1$ , Afshordi et al., 2004), SDSS ( $z_{\text{med}} \approx 0.5$ , Bielby et al., 2010) and NVSS ( $z_{\text{med}} \approx 1.2$ , Boughn & Crittenden, 2005) are shown. Here, only the cross-spectra were included in the signal covariance. Clearly, also the signal-to-noise ratio increases for higher polynomial orders due to the diagonal structure of the signal covariance. For instance, for *Euclid* we find an improvement of  $\approx 15\%$  in the signal-to-noise ratio between cumulative polynomial orders  $q = 1$  and  $q = 8$ . As expected, at a multipole order of a few hundred the cumulative signal strength saturates as a result of the Poissonian  $k^{-2}$  damping term in the iSW-effect. The signal-to-noise ratio can be calculated also for an equation of state parameter of  $w = -1.0$ . The comparison to the case  $w = -0.9$  for the tomographical signal-to-noise ratio improvement is shown in Fig. 5.5. While at  $w = -0.9$  the signal-to-noise ratio improves by 15%, the improvement reduces to 10% in the case of  $w = -1.0$ .

The actual realization of the matter distribution in the observed universe introduces a systematic noise in the iSW detections known as local variance. Using the so called optimal method one can decrease this bias by working conditional on the large scale structure data and gain 7% in signal-to-noise ratio (Frommert et al., 2008). The tomographical method presented in our work should be also applicable to the reconstructed large scale structure used in the optimal method. Therefore, a combination of these two methods would be sensible.

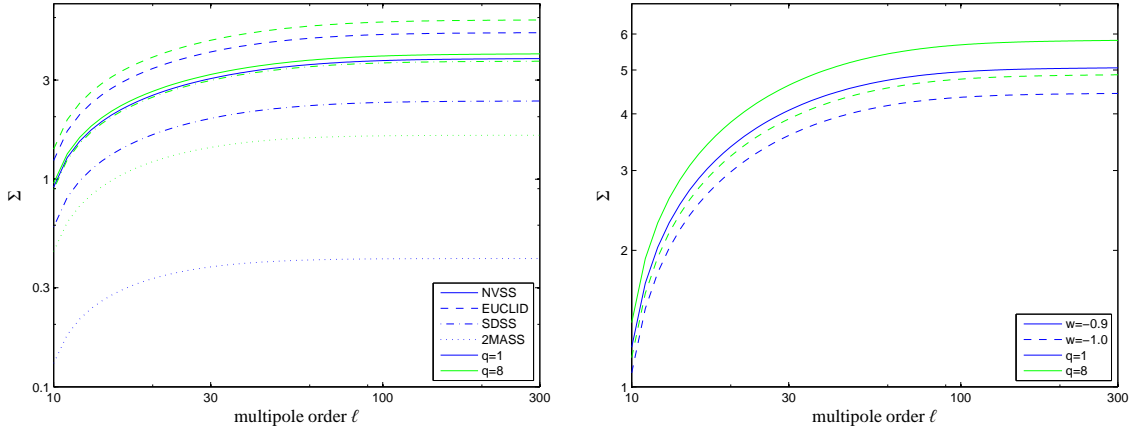


**Figure 5.5.:** *Left Panel:* Cumulative signal-to-noise ratio  $\Sigma$  depending on the multiple-order  $\ell$  with only cross-spectra included in the signal covariance. It is shown for the different survey characteristics of 2MASS (dotted), SDSS (dashed-dotted), *Euclid* (dashed) and NVSS (solid). Shown is the improvement between cumulative polynomial order  $q = 1$  (blue) and  $q = 8$  (green). *Right Panel:* Cumulative signal-to-noise ratio  $\Sigma$  depending on the multiple-order  $\ell$  with only cross-spectra included in the signal covariance. It is shown for the survey characteristics of *Euclid* for  $w = -0.9$  (solid lines) and  $w = -1.0$  (dashed lines). Shown is the improvement between cumulative polynomial order  $q = 1$  (blue) and  $q = 8$  (green).

### 5.3.4. Statistical errors

The Cramér-Rao inequality introduces a lower bound on the marginalized standard deviation of the estimated cosmological parameters. These are given by the diagonal elements of the inverse Fisher matrix:

$$\sigma_{\mu} \geq \left( (F^{-1})_{\mu\mu} \right)^{\frac{1}{2}}. \quad (5.31)$$

In Fig. 5.6 these errors are depicted for the five cosmological parameters  $\Omega_m$ ,  $\sigma_8$ ,  $h$ ,  $n_s$  and  $w$ . The plot follows the evolution of the errors with increasing number of included polynomials  $q$ . While for small polynomial orders the Cramér-Rao errors decrease rapidly with different characteristics for each parameter, the improvement slows down for higher order polynomials and assumes a characteristic behavior. This behavior can approximately be described by the inverse root of the polynomial order  $\sigma_{\mu} \propto 1/\sqrt{q}$ . A similar characteristic was found in the application of this method to the weak lensing shear spectra (Schäfer et al., 2011). Clearly, the cosmological parameter  $\Omega_m$  profits most from the tomographic method, which was already indicated by its sensitivity improvement discussed in Section 5.3.2. Going to even higher orders is difficult due to cumulative errors in the Gram-Schmidt orthogonalization method.

If we are interested in how a single cosmological parameter can be constrained assuming that all other parameters are fixed, we have to study the conditional errors. These can be obtained from the inverse diagonal elements of the Fisher matrix,

$$\sigma_{\mu, \text{con}} = (F_{\mu\mu})^{-\frac{1}{2}}. \quad (5.32)$$

For studying the improvement provided by the cross-spectra, we plot the conditional errors as a function of cumulative polynomial order  $q$  in Fig. 5.6. Here, only the derivatives of the cross-spectra were taken into account in the Fisher matrix calculation. Again  $\Omega_m$  experiences the strongest improvement, its conditional error decreases by  $\approx 30\%$ . In contrast to the marginalized errors the evolution of the conditional errors does not show a  $1/\sqrt{q}$  behavior but rather saturates at polynomial order of  $q \approx 5$ .

Finally, we are interested in the 2d-marginalized logarithmic likelihood  $\chi_m^2$  around the fiducial

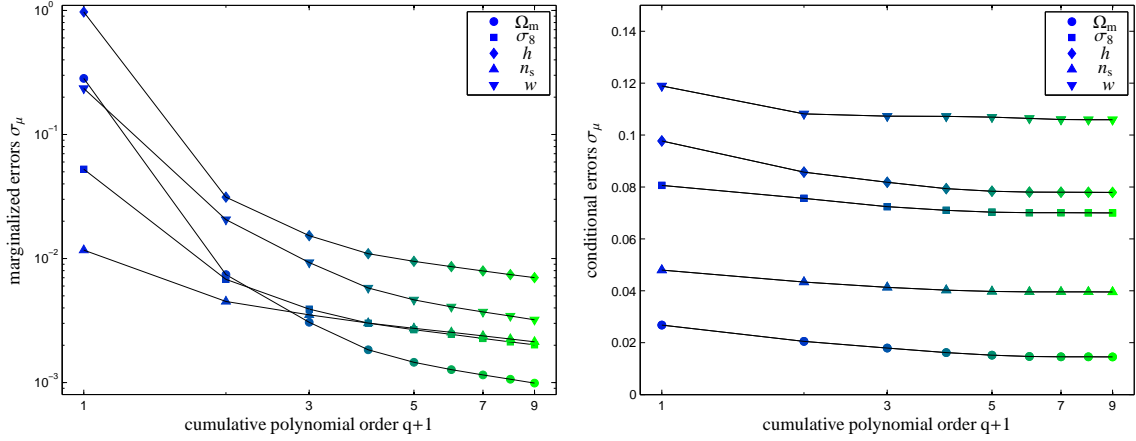


**Figure 5.6.:** *Left Panel:* Lower limits on the marginalized statistical errors  $\sigma_\mu$  on the estimates of the cosmological parameters  $\Omega_m$  (circles),  $\sigma_8$  (squares),  $h$  (lozenges),  $n_s$  (triangles, pointing up) and  $w$  (triangles, pointing down) derived from the Cramér-Rao inequality, as a function of the cumulative polynomial order  $q$ . The Fisher matrix was derived including the derivatives of all spectra  $C_{\gamma\gamma}^{(ii)}(\ell)$ ,  $C_{\tau\gamma}^{(i)}(\ell)$  and  $C_{\tau\tau}(\ell)$ . Again, the *Euclid* survey characteristics have been used.

*Right Panel:* Conditional statistical errors  $\sigma_{\mu,\text{con}}$  on the estimates of the cosmological parameters  $\Omega_m$  (circles),  $\sigma_8$  (squares),  $h$  (lozenges),  $n_s$  (triangles, pointing up) and  $w$  (triangles, pointing down). The Fisher matrix was derived including the derivatives of the cross-spectra  $C_{\tau\gamma}^{(i)}(\ell)$  only, *Euclid* survey characteristics have been used.

model  $p_{\text{fid}}$

$$\chi_m^2 = \begin{pmatrix} p_\mu - p_{\mu,\text{fid}} \\ p_\nu - p_{\nu,\text{fid}} \end{pmatrix}^T \begin{pmatrix} (F^{-1})_{\mu\mu} & (F^{-1})_{\mu\nu} \\ (F^{-1})_{\nu\mu} & (F^{-1})_{\nu\nu} \end{pmatrix} \begin{pmatrix} p_\mu - p_{\mu,\text{fid}} \\ p_\nu - p_{\nu,\text{fid}} \end{pmatrix}, \quad (5.33)$$

for which the  $1\sigma$ -error ellipses are depicted in Fig. 5.7 with both galaxy-galaxy spectra and cross-spectra included in the signal. Starting with  $q = 2$ , we have combined up to nine polynomials. Besides the expected shrinking of the ellipses for higher numbers of included polynomials, it is interesting to see how the degeneracies slightly change their orientations in the course of tomographic improvement. This is very likely due to distance dependences of the signal sensitivities.

## 5.4. Summary

In this paper a tomographic method for measuring iSW-galaxy cross-spectra and galaxy spectra has been presented. It has been carried out by line-of-sight-weighting of the tracer density field with specifically constructed orthogonal polynomials.

(i) The Gram-Schmidt orthogonalization procedure has been used to construct orthogonal polynomials in order to diagonalize the weighted galaxy signal covariance. The method projects out statistically independent signal contributions at the price of off-diagonals in the noise part. It differs from traditional tomographical approaches, for instance from most tomographical techniques in weak lensing measurements, in which the noise part is diagonalized. Due to cumulative numerical errors with increasing polynomial order, this method is limited to order  $i \approx 8$ .

(ii) The improvement of the signal-to-noise ratios with cumulative polynomial order was investigated for the galaxy surveys 2MASS (Afshordi et al., 2004), SDSS (Bielby et al., 2010), NVSS (Boughn & Crittenden, 2005) and *Euclid*. In the case of *Euclid* the signal-to-noise ratio for the cross-spectra only has been improved by 15% for  $w = -0.9$  (10% for  $w = -1.0$ ) at a cumulative polynomial order of  $q = 8$ .

(iii) A Fisher-matrix analysis was used to forecast how well cosmological parameters can be constrained by different galaxy surveys, combining signals from the iSW-effect as well as from the tracer

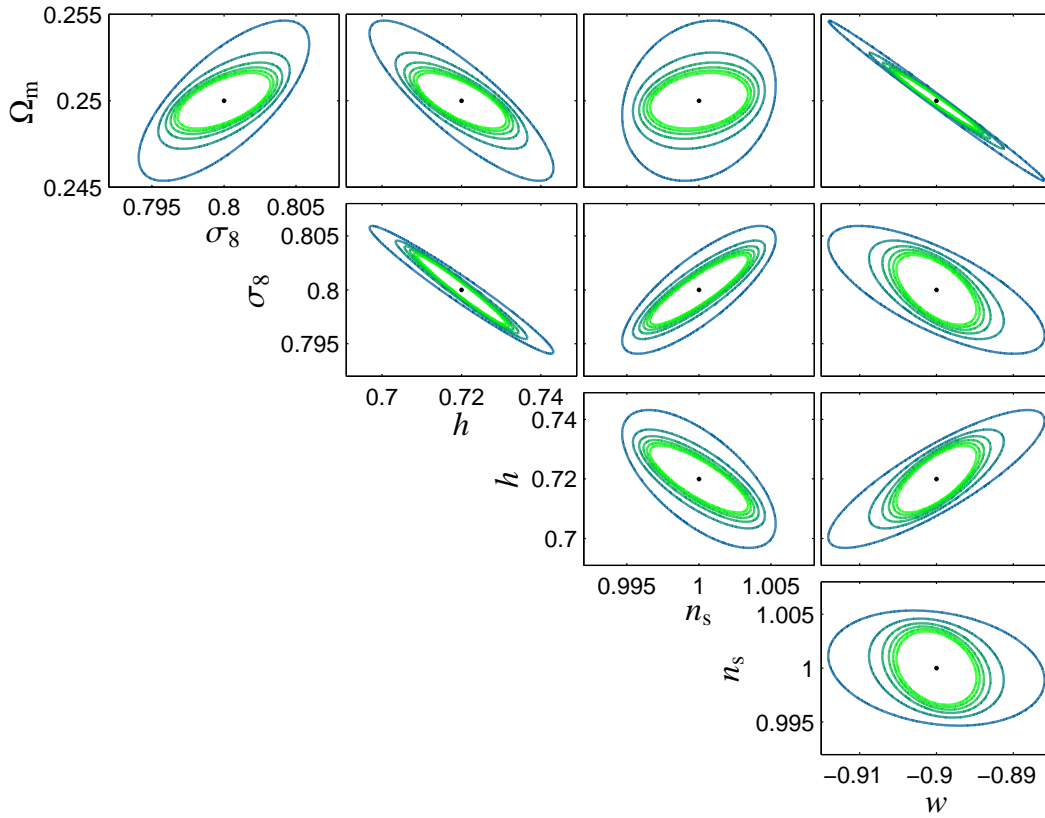


**Figure 5.7.:** The  $1\sigma$ -error ellipses in two dimensions for the cosmological parameters  $\Omega_m$ ,  $\sigma_8$ ,  $h$ ,  $n_s$  and  $w$  from *Euclid* using tomography with orthogonal polynomials are shown in this plot. The full information from the galaxy-galaxy spectra and cross-spectra were used for this plot. The  $1\sigma$  confidence regions decrease in size with increasing number of included polynomials, reaching from  $q = 2$  (blue) to  $q = 8$  (green). The ellipses are evaluated with a maximum multipole order of  $\ell_{\max} = 3000$ .

density field. The marginalized errors show simple inverse square-root behavior with increasing number of included polynomials, which can be interpreted also as a sign of the statistically independent signal contributions. Conditional errors on parameters constrained only by the cross-spectra decrease by up to  $\approx 30\%$  in case of the matter density parameter  $\Omega_m$ .

(iv) While for the cross-spectra only the conditional errors show a saturation already at quite low number of included polynomials  $q \approx 5$ , it would still be worth improving this method in order to reach even higher orders, since marginalized errors for the full signal did not yet saturate at cumulative order of  $q = 8$ .

(v) Using the wrong cosmological model in the construction of the polynomials can introduce an estimation bias on cosmological parameters. This effect was thoroughly studied in a similar approach for weak lensing measurements (Schäfer et al., 2011). In most cases the bias was found to be small compared to the statistical errors. Since, in addition, iteration between parameter estimation and polynomial construction is able to further reduce this bias, a wrongly chosen cosmology appears unlikely to affect measurements.

# 6

## Chapter 6

# Cross-bispectra and cross-trispectra of the non-linear integrated Sachs-Wolfe effect and the tracer galaxy density field

In order to investigate possibilities to measure non-Gaussian signatures of the non-linear iSW effect, we study in this chapter the family of mixed bispectra  $\langle \tau^q \gamma^{3-q} \rangle$  and trispectra  $\langle \tau^q \gamma^{4-q} \rangle$  between the integrated Sachs-Wolfe (iSW) temperature perturbation  $\tau$  and the galaxy over-density  $\gamma$ . We use standard Eulerian perturbation theory restricted to tree level expansion for predicting the cosmic matter field. As expected, the spectra are found to decrease in amplitude with increasing  $q$ . The transition scale between linear domination and the scales, on which non-linearities take over, moves to larger scales with increasing number of included iSW source fields  $q$ . We derive the cumulative signal-to-noise ratios for a combination of *Planck* CMB data and the galaxy sample of a *Euclid*-like survey. Including scales down to  $\ell_{\max} = 1000$  we find sobering values of  $\sigma \simeq 0.83$  for the mixed bispectrum and  $\sigma \simeq 0.19$  in case of the trispectrum for  $q = 1$ . For higher values of  $q$  the polyspectra  $\langle \tau^2 \gamma \rangle$  and  $\langle \tau^3 \gamma \rangle$  are found to be far below the detection limit.

The results of this chapter are published in [Jürgens & Schäfer \(2012a\)](#).

## 6.1. Introduction

The linear iSW effect, which was topic of Chapters 4-5, is a large scale effect and becomes negligible at angular wave numbers above  $\ell \sim 100$ . The effect from non-linear evolution of the gravitational potential, also called Rees-Sciama effect ([Rees & Sciama, 1968](#)), leaves signatures on much smaller scales and surpasses the linear iSW-effect in this range. The possible signatures of this effect in angular power spectrum have been thoroughly studied analytically ([Martinez-Gonzalez et al., 1994](#); [Sanz et al., 1996](#); [Seljak, 1996b](#); [Schäfer & Bartelmann, 2006](#)). The effect increases the total iSW signal by roughly two orders of magnitude at angular scales around  $\ell \sim 1000$  ([Cooray, 2002](#)), before gravitational lensing and kinetic Sunyaev-Zel'dovich effect become dominant at even smaller scales. However, comparisons of theoretical studies with numerical simulations showed the Rees-Sciama effect to be negligible in comparison with primary anisotropies on angular scales larger than  $\theta > 1'$  ([Tuluie & Laguna, 1995](#); [Seljak, 1996b](#)). Also from cross-correlations of the CMB with weak lensing surveys only a detection significance of  $\sim 1.5\sigma$  from *Planck*+LSST is expected ([Nishizawa et al., 2008](#)).

One option to obtain direct signatures of non-Gaussianities is the investigation of higher order connected correlators ([Schäfer, 2008](#)). In this chapter we aim to formulate a perturbative approach of the mixed iSW-galaxy polyspectra, concentrating on the tree-level bispectra and trispectra in flat sky approximation. The unequal rate of linear and non-linear evolution at different scales will lead to interesting sign changes in the spectra, which will also be apparent in the non-trivial time evolution

of the different source field contributions. In addition, we will study the signal-to-noise spectra for measurements expected from *Planck* CMB data in cross-correlation with observations from a *Euclid*-like survey assuming unbiased measurements with Gaussian noise contributions. We revisit a previous estimate of the observability of the iSW-bispectrum (Schäfer, 2008) correcting an error in the expression for the spectrum of the gravitational potential and because of the significantly improved signal-to-noise computation, which uses an adaptive Monte-Carlo integration scheme (Hahn, 2005) instead of a binned summation over the multipoles.

The chapter has the following structure: In Section 6.2 the non-linear iSW-effect is introduced. The mixed bispectra and trispectra are discussed in Section 6.3, with specific studies of their weighting functions (Section 6.3.4) and their time evolution (Section 6.3.5). In Section 6.4 we present the relevant noise sources (Section 6.4.1), the resulting covariances (Section 6.4.2) of the polyspectra and finally derive their signal-to-noise ratios (Section 6.4.3). Our results are summarized and discussed in Section 6.5.

The reference cosmological model is a spatially flat  $\Lambda$ CDM cosmology with Gaussian adiabatic initial perturbations in the cold dark matter density field. The specific parameter choices are  $\Omega_m = 0.25$ ,  $n_s = 1$ ,  $\sigma_8 = 0.8$ ,  $\Omega_b = 0.04$  and  $H_0 = 100 h$  km/s/Mpc, with  $h = 0.72$ . The dark energy equation of state is set to  $w = -1.0$ .

## 6.2. Non-linear iSW-effect

As we know from Section 4.4, the temperature fluctuations  $\tau(\hat{\theta})$  generated by the iSW-effect can be expressed by the line-of-sight integral (Sachs & Wolfe, 1967),

$$\tau(\boldsymbol{\theta}) \equiv \frac{\Delta T_{\text{iSW}}}{T_{\text{CMB}}} = \frac{2}{c^3} \int_0^{\chi_H} d\chi a^2 H(a) \frac{\partial}{\partial a} \Phi(\boldsymbol{\theta}\chi, \chi), \quad (6.1)$$

reaching out to the limit of Newtonian gravity. Using the Poisson equation we can write this integral in terms of the dimensionless potential  $\phi = \Delta^{-1} \delta/\chi_H^2$  of the density field  $\delta(\boldsymbol{\theta}\chi, \chi)$ . The  $n$ -th perturbative order of the iSW temperature fluctuation  $\tau = \tau^{(1)} + \tau^{(2)} + \dots$  can now be written as

$$\tau^{(n)}(\boldsymbol{\theta}) = \frac{3\Omega_m}{c} \int_0^{\chi_H} d\chi a^2 H(a) \frac{\Delta^{-1}}{\chi_H^2} \left( \frac{d}{da} \frac{D_+^{(n)}}{a} \right) \delta(\boldsymbol{\theta}\chi, \chi), \quad (6.2)$$

where the Laplacian and the term including the growth function could be exchanged, since  $D_+(a)$  does not depend on space. The linear effect ( $n = 1$ ) vanishes identically in matter dominated universes  $\Omega_m = 1$ , since then  $D_+/a$  is a constant. Therefore, a non-zero iSW-signal will be an indicator of a cosmological fluid with  $w \neq 0$ . After the radiation dominated era it will thus be a valuable tool for investigating dark energy cosmologies. The non-linear contributions ( $n \geq 2$ ) are now sourced by time derivatives of the higher perturbative orders of the gravitational potential. Therefore, the Rees-Sciama effect is also present in SCDM-cosmology.

In order to identify the sources of the effect it is sensible to investigate the cross correlation of the iSW amplitude with the line-of-sight projected relative galaxy over-density  $\gamma = \gamma^{(1)} + \gamma^{(2)} + \dots$ ,

$$\gamma^{(n)}(\boldsymbol{\theta}) = b \int_0^{\chi_H} d\chi n(z) \frac{dz}{d\chi} D_+^n \delta(\boldsymbol{\theta}\chi, \chi). \quad (6.3)$$

Since we are interested in rather small scales, where non-linear effects appear, we work in the flat sky approximation<sup>9</sup>,

$$\gamma(\boldsymbol{\ell}) = \int d^2\theta \gamma(\boldsymbol{\theta}) e^{-i(\boldsymbol{\ell} \cdot \boldsymbol{\theta})}. \quad (6.4)$$

<sup>9</sup>see also Section 4.6

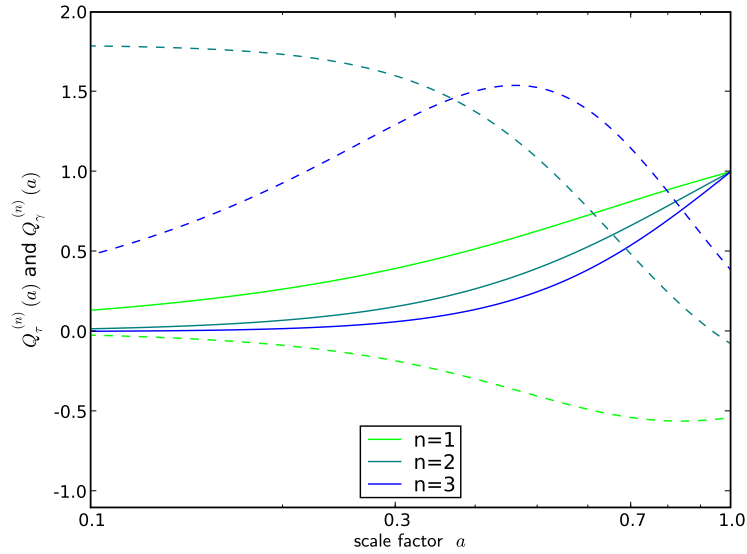


**Figure 6.1.:** Time evolution functions  $Q_\gamma^{(n)}(a)$  (solid lines) and  $Q_\tau^{(n)}(a)$  (dashed lines) as a function of the scale factor  $a$  for different perturbative orders  $n = 1, 2, 3$ .

The observable  $\tau$  can be transformed in an analogous way. For later notational convenience we define the two weighting functions

$$\begin{aligned} W_\gamma(\chi) &= b n(z) \frac{dz}{d\chi} \\ W_\tau(\chi) &= 3 \Omega_m a^2 \frac{H}{c} \end{aligned} \quad (6.5)$$

and the time evolution functions to  $n$ -th order

$$\begin{aligned} Q_\gamma^{(n)}(a) &= D_+^n \\ Q_\tau^{(n)}(a) &= \frac{d}{da} \left( \frac{D_+^n}{a} \right). \end{aligned} \quad (6.6)$$

In Fig. 6.1 the time evolution functions  $Q_\gamma^{(n)}(a)$  and  $Q_\tau^{(n)}(a)$  are depicted in dependence on the scale factor  $a$ . It is particularly interesting to observe the different signs. While the galaxy spectra are always positive, the iSW contributions change their signs with perturbative order. As we will later observe, also the signs of  $n$ -point functions will change consequently in the transition from large scales, where the linear theory is valid, to small scales, where non-linearities start to dominate. For the cross-bispectrum, this effect has already been studied (Nishizawa et al., 2008).

## 6.3. Cross-bispectra and cross-trispectra

### 6.3.1. The density polyspectra

Regardless of the existence of initial non-Gaussianities in the density field  $\delta(\mathbf{k})$ , non-linear structure formation leads to non-vanishing three-point and higher order correlators due to quadratic terms in the continuity and Euler equation. Since a Gaussian random field can uniquely be represented by its two-point correlator  $\xi(r) = \langle \delta(\mathbf{x})\delta(\mathbf{x} + \mathbf{r}) \rangle$ , multi-point correlators represent a convenient measure of

evolving non-Gaussianities. The Fourier transforms of these 2-point and 3-point correlators are the bispectrum  $B_\delta^{k_1, k_2, k_3}$  and the trispectrum  $T_\delta^{k_1, k_2, k_3, k_4}$

$$\begin{aligned}\langle \delta(\mathbf{k}_1)\delta(\mathbf{k}_2)\delta(\mathbf{k}_3) \rangle &= (2\pi)^3 \delta_D(\mathbf{k}_{1\dots 3}) B_\delta^{k_1, k_2, k_3} \\ \langle \delta(\mathbf{k}_1)\delta(\mathbf{k}_2)\delta(\mathbf{k}_3)\delta(\mathbf{k}_4) \rangle_c &= (2\pi)^3 \delta_D(\mathbf{k}_{1\dots 4}) T_\delta^{k_1, k_2, k_3, k_4},\end{aligned}\quad (6.7)$$

where the Dirac  $\delta_D$ -function occurs as a result of homogeneity.

### 6.3.2. Limber Projection

In the flat sky approximation one can use a simplified Limber projection<sup>10</sup> (Limber, 1953) to relate the 3d-source spectra  $B_\delta^{k_1, k_2, k_3}$  and  $T_\delta^{k_1, k_2, k_3, k_4}$  to the angular spectra  $B_\gamma^{\ell_1, \ell_2, \ell_3}$  and  $T_\gamma^{\ell_1, \ell_2, \ell_3, \ell_4}$ .

$$\begin{aligned}B_\gamma^{\ell_1, \ell_2, \ell_3} &= \int_0^{\chi_H} d\chi \frac{1}{\chi^4} W_\gamma^3(\chi) D_+^4(a) B_\delta^{k_1, k_2, k_3} \\ T_\gamma^{\ell_1, \ell_2, \ell_3, \ell_4} &= \int_0^{\chi_H} d\chi \frac{1}{\chi^6} W_\gamma^4(\chi) D_+^6(a) T_\delta^{k_1, k_2, k_3, k_4}.\end{aligned}\quad (6.8)$$

Then, equivalent formulae as in eqn. (6.7) apply to these angular polyspectra, which are then related to the projected density field  $\gamma(\boldsymbol{\ell})$  with 2d-angular wave vectors  $\boldsymbol{\ell}_i$ :

$$\begin{aligned}\langle \gamma(\boldsymbol{\ell}_1)\gamma(\boldsymbol{\ell}_2)\gamma(\boldsymbol{\ell}_3) \rangle &= (2\pi)^3 \delta_D(\boldsymbol{\ell}_{1\dots 3}) B_\gamma^{\ell_1, \ell_2, \ell_3} \\ \langle \gamma(\boldsymbol{\ell}_1)\gamma(\boldsymbol{\ell}_2)\gamma(\boldsymbol{\ell}_3)\gamma(\boldsymbol{\ell}_4) \rangle &= (2\pi)^3 \delta_D(\boldsymbol{\ell}_{1\dots 4}) T_\gamma^{\ell_1, \ell_2, \ell_3, \ell_4},\end{aligned}\quad (6.9)$$

where the fields on the sphere with angular directions  $\mathbf{n}_i$  are simply decomposed into Fourier harmonics instead of spherical harmonics,

$$\langle \gamma(\mathbf{n}_1)\dots\gamma(\mathbf{n}_n) \rangle = \int \frac{d^2\ell_1}{(2\pi)^2} \dots \int \frac{d^2\ell_n}{(2\pi)^2} \cdot \langle \gamma(\boldsymbol{\ell}_1)\dots\gamma(\boldsymbol{\ell}_n) \rangle e^{i\boldsymbol{\ell}_1 \cdot \mathbf{n}_1} \dots e^{i\boldsymbol{\ell}_n \cdot \mathbf{n}_n}.\quad (6.10)$$

Since the region on a sphere around a certain point can for small angles be approximated by the tangential plane, this is a good approximation for high  $\ell$ -values. It can generally be transformed to the full sky representation with Wigner 3j-symbols (Hu, 2001).

### 6.3.3. Mixed iSW-galaxy polyspectra

An equivalent procedure of definitions as in the previous subsection can be applied to the iSW-fields  $\tau(\boldsymbol{\ell})$ . However, due to the uncorrelated noise sources in the iSW and galaxy fields mixed spectra are of predominant interest to us. If there exists a chance to securely measure the iSW signal it will only work via its cross-correlation to the projected galaxy density field  $\gamma(\boldsymbol{\ell})$  in the two-point function and higher order functions.

To allow for a compact definition of the mixed spectra we introduce a doublet field  $\varphi_i(\boldsymbol{\ell})$ ,

$$\begin{pmatrix} \varphi_0(\boldsymbol{\ell}) \\ \varphi_1(\boldsymbol{\ell}) \end{pmatrix} = \begin{pmatrix} \gamma(\boldsymbol{\ell}) \\ \tau(\boldsymbol{\ell}) \end{pmatrix}.\quad (6.11)$$

Mixed spectra can now be defined in a compact way

$$\begin{aligned}\langle \varphi_{i_1}(\boldsymbol{\ell}_1)\varphi_{i_2}(\boldsymbol{\ell}_2)\varphi_{i_3}(\boldsymbol{\ell}_3) \rangle &= (2\pi)^3 \delta_D(\boldsymbol{\ell}_{1\dots 3}) B_{i_1 i_2 i_3}^{\ell_1, \ell_2, \ell_3} \\ \langle \varphi_{i_1}(\boldsymbol{\ell}_1)\varphi_{i_2}(\boldsymbol{\ell}_2)\varphi_{i_3}(\boldsymbol{\ell}_3)\varphi_{i_4}(\boldsymbol{\ell}_4) \rangle &= (2\pi)^3 \delta_D(\boldsymbol{\ell}_{1\dots 4}) T_{i_1 i_2 i_3 i_4}^{\ell_1, \ell_2, \ell_3, \ell_4}.\end{aligned}\quad (6.12)$$

<sup>10</sup>These are higher dimensional generalizations of the Limber equation introduced in Section 4.7

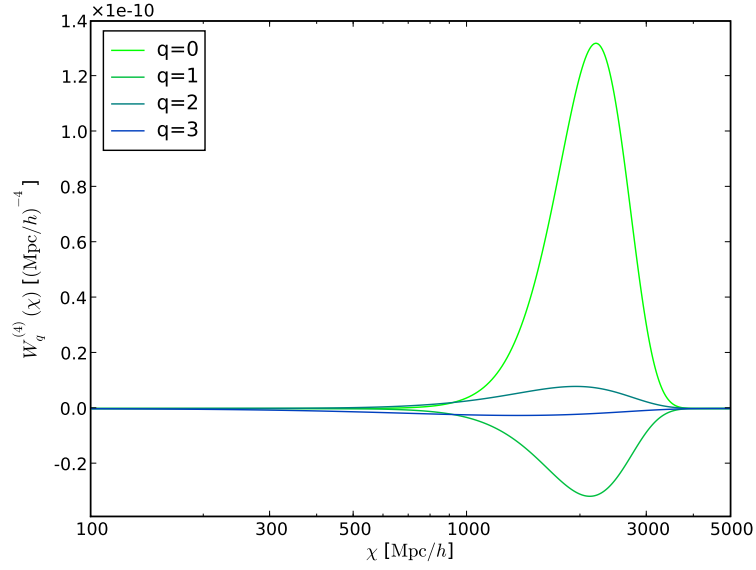


**Figure 6.2.:** Line-of-sight weighting functions  $W_q^{(4)}(\chi)$  for mixed iSW-galaxy trispectra as a function of comoving distance.

### 6.3.4. Weighting functions

For a mixed  $n$ -point function, the product of the  $n$  different weighting functions, is uniquely given by the sum  $q$  of the field indices  $i_1 \dots i_n$ . In case of the bispectrum we would define  $q = i_1 + i_2 + i_3$ , whereas in case of the trispectrum  $q = i_1 + i_2 + i_3 + i_4$ . We can therefore define a  $q$ -dependent combined weighting function  $W_q^{(n)}(\chi)$ ,

$$W_q^{(n)}(\chi) = W_\tau^q(\chi) W_\gamma^{n-q}(\chi), \quad (6.13)$$

where  $n = 3$  and  $n = 4$  correspond to the bispectra and trispectra, respectively. The different weightings in case of the trispectra are depicted in Fig. 6.2 for different field mixtures  $q$ . Although the weightings show strong differences in amplitude and sign, a broad peak between 1 and 4 Gpc  $h^{-1}$  is common to all weightings due to the maximum in the galaxy redshift distribution  $p(z)$ .

### 6.3.5. Time evolution

The time evolution of each linear galaxy field  $\gamma(a, \mathbf{k})$  is given by the growth function  $D_+(a)$ . The  $n$ -th non-linear perturbative contributions evolve simply with the  $n$ -th order of the growth function  $D_+^n$ . This is not the case for the iSW field contributions  $\tau(a, \mathbf{k})$ . While the linear term evolves proportional to  $d(D_+/a)/da$  the higher orders can not just be written as the  $n$ -th power of the linear growth but are proportional to  $d(D_+^n/a)/da$ .

Due to this, different perturbative contributions to the mixed bispectra and trispectra will in general not have the same time evolution. In order to obtain a compact notation we introduce the time evolution doublet to  $n$ -th order  $\mathcal{Q}^{(n)}(a)$ ,

$$\mathcal{Q}^{(n)}(a) = \begin{pmatrix} \mathcal{Q}_0^{(n)}(a) \\ \mathcal{Q}_1^{(n)}(a) \end{pmatrix} = \begin{pmatrix} D_+^n \\ \frac{d}{da} \left( \frac{D_+^n}{a} \right) \end{pmatrix}. \quad (6.14)$$

With these time evolution functions  $\mathcal{Q}^{(n)}(a)$  we can write down the general mixed time evolving source

fields. For the tree-level bispectra we define

$$\begin{aligned}
 B_{i_1 i_2 i_3}^{k_1, k_2, k_3} &= (\chi_H k_1)^{-2i_1} (\chi_H k_2)^{-2i_2} (\chi_H k_3)^{-2i_3} \\
 &\left( Q_{i_1}^{(2)}(a) Q_{i_2}^{(1)}(a) Q_{i_3}^{(1)}(a) b_\delta^{k_2, k_3} \right. \\
 &+ Q_{i_2}^{(2)}(a) Q_{i_3}^{(1)}(a) Q_{i_1}^{(1)}(a) b_\delta^{k_3, k_1} \\
 &\left. + Q_{i_3}^{(2)}(a) Q_{i_1}^{(1)}(a) Q_{i_2}^{(1)}(a) b_\delta^{k_1, k_2} \right). \quad (6.15)
 \end{aligned}$$

The terms  $(\chi_H k_1)^{-2i}$  are the Poisson factors from the iSW effect. In case of the tree-level trispectrum the source will consist of two contributions - one originating from second order and third order perturbation theory respectively. The time dependent source for the trispectra then reads

$$\begin{aligned}
 T_{i_1 i_2 i_3}^{k_1, k_2, k_3, k_3} &= (\chi_H k_1)^{-2i_1} (\chi_H k_2)^{-2i_2} (\chi_H k_3)^{-2i_3} (\chi_H k_4)^{-2i_4} \\
 &\left( Q_{i_1}^{(2)}(a) Q_{i_2}^{(2)}(a) Q_{i_3}^{(1)}(a) Q_{i_4}^{(1)}(a) t_\delta^{(2)}(k_1, k_2, (k_3, k_4)) + \text{allpairs} \in \{1, 2, 3, 4\} \right. \\
 &\left. + Q_{i_1}^{(3)}(a) Q_{i_2}^{(1)}(a) Q_{i_3}^{(1)}(a) Q_{i_4}^{(1)}(a) t_\delta^{(3)}(k_1, k_2, k_3, k_4) + \text{cyclic} \{1, 2, 3, 4\} \right). \quad (6.16)
 \end{aligned}$$

Now, the flat sky Limber equations for the mixed angular bispectra and trispectra read (Hu, 2001)

$$\begin{aligned}
 B_{i_1 i_2 i_3}^{\ell_1, \ell_2, \ell_3} &= \int_0^{\chi_H} d\chi \frac{1}{\chi^4} W_q^{(3)}(\chi) B_{i_1 i_2 i_3}^{k_1, k_2, k_3} \\
 T_{i_1 i_2 i_3 i_4}^{\ell_1, \ell_2, \ell_3, \ell_4} &= \int_0^{\chi_H} d\chi \frac{1}{\chi^6} W_q^{(4)}(\chi) T_{i_1 i_2 i_3 i_4}^{k_1, k_2, k_3, k_4}, \quad (6.17)
 \end{aligned}$$

where the source field spectra are evaluated at the 3d-wave vectors  $\mathbf{k}_i = (l_{i,1}, l_{i,2}, 0)$ . Since the weighting functions are slowly varying in comparison to the source field, fluctuations in the line-of-sight direction are smoothed out by the integrations. Therefore, the fields can be assumed as non-fluctuating in this direction in the first place.

While pure spectra are invariant under exchange of wave vectors  $\ell_i$ ,

$$\begin{aligned}
 B_{aaa}^{\ell_1, \ell_2, \ell_3} &= B_{aaa}^{\ell_2, \ell_3, \ell_1} = B_{aaa}^{\ell_3, \ell_1, \ell_2} \\
 T_{aaaa}^{\ell_1, \ell_2, \ell_3, \ell_4} &= T_{aaaa}^{\ell_2, \ell_3, \ell_4, \ell_1} = T_{aaaa}^{\ell_3, \ell_4, \ell_1, \ell_2} = T_{aaaa}^{\ell_4, \ell_1, \ell_2, \ell_3}, \quad (6.18)
 \end{aligned}$$

this does not generally apply for the mixed spectra  $B_{abc}^{\ell_a, \ell_b, \ell_c}$ . In general, all spectra are invariant under a simultaneous exchange of wave numbers and field indices,

$$\begin{aligned}
 B_{i_1 i_2 i_3}^{\ell_1, \ell_2, \ell_3} &= B_{i_2 i_3 i_1}^{\ell_2, \ell_3, \ell_1} = B_{i_3 i_1 i_2}^{\ell_3, \ell_1, \ell_2} \\
 T_{i_1 i_2 i_3 i_4}^{\ell_1, \ell_2, \ell_3, \ell_4} &= T_{i_2 i_3 i_4 i_1}^{\ell_2, \ell_3, \ell_4, \ell_1} = T_{i_3 i_4 i_1 i_2}^{\ell_3, \ell_4, \ell_1, \ell_2} = T_{i_4 i_1 i_2 i_3}^{\ell_4, \ell_1, \ell_2, \ell_3}. \quad (6.19)
 \end{aligned}$$

These symmetries are simply caused by the commutation invariance in the products of source fields in eqn. (6.7).

### 6.3.6. Equilateral bispectra and square trispectra

To require homogeneity the wave vector arguments have to form a triangle,  $\ell_1 + \ell_2 + \ell_3 = 0$ , for the bispectrum and a quadrangle,  $\ell_1 + \ell_2 + \ell_3 + \ell_4 = 0$ , in case of the trispectrum. Thus, due to isotropy the scale dependence of the bispectrum is uniquely defined by the absolute values of the angular wave vectors  $\ell_i$ ,

$$B_{abc}^{\ell_a, \ell_b, \ell_c} = B_{abc}^{\ell_a, \ell_b, \ell_c}. \quad (6.20)$$

The scale dependence of the trispectra, however, can be described by the four absolute values of the angular wave vectors  $\ell_i$  and one diagonal  $L$ ,

$$T_{abc}^{\ell_a, \ell_b, \ell_c, \ell_d} = T_{abc}^{\ell_a, \ell_b, \ell_c, \ell_d, L}. \quad (6.21)$$

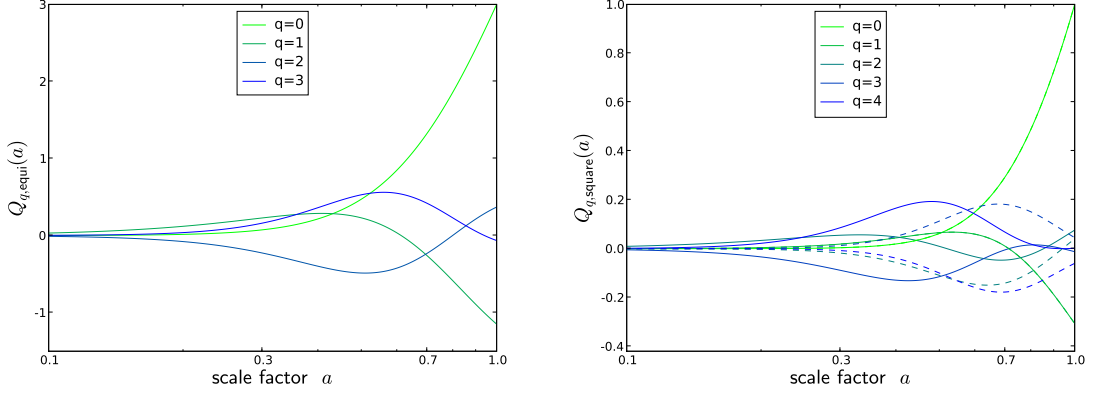


**Figure 6.3.:** *Left panel:* Time evolution functions for equilateral mixed iSW-galaxy bispectra  $B_{i_1 i_2 i_3}^{\ell, \ell, \ell}$  as a function of angular scale  $\ell$ . The value  $q = i_1 + i_2 + i_3$  defines the mixture of the source fields. *Right panel:* Time evolution functions for square mixed iSW-galaxy trispectra  $T_{(i_1 i_2 i_3 i_4)}^{\ell, \ell, \ell, \ell, \sqrt{2}\ell}$  as a function of angular scale  $\ell$ . The value  $q = i_1 + i_2 + i_3 + i_4$  defines the mixture of the source fields. The solid lines depict the second order perturbative time evolutions  $Q_{q, square}^{(2)}$ , the third order terms  $Q_{q, square}^{(3)}$  are shown as dashed lines. While the growth functions of the galaxy distribution stay positive to all perturbative orders, the derivatives in the iSW evolution functions also introduce negative terms into the evolution.

This leads to the fact that the source fields of equilateral bispectra are symmetric with respect to their field indices and have a uniform time evolution  $Q_{q, equi}(a)$ ,

$$Q_{q, equi} = \begin{cases} D_+^3 & (q = 0) \\ \frac{1}{3} D_+^2 \left( \frac{d}{da} \frac{D_+^2}{a} \right) + \frac{2}{3} D_+^3 \left( \frac{d}{da} \frac{D_+}{a} \right) & (q = 1) \\ \frac{2}{3} D_+ \left( \frac{d}{da} \frac{D_+^2}{a} \right) \left( \frac{d}{da} \frac{D_+}{a} \right) + \frac{1}{3} D_+^2 \left( \frac{d}{da} \frac{D_+}{a} \right)^2 & (q = 2) \\ \left( \frac{d}{da} \frac{D_+^2}{a} \right) \left( \frac{d}{da} \frac{D_+}{a} \right)^2 & (q = 3) \end{cases} . \quad (6.22)$$

These time evolutions are depicted in Fig. 6.3. While the growth functions of the galaxy distribution stay positive to all perturbative orders, the derivatives in the iSW evolution functions also introduce negative terms into the evolution. This will later lead to a change from correlation to anti-correlation along the line-of-sight.

Slightly more complex is the time evolution for source fields of the square trispectra. Here, the contributions from second order perturbation theory evolve still differently compared to the third order terms. The second order terms  $Q_{q, square}^{(2)}(a)$  read

$$Q_{q, square}^{(2)} = \begin{cases} D_+^6 & (q = 0) \\ \frac{1}{2} D_+^4 \left( \frac{d}{da} \frac{D_+^2}{a} \right) + \frac{1}{2} D_+^5 \left( \frac{d}{da} \frac{D_+}{a} \right) & (q = 1) \\ \frac{1}{6} D_+^4 \left( \frac{d}{da} \frac{D_+}{a} \right)^2 + \frac{2}{3} D_+^3 \left( \frac{d}{da} \frac{D_+^2}{a} \right) \left( \frac{d}{da} \frac{D_+}{a} \right) + \frac{1}{6} D_+^2 \left( \frac{d}{da} \frac{D_+^2}{a} \right)^2 & (q = 2) \\ \frac{1}{2} D_+ \left( \frac{d}{da} \frac{D_+^2}{a} \right)^2 \left( \frac{d}{da} \frac{D_+}{a} \right) + \frac{1}{2} D_+^2 \left( \frac{d}{da} \frac{D_+^2}{a} \right) \left( \frac{d}{da} \frac{D_+}{a} \right)^2 & (q = 3) \\ \left( \frac{d}{da} \frac{D_+^2}{a} \right)^2 \left( \frac{d}{da} \frac{D_+}{a} \right)^2 & (q = 4) \end{cases} \quad (6.23)$$

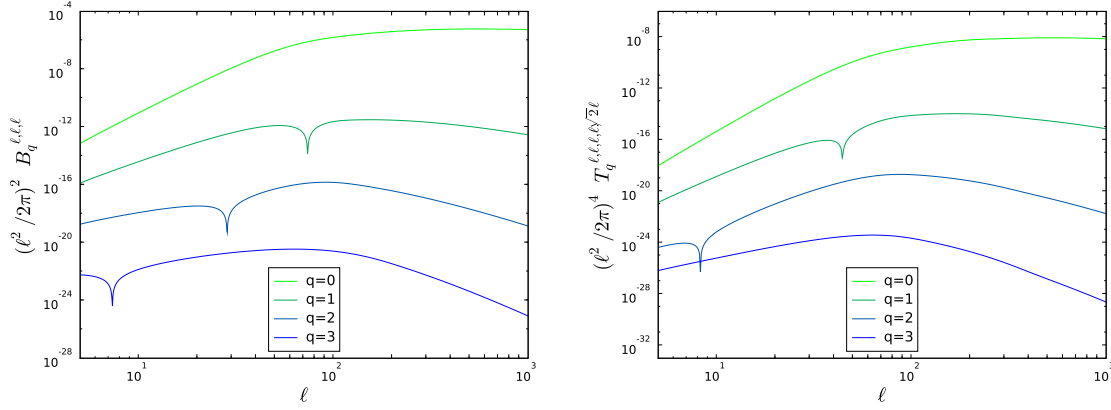


**Figure 6.4.:** *Left panel:* The absolute values of the mixed equilateral iSW-galaxy bispectra  $B_{i_1 i_2 i_3}^{\ell, \ell, \ell}$  as a function of angular scale  $\ell$  are depicted in this figure. The value  $q = i_1 + i_2 + i_3$  defines the mixture of the source fields. *Right panel:* The absolute values of the mixed square iSW-galaxy trispectra  $T_{i_1 i_2 i_3 i_4}^{\ell, \ell, \ell, \ell, \sqrt{2}\ell}$  as a function of angular scale  $\ell$  are shown in this plot. The value  $q = i_1 + i_2 + i_3 + i_4$  defines the mixture of the source fields.

and for the third order we obtain the following time evolution:

$$\mathcal{Q}_{q, \text{square}}^{(3)} = \begin{cases} D_+^6 & (q = 0) \\ \frac{1}{4} D_+^5 \left( \frac{d}{da} \frac{D_+}{a} \right) + \frac{3}{4} D_+^3 \left( \frac{d}{da} \frac{D_+^3}{a} \right) & (q = 1) \\ \frac{1}{2} D_+^4 \left( \frac{d}{da} \frac{D_+}{a} \right)^2 + \frac{1}{2} D_+^2 \left( \frac{d}{da} \frac{D_+^3}{a} \right) \left( \frac{d}{da} \frac{D_+}{a} \right) & (q = 2) \\ \frac{1}{4} D_+^3 \left( \frac{d}{da} \frac{D_+^2}{a} \right)^3 + \frac{3}{4} D_+ \left( \frac{d}{da} \frac{D_+^3}{a} \right) \left( \frac{d}{da} \frac{D_+}{a} \right)^2 & (q = 3) \\ \left( \frac{d}{da} \frac{D_+^3}{a} \right) \left( \frac{d}{da} \frac{D_+}{a} \right)^3 & (q = 4) \end{cases} . \quad (6.24)$$

Time evolutions for the different perturbative orders of the mixed trispectra are depicted in Fig. 6.3. One can see that for  $q = 1, 2$  they evolve identically but differ more strongly with increasing number  $q$  of included iSW fields.

The equilateral bispectra and square trispectra are depicted in Fig. 6.4. As in the power spectra one can observe also here the weakness of the iSW signal in comparison to the projected galaxy distribution field. This is clearly illustrated in the decrease of the polyspectra with increasing number  $q$  of included iSW source fields. Once more, the iSW effect shows its nature of being a large scale effect. With higher  $q$  the slope of the spectra increases in the large  $\ell$  region. The physical reason for this is the coupling of the iSW effect to the gravitational potential in contrast to the galaxy distribution, which couples directly to the density contrast. Mathematically, this fact manifests itself in the appearance of the  $1/k^2$  factors for the iSW contributions, originating from the inversion of the Poisson equation.

Since the linear iSW effect is strictly anti-correlated with respect to the galaxy density, linear cross-spectra would never show a change in sign in dependence on  $\ell$ . This does not apply for the non-linear iSW effect. The second order contributions have the opposite sign in their time evolution. It is therefore possible that for small  $\ell$  the linear effect dominates while for large  $\ell$  the non-linear effect determines the sign of the correlation. These changes in sign can now be observed in Fig. 6.4, for instance at  $\ell \approx 80$  in the bispectrum  $\langle \tau \gamma^2 \rangle$ . This behavior has also been observed and studied in the CMB-weak-lensing cross spectrum (Nishizawa et al., 2008).

$N$	$\Delta\Omega$	$f_{\text{sky}}$	$z_0$	$b$	$n$
$3.0 \times 10^9$	$2\pi$	0.5	0.64	1.0	$4.7 \times 10^8$

**Table 6.1.:** The Properties of the *Euclid* galaxy survey are listed in this table: total number  $N$  of objects, solid angle  $\Delta\Omega$  covered (in radians), sky fraction  $f_{\text{sky}}$ , redshift parameter  $z_0$ , galaxy bias  $b$  and density per unit steradian  $n$ .

## 6.4. Detectability

### 6.4.1. Sources of noise

The step from a good theoretical framework to an analysis of real data or to an estimation of the realistically accessible information content encompasses the description of all relevant effects influencing the measured data. Only then, one will be able to make statements about a physical process and the likelihood of its actual measurement. For the evaluation of the covariances of the bispectra and trispectra, the two-point function will be needed. In the same notation as the higher order spectra they are defined as

$$\langle \varphi_{i_1}(\ell_1) \varphi_{i_2}(\ell_2) \rangle = (2\pi)^2 \delta_{\text{D}}(\ell_1 + \ell_2) C_{i_1 i_2}^{\ell_1}. \quad (6.25)$$

In the case at hand the actual theoretically expected iSW signal in our fiducial cosmological model is superposed on the primary CMB fluctuations. Its relative amplitude reaches from 10% on very large scales to a negligible fraction of the signal for scales smaller than  $\ell \approx 200$ . Furthermore, the detected CMB signal is subjected to instrumental noise  $\sigma_\tau$  and a Gaussian beam  $\beta(\ell)$ .

Assuming that the noise sources of the galaxy counts are mutually uncorrelated, the pure galaxy-galaxy spectra are solely subjected to a Poissonian noise term  $1/\bar{n}$ . The cross-spectra between the two fields will be free of noise, since the noise sources of the single fields are uncorrelated. Now we can relate the measured spectra  $\tilde{C}_{i_1 i_2}^\ell$  to the theoretical spectra  $C_{i_1 i_2}^\ell$ :

$$\begin{aligned} \tilde{C}_{00}^\ell &= C_{00}^\ell + \frac{1}{\bar{n}} \\ \tilde{C}_{01}^\ell &= C_{01}^\ell \\ \tilde{C}_{11}^\ell &= C_{11}^\ell + C_{\text{CMB}}^\ell + \sigma_\tau^2 \beta^{-2}(\ell). \end{aligned} \quad (6.26)$$

The contributions in detail are:

(i) As the Fourier transform of the Gaussian beam one obtains  $\beta^{-2}(\ell) = \exp(\Delta\theta^2 \ell(\ell + 1))$ . We use  $\Delta\theta = 7.1$  arcmin, which corresponds to the  $\nu = 143$  GHz channels closest to the CMB emission maximum. For the conversion of  $w_T^{-1} = T_{\text{CMB}}^2 \sigma_\tau^2$  to the noise amplitude in the dimensionless temperature perturbation  $\tau$  with  $w_T = (0.01 \mu\text{K})^2$  (Zaldarriaga et al., 1997) we use the value  $T_{\text{CMB}} = 2.725$  K for the CMB temperature.

(ii) Furthermore, a CMB temperature power spectrum  $C_{\text{CMB}}^\ell$  was generated, which was equally scaled with the CMB temperature  $T_{\text{CMB}} = 2.725$  K, with the Code for Anisotropies in the Microwave Background (CAMB, Lewis et al., 2000) for the fiducial  $\Lambda$ CDM cosmology. The noise contribution from the CMB-spectrum  $C_{\text{CMB}}^\ell$  represents the main challenge in the observation of the iSW bispectra and trispectra. It provides high values for the covariance at low  $\ell$ , and it by far dominates for larger angular wave numbers,  $C_{\text{CMB}}^\ell \gg C_{00}^\ell$ . The orders of magnitude for the different contributions of the linear estimator  $\tilde{C}_{11}^\ell$  are depicted in Fig 6.5. One can see, that even at large angular wave numbers  $\ell$  the pure linear iSW signal  $C_{11}^\ell$  is still more than one order of magnitude weaker than the signal from primordial fluctuations  $C_{\text{CMB}}^\ell$ . We show the linear iSW signal  $C_{11}^\ell$ , since it is used for the derivation of the higher order correlators in our formalism.

(iii) The inverse number density  $n$  of objects per unit steradian determines the Poissonian noise term in the galaxy count. In Table 6.1 the properties of the main galaxy sample as it would be expected from *Euclid* are summarized. Major advantages lie in the large sky coverage and the high number of observed objects. Here, we assumed a non-evolving galaxy bias for simplicity.

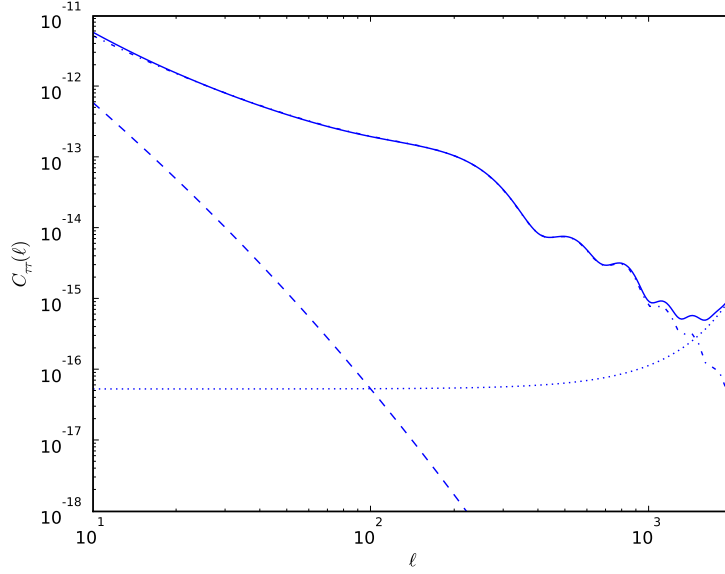


**Figure 6.5.:** Constituents of the measured angular CMB spectrum  $\tilde{C}_{11}^\ell$ . Depicted are the total signal  $\tilde{C}_{11}^\ell$  (solid line), the contribution from primordial fluctuations  $C_{\text{CMB}}^\ell$  (dash-dotted line), the linear iSW-effect  $C_{11}^\ell$  (dashed line) and the instrumental noise  $\sigma_\tau^2 \beta^{-2}(\ell)$  (dotted line), which is fortunately sub-dominant at the large scales of interest.

#### 6.4.2. Covariances

In the case of Gaussian noise the observed and estimated bispectra  $\tilde{B}_{i_1 i_2 i_3}^{\ell_1, \ell_2, \ell_3}$  and the trispectra  $\tilde{T}_{i_1 i_2 i_3 i_4}^{\ell_1, \ell_2, \ell_3, \ell_4}$  are unbiased estimates of the true bispectra  $B_{i_1 i_2 i_3}^{\ell_1, \ell_2, \ell_3}$  and trispectra  $T_{i_1 i_2 i_3 i_4}^{\ell_1, \ell_2, \ell_3, \ell_4}$  (Hu, 2001),

$$\begin{aligned} \tilde{B}_{i_1 i_2 i_3}^{\ell_1, \ell_2, \ell_3} &\simeq B_{i_1 i_2 i_3}^{\ell_1, \ell_2, \ell_3} \\ \tilde{T}_{i_1 i_2 i_3 i_4}^{\ell_1, \ell_2, \ell_3, \ell_4} &\simeq T_{i_1 i_2 i_3 i_4}^{\ell_1, \ell_2, \ell_3, \ell_4}. \end{aligned} \quad (6.27)$$

This is in contrast to the spectra  $C_{i_1 i_2}^\ell$ , which were discussed in the previous subsection. The covariances of the estimators of the bispectra and trispectra are defined as

$$\begin{aligned} \text{Cov} \left[ \tilde{B}_{i_1 i_2 i_3}^{\ell_1, \ell_2, \ell_3}, \tilde{B}_{i_1' i_2' i_3'}^{\ell_1', \ell_2', \ell_3'} \right] &= \left\langle \left( \tilde{B}_{i_1 i_2 i_3}^{\ell_1, \ell_2, \ell_3} - B_{i_1 i_2 i_3}^{\ell_1, \ell_2, \ell_3} \right) \left( \tilde{B}_{i_1' i_2' i_3'}^{\ell_1', \ell_2', \ell_3'} - B_{i_1' i_2' i_3'}^{\ell_1', \ell_2', \ell_3'} \right) \right\rangle, \\ \text{Cov} \left[ \tilde{T}_{i_1 i_2 i_3 i_4}^{\ell_1, \ell_2, \ell_3, \ell_4}, \tilde{T}_{i_1' i_2' i_3' i_4'}^{\ell_1', \ell_2', \ell_3', \ell_4'} \right] &= \left\langle \left( \tilde{T}_{i_1 i_2 i_3 i_4}^{\ell_1, \ell_2, \ell_3, \ell_4} - T_{i_1 i_2 i_3 i_4}^{\ell_1, \ell_2, \ell_3, \ell_4} \right) \left( \tilde{T}_{i_1' i_2' i_3' i_4'}^{\ell_1', \ell_2', \ell_3', \ell_4'} - T_{i_1' i_2' i_3' i_4'}^{\ell_1', \ell_2', \ell_3', \ell_4'} \right) \right\rangle. \end{aligned} \quad (6.28)$$

In a Gaussian approximation, which we are using here, any covariance can be expressed as a sum of products of two-point functions using Wick's theorem. While for pure covariances only the respective power spectra appear in this expansion, in our case of mixed covariances the products are formed from the estimators of the cross-correlation  $\tilde{C}_{01}^\ell$  and the two auto-correlations  $\tilde{C}_{00}^\ell$  and  $\tilde{C}_{11}^\ell$ .

In case of the bispectra with mutually different angular wave numbers  $\ell_{i_j} \neq \ell_{i_k}$  for  $j \neq k$  the covariance can be written as a sum over terms which are cubic in the spectra  $C_{i_1 i_2}^\ell$ ,

$$\text{Cov} \left[ \tilde{B}_{abc}^{\ell_1, \ell_2, \ell_3}, \tilde{B}_{a'b'c'}^{\ell_1', \ell_2', \ell_3'} \right] = \tilde{C}_{aa'}^{\ell_1} \tilde{C}_{bb'}^{\ell_2} \tilde{C}_{cc'}^{\ell_3} \delta_D(\ell_1 - \ell_1') \delta_D(\ell_2 - \ell_2') \delta_D(\ell_3 - \ell_3') + \text{perm}(\ell_1', \ell_2', \ell_3'). \quad (6.29)$$

On the subspace  $\ell_1, \ell_1' < \ell_2, \ell_2' < \ell_3, \ell_3'$  only the first term is non-vanishing. This block-diagonal matrix can now be inverted to

$$\text{Cov}^{-1} \left[ \tilde{B}_{abc}^{\ell_1, \ell_2, \ell_3}, \tilde{B}_{a'b'c'}^{\ell_1', \ell_2', \ell_3'} \right] = \frac{\tilde{C}_{aa'}^{*\ell_1} \tilde{C}_{bb'}^{*\ell_2} \tilde{C}_{cc'}^{*\ell_3}}{\det C^{\ell_1} \det C^{\ell_2} \det C^{\ell_3}} \delta_D(\ell_1 - \ell_1') \delta_D(\ell_2 - \ell_2') \delta_D(\ell_3 - \ell_3'), \quad (6.30)$$

with the adjoint matrix  $\tilde{C}_{aa'}^{*\ell}$ ,

$$\tilde{C}^{*\ell} = \begin{pmatrix} C_{11}^\ell & -C_{01}^\ell \\ -C_{01}^\ell & C_{00}^\ell \end{pmatrix}. \quad (6.31)$$

In analogy to the bispectrum case, the inverse covariance of the trispectra in the subspace  $\ell_1, \ell'_1 < \ell_2, \ell'_2 < \ell_3, \ell'_3 < \ell_4, \ell'_4$  amounts to

$$\text{Cov}^{-1} \left[ \tilde{T}_{abcd}^{\ell_1, \ell_2, \ell_3, \ell_4}, \tilde{T}_{a'b'c'd'}^{\ell'_1, \ell'_2, \ell'_3, \ell'_4} \right] = \frac{\tilde{C}_{aa'}^{*\ell_1} \tilde{C}_{bb'}^{*\ell_2} \tilde{C}_{cc'}^{*\ell_3} \tilde{C}_{dd'}^{*\ell_4}}{\det C^{\ell_1} \det C^{\ell_2} \det C^{\ell_3} \det C^{\ell_4}} \times \delta_D(\ell_1 - \ell'_1) \delta_D(\ell_2 - \ell'_2) \delta_D(\ell_3 - \ell'_3) \delta_D(\ell_4 - \ell'_4). \quad (6.32)$$

For an observation covering the sky with a fraction of  $f_{\text{sky}}$  the covariances scale like  $f_{\text{sky}}^{-1}$ . The anti-correlation in the cross-spectra  $C_{01}^\ell$  will not change the sign of the covariances, since in each of the products an even number of these mixed spectra appears.

### 6.4.3. Signal-to-noise ratios

The signal-to-noise ratio  $\Sigma^{(3)}$  for the simultaneous measurements of the all pure and mixed bispectra  $\langle \tau^q \gamma^{3-q} \rangle$  and  $\Sigma_q^{(4)}$  for the all mixed and pure trispectra  $\langle \tau^q \gamma^{4-q} \rangle$ , where all field indices are summed over, would imply a thorough derivation of all cross-correlations between different field mixtures. Here, we are rather interested in the individual signal-to-noise ratios of certain field configurations. If one reduces the data to a mixed configuration  $q$ , only the cases  $q = 0$  and  $q = 1$  provide a measurement in and above the order of magnitude of the noise level. For  $q = 0$  we obtain

$$\begin{aligned} (\Sigma_0^{(3)})^2 &= \frac{f_{\text{sky}}}{4\pi^3} \int d^2\ell_1 d^2\ell_2 \frac{(B_{000}^{\ell_1, \ell_2, \ell_3})^2}{6 \tilde{C}_{00}^{\ell_1} \tilde{C}_{00}^{\ell_2} \tilde{C}_{00}^{\ell_3}} \\ (\Sigma_0^{(4)})^2 &= \frac{f_{\text{sky}}}{8\pi^4} \int d^2\ell_1 d^2\ell_2 d^2\ell_3 \frac{(T_{0000}^{\ell_1, \ell_2, \ell_3, \ell_4})^2}{24 \tilde{C}_{00}^{\ell_1} \tilde{C}_{00}^{\ell_2} \tilde{C}_{00}^{\ell_3} \tilde{C}_{00}^{\ell_4}} \end{aligned} \quad (6.33)$$

However, since we are aiming for iSW detections, the more interesting case is  $q = 1$ . The signal-to-noise ratio splits up into two contributions,

$$\begin{aligned} (\Sigma_1^{(3)})^2 &= \frac{f_{\text{sky}}}{4\pi^3} \int d^2\ell_1 d^2\ell_2 \left( 2 \det C^{\ell_1} \det C^{\ell_2} \det C^{\ell_3} \right)^{-1} \\ &\quad \left[ (B_{001}^{\ell_1, \ell_2, \ell_3})^2 \tilde{C}_{11}^{\ell_1} \tilde{C}_{11}^{\ell_2} \tilde{C}_{00}^{\ell_3} + B_{001}^{\ell_1, \ell_2, \ell_3} \tilde{C}_{11}^{\ell_1} \tilde{C}_{01}^{\ell_2} \tilde{C}_{01}^{\ell_3} B_{010}^{\ell_1, \ell_2, \ell_3} \right] \\ (\Sigma_1^{(4)})^2 &= \frac{f_{\text{sky}}}{8\pi^4} \int d^2\ell_1 d^2\ell_2 d^2\ell_3 \left( \det C^{\ell_1} \dots \det C^{\ell_4} \right)^{-1} \\ &\quad \left[ \frac{1}{6} (T_{0001}^{\ell_1, \ell_2, \ell_3, \ell_4})^2 \tilde{C}_{11}^{\ell_1} \tilde{C}_{11}^{\ell_2} \tilde{C}_{11}^{\ell_3} \tilde{C}_{00}^{\ell_4} + \frac{1}{4} T_{0001}^{\ell_1, \ell_2, \ell_3, \ell_4} \tilde{C}_{11}^{\ell_1} \tilde{C}_{11}^{\ell_2} \tilde{C}_{01}^{\ell_3} \tilde{C}_{01}^{\ell_4} T_{0010}^{\ell_1, \ell_2, \ell_3, \ell_4} \right]. \end{aligned} \quad (6.34)$$

A detailed calculation of the signal-to noise expressions can be found in Section A.4. The inverse covariances of the polyspectra will always remain positive, since always an even number of anti-correlating cross-spectra will appear in its expression. However, the mixed field contributions can in general become negative.

The cumulative signal-to-noise ratios  $\Sigma_q^{(n)}$  for the mixed bispectra  $B_q$  and the mixed trispectra  $T_q$  are depicted in Fig. 6.6 for  $q = 0, 1, 2$ . The qualitative behavior of the cumulative signal-to-noise curves are again determined by the individual signal strengths of the two source fields  $\gamma$  and  $\tau$ . The strong fluctuation of the galaxy distribution  $\gamma$  even on small scales leads to a considerable increase of  $\Sigma$  for large  $\ell$  and small  $q$ . In contrast to this the iSW-effect is a large scale effect and therefore increases the slope in the small  $\ell$  range of the spectrum. It does not contribute significant signal

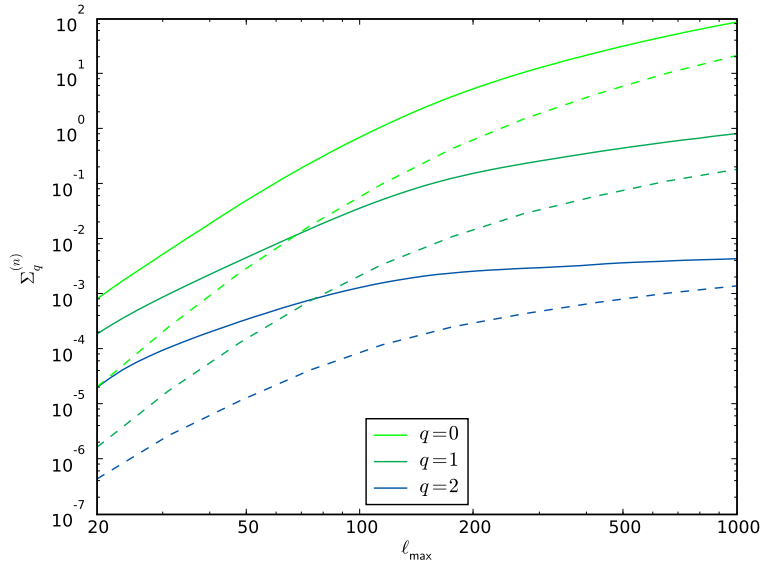


**Figure 6.6.:** Cumulative signal-to-noise ratios  $\Sigma_q^{(n)}$  for measurements of the bispectra  $\langle \tau^q \gamma^{3-q} \rangle$  (solid lines) and trispectra  $\langle \tau^q \gamma^{4-q} \rangle$  (dashed lines),  $q = 0, 1$ , for *Planck* CMB data in cross-correlation with *Euclid*-like survey, up to a resolution limit  $\ell_{\max} = 10^3$  starting from a minimum angular wave number of  $\ell_{\min} = 10$ .

$q$	0	1	2
$\Sigma_q^{(3)}$	87.8	0.828	$4.43 \cdot 10^{-3}$
$\Sigma_q^{(4)}$	21.7	0.19	$1.42 \cdot 10^{-3}$

**Table 6.2.:** Cumulative signal-to-noise ratios  $\Sigma_q^{(n)}$  for measurements of the bispectra  $\langle \tau^q \gamma^{3-q} \rangle$  and the trispectra  $\langle \tau^q \gamma^{4-q} \rangle$ ,  $q = 0, 1, 2$ , for *Planck* CMB data in cross-correlation with *Euclid*-like survey, up to a resolution limit  $\ell_{\max} = 10^3$  starting from a minimum angular wave number of  $\ell_{\min} = 10$ .

strength above values of  $\ell_{\max} > 300$ , for this reason the signal-to-noise curves flatten off in this region of the spectrum for  $q = 1, 2$ . The wider spread between different values of  $q$  for the trispectrum in contrast to the bispectrum is due to the higher power of source fields.

Quantitatively, higher values of  $q$  lead to a smaller significance in the signal. Included were contributions starting from large angular scales  $\ell_{\min} = 10$  up to smallest measurable scales in the *Planck* survey  $\ell_{\max} = 10^3$ . The pure galaxy polyspectra  $\langle \gamma^3 \rangle$  and  $\langle \gamma^4 \rangle$  can both be measured with a detection significance of  $\gg 3\sigma$ ,  $\Sigma_0^{(3)} = 87.8$  and  $\Sigma_0^{(4)} = 21.7$ . Including only one iSW source field reduces the signal down to the noise level. While the bispectrum  $\langle \tau \gamma^2 \rangle$  reaches a signal-to-noise ratio of  $\Sigma_1^{(3)} = 0.82$ , the value for the trispectrum  $\langle \tau \gamma^3 \rangle$  reaches a maximum of  $\Sigma_1^{(4)} = 0.19$ . Combining measurements of the  $q = 1$  bi- and trispectra would therefore be able to contribute a maximum signal-to-noise contribution of  $\Sigma \approx 0.84$ . Unfortunately, this is - taken on its own - still a very poor measurement significance. However, it could be used as an additional signal source to the strongest iSW signal from the cross-spectrum  $\langle \tau \gamma \rangle$ .

For the higher values of  $q$  only the case of two iSW source fields  $q = 2$  is plotted in Fig. 6.6. Both for the bispectrum as well as for the trispectra the signal-to-noise ratios is negligible with maximum values of  $\Sigma_2^{(3)} = 4.43 \cdot 10^{-3}$  and  $\Sigma_2^{(4)} = 1.42 \cdot 10^{-3}$  respectively.

One can obtain a grasp of the differential contributions of the signal-to-noise ratios with respect to

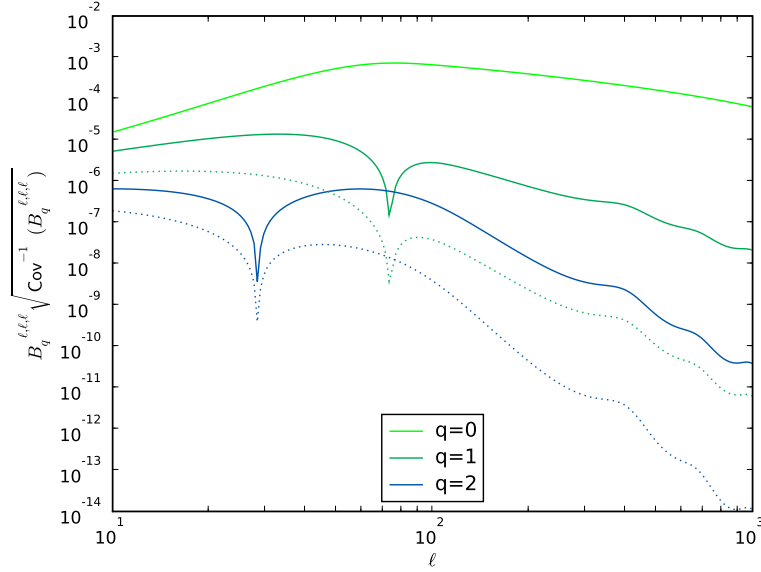


**Figure 6.7.:** The differential contributions of the equilateral bispectra to the signal-to-noise ratios in dependence on angular wave number  $\ell$  are depicted here for different source field mixtures  $q = 0, 1, 2$  (solid lines). For  $q = 1, 2$  the contributions from cross-correlations are also shown (dotted lines), as they appear for  $q = 1$  in the second term of the second line in eqn. (6.34). One can observe the increasing amplitude of the baryonic acoustic oscillations for larger  $q$ . Also the change in sign can be studied due to the transition from linear dominated to non-linear dominated scales.

angular wave number  $\ell$ , if one studies the quantity

$$\begin{aligned} \left( \frac{d}{d\ell} \Sigma_{q,\text{equi}}^{(3)} \right)^{\frac{1}{2}} &\propto B_q^{\ell,\ell,\ell} \sqrt{\text{Cov}^{-1}(B_q^{\ell,\ell,\ell})} \\ \left( \frac{d}{d\ell} \Sigma_{q,\text{square}}^{(4)} \right)^{\frac{1}{2}} &\propto T_q^{\ell,\ell,\ell,\ell, \sqrt{2}\ell} \sqrt{\text{Cov}^{-1}(T_q^{\ell,\ell,\ell,\ell, \sqrt{2}\ell})}, \end{aligned} \quad (6.35)$$

where derivative is taken with respect to the absolute value  $\ell$  of the flat sky wave number  $\ell$ , which should not be mistaken for a discrete multipole order. In Fig. 6.7 these differential contributions of equilateral bispectra are depicted in dependence on  $\ell$  for different source field mixtures  $q$ . The differential contributions of the square trispectra behave qualitatively analogous. Also the change in sign can be studied due to the transition from linear dominated to non-linear dominated scales. For  $q = 1, 2$  the contributions from cross-correlations are also shown (dotted lines), as they appear for  $q = 1$  in the second term of the second line in eqn. (6.34). As one can see, these terms are sub-dominant and can be neglected in our case.

One can observe the increasing amplitude of the baryonic acoustic oscillations for larger  $q$ , which originate from  $C_{\text{CMB}}^\ell$ . The falling slopes of the BAO features in the covariance lead to small plateaus in the differential contributions for larger  $\ell$ . Since in these regions the signal decreases more gently than the covariance, one obtains a local increase of signal-to-noise. However, this effect can hardly be observed in Fig. 6.6.

## 6.5. Summary

The objective of this chapter has been a study of the detectability of non-Gaussian signatures in non-linear iSW-effect. Besides the mixed bispectra of the form  $\langle \tau^q \gamma^{3-q} \rangle$ ,  $q = 0, 1, 2$ , between the galaxy

distribution  $\gamma$  and the iSW temperature perturbation  $\tau$  we also calculate for the first time the mixed trispectra of the analogous form  $\langle \tau^q \gamma^{4-q} \rangle$ . Both types of spectra were consistently derived in tree-level perturbation theory. This implies for the bispectra perturbative corrections to second order and for the mixed trispectra contributions from second and third order terms. Furthermore, we investigated the time evolution of these individual 3d-source terms, which are in general very diverse. For this reason, the time evolution and the configuration dependence of a specific class of spectra, equilateral bispectra and the square trispectra, were studied. Finally, the achievable signal-to-noise ratios were derived for measurements cross-correlating data from *Planck* and a *Euclid*-like galaxy sample. (i) The linear iSW-effect has the time dependence  $d(D_+/a)/da$ , which makes it sensitive to dark energy but makes it vanish in  $\Lambda$ CDM-models with  $\Omega_m \equiv 1$  and  $D_+(a) = a$ . In contrast to this, the non-linear contributions to the iSW signal are sensitive to derivatives of higher powers of  $D_+(a)$ , namely  $d(D_+^2/a)/da$  for second order perturbation theory and  $d(D_+^3/a)/da$  for third order contributions. For this reason, the effect does not vanish in matter-dominated epochs.

(ii) The covariances of the measurements were derived in a Gaussian approximation. For the CMB observation the intrinsic CMB fluctuations and instrumental noise in form of the pixel noise and a Gaussian beam were considered as noise sources. A Poissonian noise term was added to the galaxy distribution signal. For simplicity the fluctuations of the dark matter density and galaxy number density were related to each other by a constant linear biasing model.

(iii) In the mixed bispectra and trispectra the configuration and scale dependence represent the different correlation lengths of the gravitational potential and the density field. Since the specific perturbative corrections dominate on different scales, the mixed spectra change their sign at certain values of  $\ell$ . In case of the bispectra one can observe the transition from linear domination to non-linear domination move to larger and larger scales with increasing number  $q$  of included iSW source fields.

(iv) We derived the cumulative signal-to-noise ratios  $\Sigma_q^{(3)}$  for the measurements of mixed bispectra  $\langle \tau^q \gamma^{3-q} \rangle$ , and  $\Sigma_q^{(4)}$  for the mixed trispectra  $\langle \tau^q \gamma^{4-q} \rangle$ , with a Gaussian approximation to the covariance. The integrations were performed numerically using Monte Carlo integration techniques from the multi-dimensional numerical integration library CUBA (Hahn 2005). For both spectra the initial CMB fluctuations are the most important noise source, which makes it difficult to observe the signals. We assumed a cross-correlation of *Planck* data with a *Euclid*-like galaxy sample starting from angular scales of  $\ell_{\min} = 10$  up to a resolution of  $\ell_{\max} = 10^3$ . The only spectra reaching the order of magnitude of the noise level are the bispectra and trispectra in the configuration  $\langle \tau \gamma^{n-1} \rangle$ . We found the numerical signal-to-noise ratios of  $\Sigma_1^{(3)} = 0.828$  for the bispectrum and  $\Sigma_1^{(4)} = 0.19$  for the trispectrum and conclude, that non-Gaussian signatures of the iSW-effect are too weak to be detected. At the same time, these small signal-to-noise ratios suggest that non-Gaussianities in the CMB generated by the iSW-effect are small enough so that they do not interfere with the estimation of the inflationary non-Gaussianity parameter  $f_{\text{NL}}$  from the bispectrum  $\langle \tau^3 \rangle$  and of the two parameters  $g_{\text{NL}}$  and  $\tau_{\text{NL}}$  from the trispectrum  $\langle \tau^4 \rangle$ .

# Summary and conclusions

In the first part of our thesis we focused on an extension of the time renormalization group (TRG) approach introduced by Pietroni (2008) for describing non-linear cosmic structure formation. First, we implemented the original approach for  $\Lambda$ CDM and SCDM type cosmological models with possible modifications to all different types of dark energy constituents with a constant equation of state parameter. While first semi-analytical results of the method had been truncated at the level of the bispectrum, we modified the original method to a hybrid approach using tree-level perturbation theory for the description of the trispectrum. To isolate the impact of this extension on the power spectrum results and to consistently compare our results to numerical simulations (Carlson et al., 2009), we restricted ourselves to Gaussian initial growing mode conditions. We also extended the diagrammatic language for the power spectrum corrections with respect to the additional terms. Furthermore, we analytically discussed the possible inclusion of the full trispectrum with the next higher evolution equation and argued the numerical effort to be unreasonable.

The crucial point in the implementation of the original method is the numerical evaluation of the loop integrals. Due to isotropy the one-loop integrals could be reduced to a 2d-integral which can still be integrated at sufficient speed by trapezoidal routines. The trispectrum correction integrals are of two loop order. In this case, only one angular integration is trivial and one has to solve a 5d-integral. For their evaluation we chose Monte Carlo integration techniques from the multidimensional numerical integration library CUBA (Hahn, 2005). With traditional trapezoidal algorithms the processing time would have exploded beyond weeks and one of the key advantages of the method with respect to numerical simulations would have been vitiated.

Analytically, the non-linear correction term in the bispectrum evolution equation is of two-loop order. It couples the full four-point function to the vertex function by a double integration. If one truncates at the level of the trispectrum, the remaining term is disconnected and one integration becomes trivial. If the connected part of the four-point function is taken into account this is no longer the case and one is left with two non-trivial integrations. With the tree-level approximation, we chose the next easiest way to take the trispectrum into account for a practical reason. Due to its simple time evolution, which is given in powers of the growth function only, it is sufficient to evaluate the respective corrections at one particular time. The solution process of the original approach remains unchanged up to the additional connected correction terms in the bispectrum evolution function.

One of the major advantages of analytical and semi-analytical methods over numerical simulations is the possibility to interpret correction terms, which gives rise to a deeper understanding of the processes at hand. This can for instance be achieved by a diagrammatic description of the correction terms, which were extended by the additional perturbative 2-loop contributions. However, the extension should not be interpreted as being of perturbative nature only, since the tree-level terms also drive the non-perturbative evolution.

The numerical results of our extended method show an improvement in the power spectrum prediction with respect to the original method for  $k < 0.25 \text{ h/Mpc}^{-1}$  at redshift  $z = 1$  and for  $k < 0.18 \text{ h/Mpc}^{-1}$  at redshift  $z = 0$ . On smaller scales the original method performs better than the method with the trispectrum included.

Summing up the results of the extended model, it has emphasized the importance of the trispectrum for the evolution of the lower order correlators even starting from Gaussian initial conditions. Most certainly it will play an even larger role once initial non-Gaussianities are taken into account. The improvement of results at the onset of the non-linear regime is significant. It also performs better throughout the entire region, in which both methods reach approximately per cent accuracy. The scale

at which the method falls behind the original approach may also be taken as a measure for the break down of the trispectrum's tree-level description. The drawback however is the numerical cost, the extension with respect to the trispectrum comes with. Depending on the resolution in  $k$ -space the evaluation of the trispectrum correction terms may take up to several ours on a ten core machine. This illustrates that the method is not ready for a scan through a larger range of cosmological models.

For the underlying time renormalization technique our results show that even a small step towards the inclusion of important higher order correlators increases the numerical cost significantly. Taking the full trispectrum evolution into account would be the next logical step after our approach and would imply the truncation at the level of the connected five-point function. We argued that this would be unreasonable from a numerical point of view, since then several fields in 3d-Fourier space would have to be propagated in time in the numerical algorithm. For each of the sampling points one would need to evaluate a 2-loop integral. For this reason, we conclude that the capability of the time renormalization group approach is tightly limited with respect to predictions of the power spectrum further into the non-linear regime.

However, fortunate results came up after the publication of our method. A non-linear power spectrum from resummed perturbation theory was found and was successfully implemented in a fast algorithm (Anselmi & Pietroni, 2012). Based on earlier work using generating functionals to renormalize the non-linear propagator in the large  $k$  limit (Matarrese & Pietroni, 2007; Anselmi et al., 2011b) it was now possible to predict the power spectrum itself to per cent accuracy deeper into the BAO region, up to  $k \sim 1 h \text{Mpc}^{-1}$ . This approach will open new possibilities for a broader range of applications such as weak lensing. However, one major future challenge will be to find accurate predictions for the power spectrum scales for a larger set of different cosmologies. Early resumming techniques applied to cosmological structure formation (Crocco & Scoccimarro, 2006a,b) were limited by the approximation  $f_+ = \Omega_m^{1/2}$ , which restricts the applicability to  $\Lambda$ CDM-like cosmologies. The same applies to the recent renormalization of the power spectrum (Anselmi & Pietroni, 2012). The capability of also accounting for more exotic cosmological models (Anselmi et al., 2011a) can still be regarded as one of the major advantages of the time renormalization group approach. This, however, was diminished by including the tree-level perturbative trispectrum for which also the approximation  $f_+ = \Omega_m^{1/2}$  had to be assumed. For this reason, broadening the applicability of the models should be regarded as an interesting and important direction for future studies.

The second part of the thesis was of methodological kind. The subjects of interest were the linear and non-linear iSW effects. Considering a *Euclid*-like galaxy survey, we increased the signal-to-noise ratio by 15% for  $w = -0.9$  (10% for  $w = -1$ ) for cross-correlation measurements between the linear iSW effect and the tracer galaxy density field with a line-of-sight tomographical technique in the galaxy field. For this purpose we used polynomial weighting functions which were orthogonalized with help of the Gram-Schmidt orthogonalization algorithm. This choice of basis system for the covariance matrix leads to statistical independent signal contributions in the galaxy auto-correlation. The Fisher matrix analysis and the marginalized errors on cosmological parameters inferred from it show an inverse square-root behavior which indicates the statistical independence of the covariance's signal part. To investigate further possibilities of measuring the non-linear iSW effect we studied the qualitative behavior of cross-bispectra and cross-trispectra in the flat sky approximation. Unfortunately, even the combined signal of bispectra and trispectra does not exceed the noise level.

Naturally, the choice of polynomials as orthogonal basis system is not obvious. In general every complete basis system would be applicable for our purpose but polynomials give an easy to handle tool to test the idea of diagonalizing the signal part of the covariance. In general, it would be interesting to determine the best performing basis system - leading to the highest signal-to-noise ratio at the smallest number of included tomographical basis functions. However, the question may be asked whether it is worth the effort considering the relatively small signal-to-noise improvement of about 10%. For the cross-correlation alone a tomographical analysis does not pay off but in combination with a tomographical approach for the tracer galaxy density field itself it should be considered as a

rounding off for the analysis.

Our method was found to be numerically limited. This was mainly due to the Gram-Schmidt orthogonalization method which was used for the construction of the polynomial weighting function basis system. The scalar product evaluations cumulatively increase the numerical error with increasing order. The off-diagonal element in the orthogonality relation reached the percent level between the 9<sup>th</sup> order polynomial and the 10<sup>th</sup> order polynomial. For this reason, the analysis was truncated at the level of the 8<sup>th</sup> order polynomial. While this is inconvenient for the analysis, our results have shown that the conditional error are close to saturation at the achieved polynomial order. Thus, pushing the method to higher polynomial orders should not be regarded as our first priority.

One should keep in mind that the construction of the tomographical polynomials are not model independent. A fiducial model has to be chosen in the definition of the scalar product. This inevitably implies the analysis and the cosmological parameters to be exposed to a possible estimation bias. However, for the same tomographical approach in the neighbored field of weak gravitational lensing this possibility has been thoroughly discussed for various cases of bias and the effects were found to be small in comparison to the statistical errors (Schäfer & Heisenberg, 2011). Even in case of new upcoming biases which have not yet been accounted for it is still possible to minimize the effect via iteration between cosmological parameter estimation and the construction of orthogonal polynomials.

Also other approaches have been developed which aim at inferring line-of-sight information from the iSW effect with help of tomographical techniques. One drawback of our approach can be seen as the detour of tomography via the tracer galaxy density field. In an interesting alternative work, it was pointed out that the parameter estimates referred from standard statistical approaches can be biased by local variance (Frommert et al., 2008), which can be as large as 11% of the statistical errors. In the case of living in an unlikely realization of the universe parameter estimations could be strongly biased. They pointed out that once the large scale structure (LSS) is known, a theoretical prediction for the expected iSW effect could be referred from the LSS and correlated with the CMB signal. The estimated increase of 7% in signal-to-noise only applies once an ideal measurement of the large scale structure is given. The inversion of the Poisson equation, which is needed for the prediction of the gravitational potential, should give rise to additional errors. However, in contrast to the aforementioned method our tomographic approach is not prior-less and can possibly be subjected to small systematic errors.

Summing up, in combination with a tomographical analysis of the galaxy field itself, it is certainly worth to include also the cross-spectra into the tomographical method following our approach. Taken on its own the increase in signal-to-noise ratio does not justify the numerical effort. Furthermore, it should be considered as an alternative if the evaluation of the signal cross-correlation in standard  $z$ -binning is cumbersome. Due to its model dependence, systematical errors can not totally be excluded.

Our motivation to study higher order cross-correlators between the iSW effect and the tracer galaxy density field originated from the fact that up to this time the statistical form of the non-linear iSW effect was found to be below the detection limit (Martinez-Gonzalez et al., 1994; Sanz et al., 1996; Seljak, 1996b; Schäfer & Bartelmann, 2006). The different time evolutions of the fields and their respective perturbative corrections lead naturally to a large diversity in the time evolution of the perturbative contributions of the higher order correlators - the bispectra and trispectra. The more interesting it is, that we found a clear dependence of the transition scale between linear and non-linear effect on the field configuration. This was clearly seen in the simple case of the bispectra where the number enhancement of included iSW fields pushes the transition scale to larger scales. Also a clear decrease of the signal-to-noise ratio with increasing order of the correlator was observed. The study of even higher correlators is therefore not likely to contribute much to the signal strength. As a final result, we found the non-linear iSW effect not to be detectable with cross-correlation analysis of contemporary and upcoming galaxy surveys - in neither cross-correlation of any order up to the trispectra. It is more likely that the study of particular extreme over-densities or voids will open the possibility to detect the iSW effect as it was proposed by Granett et al. (2008). It was possible to reach a total signal-to-noise

ratio of  $\sim 4$  by stacking regions with superclusters and supervoids. This connection of the effect to real observed structures may also open new opportunities for detecting the non-linear iSW effect.

# A

## Analytical details

### A.1. Wick's theorem

In quantum field theory the Wick theorem is a fundamental tool for the derivation of propagators. In such argumentations - as for example in the context of path integrals and generating functionals - the theorem arises naturally as a result of the formalism which is applied (Maggiore, 2006). However, without being involved in the context and notation of quantum field theory some readers may find it difficult to understand the fundamental simple ideas of the theorem in a quantum field theory text book. For this reason we decided to present a simple proof of the theorem valid for any Gaussian random field with zero mean in Section A.1.1 motivating the definitions of connected correlators for non-Gaussian fields in Section A.1.2. The definition of connected part is also often referred to as the Wick theorem for non-Gaussian fields.

#### A.1.1. Gaussian case

We show here the Wick theorem in the Gaussian density field with zero mean  $\langle \delta_{\mathbf{x}} \rangle = 0$ . Starting point of the argumentation is writing the  $n$ -point function  $\langle \delta_{\mathbf{x}_1} \dots \delta_{\mathbf{x}_n} \rangle$  of the density field with an artificial source term  $z_i \delta_{x_i}$  in the probability density, which is set to zero in the end,

$$\begin{aligned} \langle \delta_{\mathbf{x}_1} \dots \delta_{\mathbf{x}_m} \rangle &= \frac{1}{\mathcal{N}} \int d\delta_{\mathbf{x}_1} \dots d\delta_{\mathbf{x}_m} \delta_{\mathbf{x}_1} \dots \delta_{\mathbf{x}_m} \exp\left(-\frac{1}{2} \delta_{x_i} (Q^{-1})_{ij} \delta_{x_j}\right) \\ &= \frac{1}{\mathcal{N}} \int d\delta_{\mathbf{x}_1} \dots d\delta_{\mathbf{x}_m} \delta_{\mathbf{x}_1} \dots \delta_{\mathbf{x}_m} \exp\left(-\frac{1}{2} \delta_{x_i} (Q^{-1})_{ij} \delta_{x_j} + z_i \delta_{x_i}\right) \Big|_{z_i=0}, \end{aligned} \quad (\text{A.1})$$

where  $\mathcal{N} = (2\pi)^{m/2} (\det Q)^{1/2}$  and the covariance matrix  $Q_{ij}$  is defined as

$$Q = \begin{pmatrix} \langle \delta_{\mathbf{x}_1} \delta_{\mathbf{x}_1} \rangle & \dots & \langle \delta_{\mathbf{x}_m} \delta_{\mathbf{x}_1} \rangle \\ \vdots & \ddots & \vdots \\ \langle \delta_{\mathbf{x}_1} \delta_{\mathbf{x}_m} \rangle & \dots & \langle \delta_{\mathbf{x}_m} \delta_{\mathbf{x}_m} \rangle \end{pmatrix}. \quad (\text{A.2})$$

Since the sources  $z_i$  are set to zero in the end, they do not alter the result. Their introduction can therefore be seen as a mathematical tool to write the correlators of  $\delta_{\mathbf{x}_i}$  as partial derivatives with respect to the sources  $z_i$ ,

$$\begin{aligned} \langle \delta_{\mathbf{x}_1} \dots \delta_{\mathbf{x}_m} \rangle &= \frac{\partial_{z_1} \dots \partial_{z_m}}{\mathcal{N}} \int d\delta_{\mathbf{x}_1} \dots d\delta_{\mathbf{x}_m} \exp\left(-\frac{1}{2} \delta_{x_i} (Q^{-1})_{ij} \delta_{x_j} + z_i \delta_{x_i}\right) \Big|_{z_i=0} \\ &= \partial_{z_1} \dots \partial_{z_m} \exp\left(\frac{1}{2} z_i Q_{ij} z_j\right) \Big|_{z_i=0}. \end{aligned} \quad (\text{A.3})$$

If  $n$  is uneven, the correlator vanishes, since in all summands will remain a factor  $z_i$ , which is set to zero in the end. In the case of an even  $n$  a sum over all combinations of products of  $n/2$  two-point correlators is formed,

$$\langle \delta_{x_1} \dots \delta_{x_m} \rangle = \langle \delta_{x_1} \delta_{x_2} \rangle \dots \langle \delta_{x_{n-1}} \delta_{x_n} \rangle + \text{all pair combinations} \in \{1 \dots n\} \quad (\text{A.4})$$

The lowest non-vanishing Gaussian  $n$ -point correlator for  $n > 2$  is the four-point correlator and can now be written as

$$\langle \delta_{x_1} \delta_{x_2} \delta_{x_3} \delta_{x_4} \rangle = \langle \delta_{x_1} \delta_{x_2} \rangle \langle \delta_{x_3} \delta_{x_4} \rangle + \langle \delta_{x_1} \delta_{x_3} \rangle \langle \delta_{x_2} \delta_{x_4} \rangle + \langle \delta_{x_1} \delta_{x_4} \rangle \langle \delta_{x_2} \delta_{x_3} \rangle. \quad (\text{A.5})$$

### A.1.2. Connected correlators

Motivated by the Wick theorem in the Gaussian case in eqn. (A.4) one can now motivate the non-Gaussian or connected parts of higher order correlators for general random fields in the following way (Bernardeau et al., 2002),

$$\begin{aligned} \xi^{(N)}(\mathbf{x}_1 \dots \mathbf{x}_N) &\equiv \langle \delta_{\mathbf{x}_1} \dots \delta_{\mathbf{x}_N} \rangle_c \\ &= \langle \delta_{\mathbf{x}_1} \dots \delta_{\mathbf{x}_N} \rangle \\ &\quad - \sum_{S \in \mathcal{P}(\{\mathbf{x}_1, \dots, \mathbf{x}_N\})} \prod_{s_i \in S} \xi^{(\#s_i)}(\mathbf{x}_{s_i(1)} \dots \mathbf{x}_{s_i(\#s_i)}). \end{aligned} \quad (\text{A.6})$$

Here, the sum is taken over all proper partitions of  $\{\mathbf{x}_1, \dots, \mathbf{x}_N\}$ .  $s_i$  denotes a subset of  $\{\mathbf{x}_1, \dots, \mathbf{x}_N\}$ , which is contained in the partition  $\mathcal{S}$ . The number of elements in the subset  $s_i$  are indicated by  $\#s_i$ . As we are dealing with random fields with zero mean throughout the entire thesis, no singlet terms contribute, i.e.  $\#s_i \geq 2$ . This simplifies calculations considerably since it reduces the number of proper partitions. One can see with help of eqn. (A.4), that for Gaussian fields with zero mean the definition in eqn. (A.6) implies the connected correlators to vanish.

## A.2. Compact structure formation equations

In the compact formulation of structure formation - introduced for flat matter dominated universes in Section 2.8 and later extended to flat cosmologies with a non-clustering dark energy component with constant equation of state in Section 3.2.1 - some technical details were skipped for conceptual clarity. However, they should be explained at this point.

Starting from the Fourier representation of the structure formation equation in eqn. (2.45),

$$\begin{aligned} \frac{\partial}{\partial \tau} \delta(\mathbf{k}) + \theta(\mathbf{k}) &= -\delta_D(\mathbf{k} - \mathbf{k}_1 - \mathbf{k}_2) \alpha(\mathbf{k}_1, \mathbf{k}_2) \delta(\mathbf{k}_1) \theta(\mathbf{k}_2) \\ \frac{\partial}{\partial \tau} \theta(\mathbf{k}) + \mathcal{H} \theta(\mathbf{k}) + \frac{3}{2} \mathcal{H}^2 \Omega_m \theta(\mathbf{k}) &= -\delta_D(\mathbf{k} - \mathbf{k}_1 - \mathbf{k}_2) \beta(\mathbf{k}_1, \mathbf{k}_2) \theta(\mathbf{k}_1) \theta(\mathbf{k}_2), \end{aligned} \quad (\text{A.7})$$

we first would like to transform the equations to a logarithmic time variable  $\eta$ ,

$$\eta = \log \left( \frac{D_+(a)}{D_+(a_{\text{in}})} \right). \quad (\text{A.8})$$

With  $\partial a / \partial \tau = a \mathcal{H}$  and  $\partial \eta / \partial a = f_+ / a$  one can write

$$\begin{aligned} \frac{\partial}{\partial \tau} &= \frac{\partial a}{\partial \tau} \frac{\partial \tau}{\partial a} \frac{\partial}{\partial \eta} \\ &= \mathcal{H} f_+ \frac{\partial}{\partial \eta}, \end{aligned} \quad (\text{A.9})$$

where  $f_+$  is defined as the slope of the growth function,

$$f_+ = \frac{d \log D_+}{d \log a}. \quad (\text{A.10})$$

Substituting now the doublet field

$$\begin{pmatrix} \delta(\mathbf{k}) \\ \theta(\mathbf{k}) \end{pmatrix} = e^\eta \begin{pmatrix} \varphi_1(\mathbf{k}) \\ -\mathcal{H} f_+ \varphi_2(\mathbf{k}) \end{pmatrix}, \quad (\text{A.11})$$

the evolution equations transform to

$$\begin{aligned} \frac{\partial}{\partial \eta} \varphi_1(\mathbf{k}) + \varphi_1(\mathbf{k}) - \varphi_2(\mathbf{k}) &= -\delta_D(\mathbf{k} - \mathbf{k}_{12}) \alpha(\mathbf{k}_1, \mathbf{k}_2) \delta(\mathbf{k}_1) \theta(\mathbf{k}_2) \\ \frac{\partial}{\partial \eta} \varphi_2(\mathbf{k}) - \frac{3}{2} \frac{\Omega_m}{f_+^2} \varphi_1(\mathbf{k}) + \left( \frac{\partial(\log \mathcal{H} + \log f_+)}{\partial \eta} + \frac{f_+ + 1}{f_+} \right) \varphi_2(\mathbf{k}) &= -\delta_D(\mathbf{k} - \mathbf{k}_{12}) \beta(\mathbf{k}_1, \mathbf{k}_2) \theta(\mathbf{k}_1) \theta(\mathbf{k}_2), \end{aligned}$$

Obviously, the term in the brackets in the second equation is the most problematic one, which we define as  $\Omega_{22}$ ,

$$\Omega_{22} \equiv \left( \frac{\partial(\log \mathcal{H} + \log f_+)}{\partial \eta} + \frac{f_+ + 1}{f_+} \right). \quad (\text{A.12})$$

Now, in the case of only dark matter and an additional non-clustering dark matter fluid with constant equation of state, one can find an integral solution for the growth function  $D_+(a)$ ,

$$D_+(a) = H(a) \int_0^a \frac{d\tilde{a}'}{\tilde{a}'^3 H^3(\tilde{a}')}. \quad (\text{A.13})$$

Using this we can rewrite  $\Omega_{22}$  as

$$\Omega_{22} \equiv \frac{\partial(\log \mathcal{H} + \log f_+)}{\partial \eta} + \frac{f_+ + 1}{f_+} = \frac{1}{f_+} \left( 3a \frac{H'}{H} + \left( \frac{a}{H} \right)^2 H'^2 + \frac{a^2}{H} H'' \right). \quad (\text{A.14})$$

Now, using Friedman's first equation for  $\Lambda$ CDM,

$$H^2(a) = H_0^2 \left( \Omega_{m0} a^{-3} + (1 - \Omega_{m0}) \right), \quad (\text{A.15})$$

we can write eqn. (A.14) as

$$\Omega_{22} = \frac{3}{2 f_+^2} \frac{1}{\left( 1 + \frac{\Omega_{\Lambda 0}}{\Omega_{m0}} a^3 \right)} = \frac{3}{2} \frac{\Omega_m}{f_+^2}. \quad (\text{A.16})$$

With this at hand, we can now write the eqs. (A.7) in the desired compact form,

$$\partial_\eta \varphi_a(\mathbf{k}) = \Omega_{ab} \varphi_b(\mathbf{k}) + e^\eta \tilde{\gamma}_{abc}(\mathbf{k}, -\mathbf{q}, -\mathbf{p}) \varphi_b(\mathbf{q}) \varphi_c(\mathbf{p}), \quad (\text{A.17})$$

with the linear evolution matrix

$$\Omega_{ab} = \begin{pmatrix} 1 & -1 \\ -\frac{3}{2} \frac{\Omega_m}{f_+^2} & \frac{3}{2} \frac{\Omega_m}{f_+^2} \end{pmatrix} \quad (\text{A.18})$$

and the non-linear interaction vertex  $\tilde{\gamma}_{abc}(\mathbf{k}, \mathbf{q}, \mathbf{p})$  with the only non-vanishing components

$$\begin{aligned} \tilde{\gamma}_{121}(\mathbf{k}, \mathbf{q}, \mathbf{p}) = \tilde{\gamma}_{112}(\mathbf{k}, \mathbf{p}, \mathbf{q}) &= \frac{1}{2} \delta_D(\mathbf{k} + \mathbf{q} + \mathbf{p}) \alpha(\mathbf{q}, \mathbf{p}), \\ \tilde{\gamma}_{222}(\mathbf{k}, \mathbf{q}, \mathbf{p}) &= \delta_D(\mathbf{k} + \mathbf{q} + \mathbf{p}) \beta(\mathbf{q}, \mathbf{p}). \end{aligned} \quad (\text{A.19})$$

In absence of dark energy, i.e.  $\Omega_m = 1$  and  $f_+ = 1$ , equation (A.18) reduces to the case in eqn. (2.58),

$$\Omega_{ab} = \begin{pmatrix} 1 & -1 \\ -3/2 & 3/2 \end{pmatrix}. \quad (\text{A.20})$$

### A.3. Derivation of the iSW-effect in general relativity

Since the integrated Sachs-Wolfe effect is known to be a large scale effect, on which gravitational perturbations are very small, one can safely employ a weak field approximation for the theoretical description. In principle, the fundamental idea of the iSW-effect can be understood in Newtonian gravity. For a more formal derivation we choose here the framework of general relativity following the derivation presented in [Durrer \(2008\)](#).

We assume a weak perturbation by the potential  $\Phi$  on a static, flat background. Anisotropic stress is neglected in this approach [Mukhanov \(2005\)](#). The metric can now be assumed to be nearly Minkowskian  $\eta_{\mu\nu}$  with only a small additional perturbative metric tensor  $h_{\mu\nu}$ .

$$g_{\mu\nu} = \eta_{\mu\nu} + h_{\mu\nu}. \quad (\text{A.21})$$

In this case, the infinitesimal length element can be written as ([Linder, 1997](#))

$$ds^2 = (\eta_{\mu\nu} + h_{\mu\nu}) dx^\mu dx^\nu = - \left(1 + \frac{2\Phi}{c^2}\right) d\eta^2 + \left(1 - \frac{2\Phi}{c^2}\right) d\mathbf{x}^2. \quad (\text{A.22})$$

The equations of motion for photons are the null-geodesics. The photon's four-momentum  $(n^0, \mathbf{n})$ , which is tangential to its trajectory  $x_\mu(\lambda)$  has to obey  $n^2 = 0$ . It is convenient to normalize the four momentum to  $n^0 = 1$  and  $\mathbf{n}^2 = 1$ . It is sufficient to consider a static background because of the conformal invariance of light-like geodesics, which do not change under a transformation of the type  $g_{\mu\nu} \rightarrow a^2 g_{\mu\nu}$  of the spatial part of the metric  $g_{\mu\nu}$ .

The geodesic equation now reads,

$$\frac{d}{d\lambda} \delta n^\alpha = -\Gamma_{\mu\nu}^\alpha n^\mu n^\nu, \quad (\text{A.23})$$

and measures the change in  $n^\alpha$  induced by gravitational interaction. The Christoffel symbols of the metric are now derived to first order in the perturbative metric  $h_{\mu\nu}$ . However, aiming at the iSW effect, we are interested in the components transforming the time-component of  $n^\alpha$ . The latter is given by

$$\Gamma_{\mu\nu}^0 = -\frac{1}{2} \left[ \partial_\nu h_{\mu 0} + \partial_\mu h_{\nu 0} - \partial_0 h_{\mu\nu} \right] \quad (\text{A.24})$$

The first two terms include spatial derivatives of the metric perturbation and give rise to the conventional Sachs-Wolfe effect, while the last term with the time derivative  $\partial_0 h_{\mu\nu}$  represents the origin of the iSW-effect. Substitution into the geodesic equation (A.23) yields

$$\frac{d}{d\lambda} \delta n^0 = -\frac{1}{2} \partial_0 h_{\mu\nu} n^\mu n^\nu \quad (\text{A.25})$$

The energy shift  $\delta n^0$  of a photon can be derived,

$$\begin{aligned} \delta n^0 &= \frac{1}{c^2} \int d\lambda \begin{pmatrix} n^0 \\ \mathbf{n} \end{pmatrix}' \begin{pmatrix} \partial\Phi/\partial\eta & 0 \\ 0 & \partial\Phi/\partial\eta \end{pmatrix} \begin{pmatrix} n^0 \\ \mathbf{n} \end{pmatrix} \\ &= \frac{1}{c^2} \int d\lambda \left[ (n^0)^2 + \mathbf{n}^2 \right] \frac{\partial\Phi}{\partial\eta} \\ &= \frac{2}{c^2} \int d\lambda \frac{\partial\Phi}{\partial\eta}. \end{aligned} \quad (\text{A.26})$$

In principle, the geodesic equation (A.23) could be solved in an iterative manner. The first step is summing up the corrections along the unperturbed path, which is called Born approximation. This was done in eqn. (A.26) for the time part of the geodesic equation. Then, the energy shift is obtained and the geodesic remains characterized by the conditions  $(n^0)^2 = 1$  and  $\mathbf{n}^2 = 1$ . In a cosmological

context, the photon geodesic  $ds^2 = 0$  is given by  $d\chi = cd\eta/a = cd\eta$  with the conformal time  $\eta$ . The natural choice for the affine parameter  $\lambda$  in the comoving frame is now  $\eta$ . Since  $\eta$  and  $\lambda$  are linearly connected to each other, their ratio can be absorbed in the normalization of  $n$ . A generalization to higher order spatial and temporal perturbations of the photon geodesic is provided by [Pyne & Carroll \(1996\)](#).

#### A.4. Analytical details of signal-to-noise ratios

The squared signal-to-noise ratio  $\Sigma^2$  is given by the  $\chi^2$  between a detection and its zero hypothesis. In the course of its calculation, one has to ensure that no redundant information is taken into account. We present the calculation for the bispectra only, since it follows the same argumentation in the case of the trispectra. Neglecting redundancy due to any symmetries the mixed and pure bispectra would account for a  $\chi^2$ -contribution of

$$\chi^2 = \frac{f_{\text{sky}}}{\pi} \frac{1}{(2\pi)^2} \int d^2\ell_{1,2,3} d^2\ell_{1',2',3'} \delta_{\text{D}}(\ell_1 + \ell_2 + \ell_3) B_{i_1 i_2 i_3}^{\ell_1, \ell_2, \ell_3} \text{Cov}^{-1} \left[ \tilde{B}_{i_1 i_2 i_3}^{\ell_1, \ell_2, \ell_3}, \tilde{B}_{i'_1 i'_2 i'_3}^{\ell'_1, \ell'_2, \ell'_3} \right] \tilde{B}_{i'_1 i'_2 i'_3}^{\ell'_1, \ell'_2, \ell'_3}, \quad (\text{A.27})$$

where also the sum over all field indices is implied. However, the integrand is symmetric in any simultaneous pairwise permutation of  $(\ell_n, i_n)$  with  $(\ell_m, i_m)$  and likewise of  $(\ell'_n, i'_n)$  with  $(\ell'_m, i'_m)$ . This type of redundancy can be avoided by constraining the integration volumes to  $\ell_1 < \ell_2 < \ell_3$  and  $\ell'_1 < \ell'_2 < \ell'_3$ . Furthermore, the sum over field indices may lead to more redundancy, which we encode at this point into a factor  $s_{i_1 i_2 i_3}^{i'_1 i'_2 i'_3}$ . Now, the signal-to-noise ratio can be written as

$$\begin{aligned} (\Sigma^{(3)})^2 &= \frac{f_{\text{sky}}}{4\pi^3} \int_{\ell_1 < \ell_2 < \ell_3} d^2\ell_{1,2,3} \int_{\ell'_1 < \ell'_2 < \ell'_3} d^2\ell_{1',2',3'} \delta_{\text{D}}(\ell_1 + \ell_2 + \ell_3) \\ &\quad \times B_{i_1 i_2 i_3}^{\ell_1, \ell_2, \ell_3} \text{Cov}^{-1} \left[ \tilde{B}_{i_1 i_2 i_3}^{\ell_1, \ell_2, \ell_3}, \tilde{B}_{i'_1 i'_2 i'_3}^{\ell'_1, \ell'_2, \ell'_3} \right] \tilde{B}_{i'_1 i'_2 i'_3}^{\ell'_1, \ell'_2, \ell'_3} \left( s_{i_1 i_2 i_3}^{i'_1 i'_2 i'_3} \right)^{-1}, \end{aligned} \quad (\text{A.28})$$

In this subspace the covariance matrix can be inverted, as it was shown in Section 6.4.2. Substituting eqn. (6.30) into eqn. (A.28), we find

$$(\Sigma^{(3)})^2 = \frac{f_{\text{sky}}}{4\pi^3} \left( s_{i_1 i_2 i_3}^{i'_1 i'_2 i'_3} \right)^{-1} \int_{\ell_1 < \ell_2 < \ell_3} d^2\ell_1 d^2\ell_2 B_{i_1 i_2 i_3}^{\ell_1, \ell_2, \ell_3} \frac{\tilde{C}_{i_1 i'_1}^* \tilde{C}_{i_2 i'_2}^* \tilde{C}_{i_3 i'_3}^*}{\det C^{\ell_1} \det C^{\ell_2} \det C^{\ell_3}} \tilde{B}_{i'_1 i'_2 i'_3}^{\ell_1, \ell_2, \ell_3}, \quad (\text{A.29})$$

where from now on  $\ell_3 = -\ell_1 - \ell_2$  is implied, if  $\ell_3$  is not integrated over. If one is now interested in the signal-to-noise ratio of a particular field mixture, i.e. data with a fixed field configuration  $q = i_1 + i_2 + i_3$ , one can further simplify the expression. For pure galaxy contributions,  $q = q' = 0$ , we can neglect the cross-correlation, i.e.  $C_{01} = 0$ , and no redundancy due to field summation occurs,  $s_{000}^{000} = 1$ . One obtains the well-known case ([Hu, 2001](#))

$$\left( \Sigma_0^{(3)} \right)^2 = \frac{f_{\text{sky}}}{4\pi^3} \int d^2\ell_1 d^2\ell_2 \frac{\left( B_{000}^{\ell_1, \ell_2, \ell_3} \right)^2}{6 \tilde{C}_{00}^{\ell_1} \tilde{C}_{00}^{\ell_2} \tilde{C}_{00}^{\ell_3}}, \quad (\text{A.30})$$

where the symmetry in the integrand was used to obtain an integration over full  $\ell$ -space in combination with the factor 1/6. If all mixed spectra with one iSW field are taken into account, i.e.  $q = q' = 1$ , one obtains 9 different contributions due to the field index summation. Three contributions are quadratic in identical bispectra,  $(i_1, i_2, i_3) = (i'_1, i'_2, i'_3)$ , and have multiplicity one. The remaining mixed contributions have multiplicity 2, since the integrand in eqn. (A.29) is symmetric under exchange of

the primed and unprimed index sets  $(i_1, i_2, i_3)$  and  $(i'_1, i'_2, i'_3)$  as a whole. Therefore the multiplicities are

$$\begin{aligned} 1 &= s_{001}^{001} = s_{010}^{010} = s_{100}^{100} \\ 2 &= s_{001}^{010} = s_{001}^{100} = s_{010}^{100} = s_{010}^{001} = s_{100}^{001} = s_{100}^{010}. \end{aligned} \quad (\text{A.31})$$

If one uses

$$\begin{aligned} B_{010}^{\ell_1, \ell_2, \ell_3} &= B_{001}^{\ell_1, \ell_3, \ell_2} \\ B_{100}^{\ell_1, \ell_2, \ell_3} &= B_{001}^{\ell_3, \ell_2, \ell_1} \end{aligned} \quad (\text{A.32})$$

in combination with

$$B_{001}^{\ell_1, \ell_2, \ell_3} = \frac{1}{2} (B_{001}^{\ell_1, \ell_2, \ell_3} + B_{001}^{\ell_2, \ell_1, \ell_3}), \quad (\text{A.33})$$

one can combine the quadratic terms to one, which is integrated over the full  $\ell_{1,2,3}$ -volume. This can be done for the mixed terms in analogy. One is left with the following expression for the signal-to-noise ratio,

$$\begin{aligned} (\Sigma_1^{(3)})^2 &= \frac{f_{\text{sky}}}{4\pi^3} \int d^2\ell_1 d^2\ell_2 (2 \det C^{\ell_1} \det C^{\ell_2} \det C^{\ell_3})^{-1} \\ &\quad \left[ (B_{001}^{\ell_1, \ell_2, \ell_3})^2 \tilde{C}_{11}^{\ell_1} \tilde{C}_{11}^{\ell_2} \tilde{C}_{00}^{\ell_3} + B_{001}^{\ell_1, \ell_2, \ell_3} \tilde{C}_{11}^{\ell_1} \tilde{C}_{01}^{\ell_2} \tilde{C}_{01}^{\ell_3} B_{010}^{\ell_1, \ell_2, \ell_3} \right]. \end{aligned} \quad (\text{A.34})$$

Following the analogous path of argumentation one finds the signal-to-noise expressions for the trispectra,

$$\begin{aligned} (\Sigma_0^{(4)})^2 &= \frac{f_{\text{sky}}}{8\pi^4} \int d^2\ell_1 d^2\ell_2 d^2\ell_3 \frac{(T_{0000}^{\ell_1, \ell_2, \ell_3, \ell_4})^2}{24 \tilde{C}_{00}^{\ell_1} \tilde{C}_{00}^{\ell_2} \tilde{C}_{00}^{\ell_3} \tilde{C}_{00}^{\ell_4}} \\ (\Sigma_1^{(4)})^2 &= \frac{f_{\text{sky}}}{8\pi^4} \int d^2\ell_1 d^2\ell_2 d^2\ell_3 (\det C^{\ell_1} \dots \det C^{\ell_4})^{-1} \\ &\quad \left[ \frac{1}{6} (T_{0001}^{\ell_1, \ell_2, \ell_3, \ell_4})^2 \tilde{C}_{11}^{\ell_1} \tilde{C}_{11}^{\ell_2} \tilde{C}_{11}^{\ell_3} \tilde{C}_{00}^{\ell_4} \right. \\ &\quad \left. + \frac{1}{4} T_{0001}^{\ell_1, \ell_2, \ell_3, \ell_4} \tilde{C}_{11}^{\ell_1} \tilde{C}_{11}^{\ell_2} \tilde{C}_{01}^{\ell_3} \tilde{C}_{01}^{\ell_4} T_{0010}^{\ell_1, \ell_2, \ell_3, \ell_4} \right]. \end{aligned} \quad (\text{A.35})$$

Also the expressions for higher values of  $q$  can now be deduced with the same techniques.

# B Appendix B

## Numerical Details

### B.1. The correction integrals

In this section, we would like to give detailed insight in the procedure of numerically solving the correction integrals in eqn. (3.10), as it was firstly performed in Pietroni (2008),

$$A_{acd,bef}^k = \frac{k}{4\pi} \int d^3q \frac{1}{2} \left\{ \gamma_{acd}^{k,q,p} \left( \gamma_{bgh}^{k,q,p} P_{ge}^q P_{hf}^p + \gamma_{egh}^{q,p,k} P_{gf}^p P_{hb}^k + \gamma_{fgh}^{p,k,q} P_{gb}^k P_{hb}^q \right) + (q \leftrightarrow p) \right\}. \quad (\text{B.1})$$

The free 3d-integration runs over  $\mathbf{q}$  while the  $\delta_{\text{D}}$  delta function in the vertex  $\tilde{\gamma}_{acd}^{k,q,p}$  induces the condition  $\mathbf{p} = -\mathbf{q} - \mathbf{k}$ . Therefore, we can choose the coordinate system as it is depicted in Fig. B.1. Due

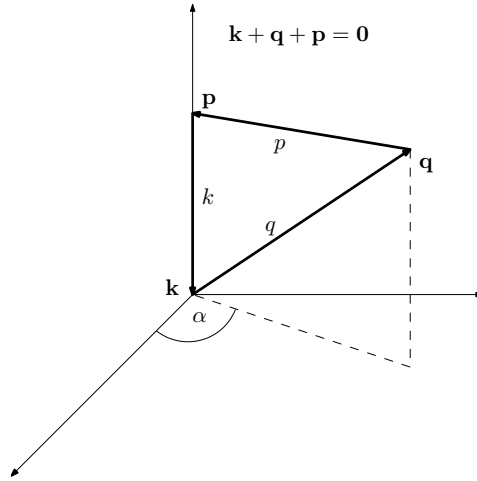


**Figure B.1.:** Graphical illustration of the coordinate system chosen for the numerical integration of the integrals in eqn. (B.1). The condition  $\mathbf{k} + \mathbf{q} + \mathbf{p} = 0$  is induced by the  $\delta_{\text{D}}$  delta function in the vertex  $\tilde{\gamma}_{acd}^{k,q,p}$ . Due to isotropy, the angular integration is trivial and can be carried out independently.

to isotropy, the result must not depend on the direction of  $\mathbf{k}$  and the orientation of the triangle. For this reason, the angular integration is trivial and can be carried out independently. Performing the coordinate transformation, one can now write the integral as

$$A_{acd,bef}^k = \int_{k/2}^{\infty} dq q \int_{|q-k|}^q dp p \frac{1}{2} \left\{ \gamma_{acd}^{k,q,p} \left( \gamma_{bgh}^{k,q,p} P_{ge}^q P_{hf}^p + \gamma_{egh}^{q,p,k} P_{gf}^p P_{hb}^k + \gamma_{fgh}^{p,k,q} P_{gb}^k P_{hb}^q \right) + (q \leftrightarrow p) \right\}. \quad (\text{B.2})$$

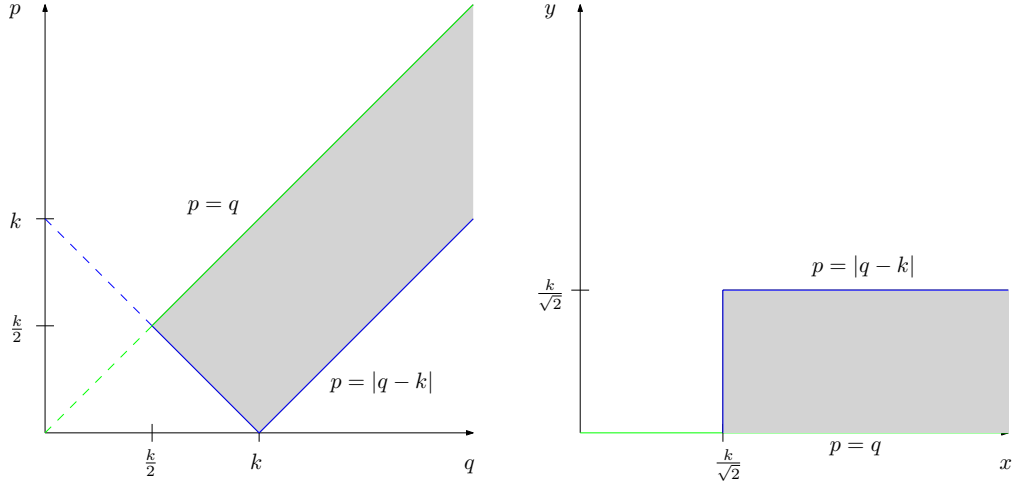


**Figure B.2.:** Coordinate transformation for the integrals  $A_{acd,bef}^k$ . The coordinate transformation from eqn. (B.3) decouples the integration boundaries.

In order to obtain independent integration boundaries, we furthermore perform another transformation,

$$\begin{pmatrix} p \\ q \end{pmatrix} \rightarrow \begin{pmatrix} x \\ y \end{pmatrix} = \begin{pmatrix} \frac{q+p}{\sqrt{2}} \\ \frac{q-p}{\sqrt{2}} \end{pmatrix}. \quad (\text{B.3})$$

The change of integration area is depicted in Fig. B.4. The integration boundaries decouple and the integral can be rewritten as

$$A_{acd,bef}^k = \int_{\frac{k}{\sqrt{2}}}^{\infty} dx \int_0^{\frac{k}{\sqrt{2}}} dy \frac{x^2 - y^2}{\sqrt{2}} \left[ F_{acd} \left( k, \frac{x+y}{\sqrt{2}}, \frac{x-y}{\sqrt{2}} \right) + (y \leftrightarrow -y) \right], \quad (\text{B.4})$$

where  $F_{acd}(k, q, p)$  is defined by

$$F_{acd}(k, q, p) = \gamma_{acd}^{k,q,p} \left( \gamma_{bgh}^{k,q,p} P_{ge}^q P_{hf}^p + \gamma_{egh}^{q,p,k} P_{gf}^p P_{hb}^k + \gamma_{fgh}^{p,k,q} P_{gb}^k P_{hb}^q \right). \quad (\text{B.5})$$

Now the integration can be derived numerically. The upper limit of the integration has to be truncated at a maximum wave number  $k_{\max}$ . The value of  $k_{\max}$  has to be chosen high enough to ensure the required saturation.

## B.2. Monte Carlo integration

In Chapter 3 and Chapter 6  $d$ -dimensional integrals of a function  $f(x)$  over a volume  $U \subset \mathbb{R}^d$  of the type

$$I = \int_U dx f(x) \quad (\text{B.6})$$

have to be solved numerically. For traditional trapezoidal techniques the error  $\Delta N$  scales with  $N^{-2/d}$ , where  $N$  is the number of function evaluations. The computation time is proportional to the number of function evaluations  $N$  and will increase dramatically for higher dimensions, since the error decreases slower with  $N$ . In contrast to this, for Monte Carlo integration techniques, the error estimate scales independent of the dimension,

$$\Delta N \propto \frac{1}{\sqrt{N}}. \quad (\text{B.7})$$

Different algorithms have been developed with individual advantages and drawbacks (Weinzierl, 2000; Hahn, 2005). In this section we would like to shortly lay out the simple idea every Monte Carlo algorithm is based on. By coordinate transformation the integration area can be reduced to the  $d$ -dimensional hypercube  $[0, 1]^d$ . If we now draw equally distributed random values  $x_i$ , the value of the integral can be estimated to be

$$E = \frac{1}{N} \sum_{n=1}^N f(x_n). \quad (\text{B.8})$$

Due to the law of large numbers the Monte Carlo estimate of the integral will converge to the real value of the integral,

$$\lim_{N \rightarrow \infty} \frac{1}{N} \sum_{n=1}^N f(x_n) = I. \quad (\text{B.9})$$

If one now defines for finite  $N$  an error estimate in form of the variance  $\sigma^2(f)$ ,

$$\sigma^2(f) = \int dx (f(x) - I)^2, \quad (\text{B.10})$$

one can easily show that

$$\int dx_1 \dots \int dx_N \left( \frac{1}{N} \sum_{n=1}^N f(x_n) - I \right)^2 = \frac{\sigma^2(f)}{N}. \quad (\text{B.11})$$

This means, that the error of the Monte Carlo estimator is on average  $\sigma(f)/\sqrt{N}$ . For this reason, Monte Carlo integration techniques have become the methods of choice in case of higher dimensions.



# C

## Appendix C

# Fourier conventions

In this additional remark we would like to give the definitions of the different Fourier conventions used in this work. In spite of bearing in mind the identical mathematical concept, it is in different fields of physics sensible and established to use different conventions in order to obtain equations in a clearer form. To avoid confusion for the reader it is necessary always mention which convention one is using.

## C.1. Spatial transformations

### C.1.1. Convention 1

This is the standard convention used in most applications in astrophysics. The Fourier transform of a scalar function  $f(\mathbf{x})$  in  $n$ -dimensional space is defined as

$$f(\mathbf{k}) = \int d^n x f(\mathbf{x}) e^{i\mathbf{k}\cdot\mathbf{x}}. \quad (\text{C.1})$$

The inverse transform is consequently performed with an inverse  $(2\pi)^n$  factor,

$$f(\mathbf{x}) = \int \frac{d^n k}{(2\pi)^n} f(\mathbf{k}) e^{-i\mathbf{x}\cdot\mathbf{k}}. \quad (\text{C.2})$$

For checking the inverse Fourier transform the integral representation of the  $n$ -dimensional Dirac delta function has to be employed,

$$\int d^n k e^{-i\mathbf{k}\cdot(\mathbf{x}_2-\mathbf{x}_1)} = (2\pi)^n \delta_{\text{D}}(\mathbf{x}_2 - \mathbf{x}_1). \quad (\text{C.3})$$

In this convention the power spectrum and higher order correlators in 3d-space are defined with a factor of  $(2\pi)^3$  in front of them,

$$\begin{aligned} \langle \delta(\mathbf{k}_1)\delta(\mathbf{k}_2) \rangle &= (2\pi)^3 P^{k_1} \delta_{\text{D}}(\mathbf{k}_1 + \mathbf{k}_2) \\ \langle \delta(\mathbf{k}_1)\delta(\mathbf{k}_2)\delta(\mathbf{k}_3) \rangle &= (2\pi)^3 B^{k_1,k_2,k_3} \delta_{\text{D}}(\mathbf{k}_1 + \mathbf{k}_2 + \mathbf{k}_3) \\ \langle \delta(\mathbf{k}_1)\delta(\mathbf{k}_2)\delta(\mathbf{k}_3)\delta(\mathbf{k}_4) \rangle &= (2\pi)^3 Q^{k_1,k_2,k_3,k_4} \delta_{\text{D}}(\mathbf{k}_1 + \mathbf{k}_2 + \mathbf{k}_3 + \mathbf{k}_4). \end{aligned} \quad (\text{C.4})$$

this convention will be used in the majority of the applications, namely in Chapters 4-6.

### C.1.2. Convention 2

In the course of Chapters (2)-(3) another convention is more convenient and established. The factor of  $(2\pi)^n$  is simply shifted to the transformation from real-space to  $\mathbf{k}$ -space. The Fourier transform of a scalar function  $f(\mathbf{x})$  in  $n$ -dimensional space is defined as

$$f(\mathbf{k}) = \int \frac{d^n x}{(2\pi)^n} f(\mathbf{x}) e^{i\mathbf{k}\cdot\mathbf{x}}. \quad (\text{C.5})$$

The inverse transformation is consequently performed with an inverse  $(2\pi)^n$  factor,

$$f(\mathbf{x}) = \int d^n x f_+(\mathbf{x}) e^{-i\mathbf{x}\cdot\mathbf{k}}. \quad (\text{C.6})$$

In this convention the power spectrum and higher order correlators in 3d-space are defined without a factor of  $(2\pi)^3$  in front of them,

$$\begin{aligned} \langle \delta(\mathbf{k}_1)\delta(\mathbf{k}_2) \rangle &= P^{k_1} \delta_{\text{D}}(\mathbf{k}_1 + \mathbf{k}_2) \\ \langle \delta(\mathbf{k}_1)\delta(\mathbf{k}_2)\delta(\mathbf{k}_3) \rangle &= B^{k_1,k_2,k_3} \delta_{\text{D}}(\mathbf{k}_1 + \mathbf{k}_2 + \mathbf{k}_3) \\ \langle \delta(\mathbf{k}_1)\delta(\mathbf{k}_2)\delta(\mathbf{k}_3)\delta(\mathbf{k}_4) \rangle &= Q^{k_1,k_2,k_3,k_4} \delta_{\text{D}}(\mathbf{k}_1 + \mathbf{k}_2 + \mathbf{k}_3 + \mathbf{k}_4). \end{aligned} \quad (\text{C.7})$$

## C.2. Time transformations, Laplace transform

In order to study the frequency spectrum of a time evolving function  $f(t)$  it is sometimes useful to transform into frequency space,

$$f(\omega) = \int_0^{\infty} dt f(t) e^{i\omega t}. \quad (\text{C.8})$$

The inverse transformation is defined in analogy to Section (C.1.1) with the factor  $1/(2\pi)$  included,

$$f(t) = \int_0^{\infty} \frac{d\omega}{2\pi} f(\omega) e^{-i\omega t}. \quad (\text{C.9})$$

One can interpret this transformation as a one-sided Fourier transform or a special case of a Laplace transform. With the substitution  $s = -i\omega$  one can write the same transformation as

$$f(s) = \int_0^{\infty} dt f(t) e^{-st}. \quad (\text{C.10})$$

This technique can be useful to separate linear solutions of differential equations from their non-linear part by transforming time differential operators into simple algebraic expressions.

# D Appendix D

## Units and constants

In this appendix astronomical units and physical constants are given, which are relevant for this thesis.

### D.1. Astronomical units and physical constants

The average distance of our Earth to the sun defines one astronomical unit (AU),

$$1 \text{ AU} = 1.4960 \times 10^{13} \text{ cm} . \quad (\text{D.1})$$

The distance to the Sun, at which the parallax of the Earth motion around the Sun is  $1''$  (arcsecond), is defined as one parsec (pc). The intuitive definition is depicted in Fig. D.1. The word “parsec” is an abbreviation for “*parallax of one arcsecond*”. It is

$$1 \text{ pc} = 3.2616 \text{ ly} = 3.0857 \times 10^{18} \text{ cm} . \quad (\text{D.2})$$

One Megaparsec (Mpc) is therefore

$$1 \text{ Mpc} = 3.0857 \times 10^{24} \text{ cm} . \quad (\text{D.3})$$

The speed of light  $c$  is

$$c = 2.9979 \times 10^{10} \text{ cm s}^{-1} . \quad (\text{D.4})$$

The gravitational constant  $G$  is

$$G = 6.6720 \times 10^{-8} \text{ cm}^3 \text{ g}^{-1} \text{ s}^{-2} . \quad (\text{D.5})$$

The Hubble constant  $H_0$ , representing the expansion rate of our Universe today, is

$$H_0 = 100 h \text{ km s}^{-1} \text{ Mpc}^{-1} = (9.7778)^{-1} h \text{ Gyr}^{-1} = 3.2408 \times 10^{-18} h \text{ s}^{-1} . \quad (\text{D.6})$$

The critical density  $\rho_c$  of the Universe is given by

$$\rho_c \equiv \frac{3H_0^2}{8\pi G} = 2.7754 \times 10^{11} h^2 M_\odot \text{ Mpc}^{-3} = 1.8788 \times 10^{-29} h^2 \text{ g cm}^{-3} . \quad (\text{D.7})$$

The size of the visible Universe is described by the Hubble radius  $\chi_H$ ,

$$\chi_H \equiv \frac{c}{H_0} = 2997.9 h^{-1} \text{ Mpc} = 9.2506 \times 10^{27} h^{-1} \text{ cm} . \quad (\text{D.8})$$

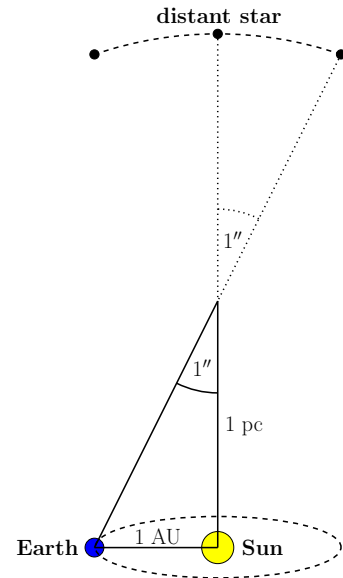


**Figure D.1.:** Definition of a parsec.  
Figure taken from Angrick (2011).



# Bibliography

- ABRAMOWITZ, M. & STEGUN, I. A., *Handbook of Mathematical Functions* (1972)
- ADLER, R. J., *The Geometry of Random Fields* (The Geometry of Random Fields, Chichester: Wiley, 1981, 1981)
- AFSHORDI, N., LOH, Y.-S., & STRAUSS, M. A. (2004): *Cross-correlation of the cosmic microwave background with the 2MASS galaxy survey: Signatures of dark energy, hot gas, and point sources*. Phys. Rev. D, **69** (8), 083524. [[link](#)]
- ANGRICK, C. (2011): *On the derivation of an X-ray temperature function without reference to mass and the prediction of weak-lensing number counts from the statistics of Gaussian random fields*. Ph.D. thesis, University of Heidelberg
- ANGULO, R. E., BAUGH, C. M., FRENK, C. S., & LACEY, C. G. (2008): *The detectability of baryonic acoustic oscillations in future galaxy surveys*. MNRAS, **383**, 755. [[link](#)]
- ANSELMIS, S., BALLESTEROS, G., & PIETRONI, M. (2011a): *Non-linear dark energy clustering*. J. Cosmology Astropart. Phys., **11**, 14. [[link](#)]
- ANSELMIS, S., MATARRESE, S., & PIETRONI, M. (2011b): *Next-to-leading resummations in cosmological perturbation theory*. J. Cosmology Astropart. Phys., **6**, 15. [[link](#)]
- ANSELMIS, S. & PIETRONI, M. (2012): *Nonlinear Power Spectrum from Resummed Perturbation Theory: a Leap Beyond the BAO Scale*. ArXiv e-prints
- AUDREN, B. & LESGOURGUES, J. (2011): *Non-linear matter power spectrum from Time Renormalisation Group: efficient computation and comparison with one-loop*. J. Cosmology Astropart. Phys., **10**, 37. [[link](#)]
- BARDEEN, J. M., BOND, J. R., KAISER, N., & SZALAY, A. S. (1986): *The statistics of peaks of Gaussian random fields*. ApJ, **304**, 15. [[link](#)]
- BARTELMANN, M. (2004): *Cosmology*. Lecture
- BARTELMANN, M. & SCHNEIDER, P. (2001): *Weak gravitational lensing*. Phys. Rep., **340**, 291. [[link](#)]
- BERNARDEAU, F., COLOMBI, S., GAZTAÑAGA, E., & SCOCCIMARRO, R. (2002): *Large-scale structure of the Universe and cosmological perturbation theory*. Phys. Rep., **367**, 1. [[link](#)]
- BERNARDEAU, F., CROCCE, M., & SCOCCIMARRO, R. (2008): *Multipoint propagators in cosmological gravitational instability*. Phys. Rev. D, **78** (10), 103521. [[link](#)]
- BIELBY, R., SHANKS, T., SAWANGWIT, U., ET AL. (2010): *Photometric selection of emission-line galaxies, clustering analysis and a search for the integrated Sachs-Wolfe effect*. MNRAS, **403**, 1261. [[link](#)]
- BLAKE, C., COLLISTER, A., BRIDLE, S., & LAHAV, O. (2007): *Cosmological baryonic and matter densities from 600000 SDSS luminous red galaxies with photometric redshifts*. MNRAS, **374**, 1527. [[link](#)]
- BOUGHN, S. & CRITTENDEN, R. (2004): *A correlation between the cosmic microwave background and large-scale structure in the Universe*. Nature, **427**, 45. [[link](#)]

- BOUGHN, S. P. & CRITTENDEN, R. G. (2005): *The cross-correlation between the microwave and X-ray backgrounds: foregrounds and systematics*. MNRAS, **360**, 1013. [\[link\]](#)
- BOUGHN, S. P., CRITTENDEN, R. G., & TUROK, N. G. (1998): *Correlations between the cosmic X-ray and microwave backgrounds: constraints on a cosmological constant*. New A, **3**, 275. [\[link\]](#)
- CARLSON, J., WHITE, M., & PADMANABHAN, N. (2009): *Critical look at cosmological perturbation theory techniques*. Phys. Rev. D, **80** (4), 043531. [\[link\]](#)
- COLES, P. & LUCCHIN, F., *Cosmology: The Origin and Evolution of Cosmic Structure, Second Edition* (2002)
- COORAY, A. (2002): *Nonlinear integrated Sachs-Wolfe effect*. Phys. Rev. D, **65** (8), 083518. [\[link\]](#)
- CRITTENDEN, R. G. & TUROK, N. (1996): *Looking for a Cosmological Constant with the Rees-Sciama Effect*. Physical Review Letters, **76**, 575. [\[link\]](#)
- CROCCE, M. & SCOCCIMARRO, R. (2006a): *Memory of initial conditions in gravitational clustering*. Phys. Rev. D, **73** (6), 063520. [\[link\]](#)
- CROCCE, M. & SCOCCIMARRO, R. (2006b): *Renormalized cosmological perturbation theory*. Phys. Rev. D, **73** (6), 063519. [\[link\]](#)
- CROCCE, M. & SCOCCIMARRO, R. (2008): *Nonlinear evolution of baryon acoustic oscillations*. Phys. Rev. D, **77** (2), 023533. [\[link\]](#)
- DURRER, R., *The Cosmic Microwave Background* (Cambridge University Press, 2008)
- EINSTEIN, A. (1915): *Die Feldgleichungen der Gravitation*. Sitzungsberichte der Königlich Preussischen Akademie der Wissenschaften (Berlin), 844–847
- EINSTEIN, A. (1916): *Die Grundlage der allgemeinen Relativitätstheorie*. Annalen der Physik, **354**, 769. [\[link\]](#)
- EISENSTEIN, D. J. & HU, W. (1998): *Baryonic Features in the Matter Transfer Function*. ApJ, **496**, 605. [\[link\]](#)
- EISENSTEIN, D. J., HU, W., & TEGMARK, M. (1998): *Cosmic Complementarity:  $H_0$  and  $\Omega_M$  from Combining Cosmic Microwave Background Experiments and Redshift Surveys*. ApJ, **504**, L57. [\[link\]](#)
- EISENSTEIN, D. J., SEO, H.-J., & WHITE, M. (2007): *On the Robustness of the Acoustic Scale in the Low-Redshift Clustering of Matter*. ApJ, **664**, 660. [\[link\]](#)
- EISENSTEIN, D. J., ZEHAVI, I., HOGG, D. W., ET AL. (2005): *Detection of the Baryon Acoustic Peak in the Large-Scale Correlation Function of SDSS Luminous Red Galaxies*. ApJ, **633**, 560. [\[link\]](#)
- EVRAUD, A. E., BIALEK, J., BUSH, M., ET AL. (2008): *Virial Scaling of Massive Dark Matter Halos: Why Clusters Prefer a High Normalization Cosmology*. ApJ, **672**, 122. [\[link\]](#)
- FIXSEN, D. J. (2009): *The Temperature of the Cosmic Microwave Background*. ApJ, **707**, 916. [\[link\]](#)
- FREEDMAN, W. L., MADORE, B. F., GIBSON, B. K., ET AL. (2001): *Final Results from the Hubble Space Telescope Key Project to Measure the Hubble Constant*. Astrophys.J., **553**:47-72,2001
- FRIEDMANN, A. (1922): *Über die Krümmung des Raumes*. Zeitung für Physik, **10**, 377. [\[link\]](#)

- FRIEDMANN, A. (1924): *Über die Möglichkeit einer Welt mit konstanter negativer Krümmung des Raumes*. Zeitung für Physik, **21**, 326. [\[link\]](#)
- FROMMERT, M., ENSSLIN, T. A., & KITaura, F. S. (2008): *Optimal ISW detection and joint likelihood for cosmological parameter estimation*. MNRAS, **391**, 1315
- FRY, J. N. (1996): *The Evolution of Bias*. ApJ, **461**, L65. [\[link\]](#)
- GIANNANTONIO, T., SCRANTON, R., CRITTENDEN, R. G., ET AL. (2008): *Combined analysis of the integrated Sachs-Wolfe effect and cosmological implications*. Phys. Rev. D, **77** (12), 123520. [\[link\]](#)
- GLAZEBROOK, K., EISENSTEIN, D., DEY, A., NICHOL, B., & THE WFMOS FEASIBILITY STUDY DARK ENERGY TEAM (2005): *Dark Energy and Cosmic Sound:  $w(z)$  Surveys with the Gemini/Subaru Wide-Field Multi-Object Spectrograph*. ArXiv Astrophysics e-prints
- GROFF, M. H., GRINSTEIN, B., REY, S.-J., & WISE, M. B. (1986): *Coupling of modes of cosmological mass density fluctuations*. ApJ, **311**, 6. [\[link\]](#)
- GRANETT, B. R., NEYRINCK, M. C., & SZAPUDI, I. (2008): *Dark Energy Detected with Supervoids and Superclusters*. ArXiv e-prints
- GUO, H. & JING, Y. P. (2009): *A Determination of Dark Matter Bispectrum with a Large Set of N-Body Simulations*. ApJ, **698**, 479. [\[link\]](#)
- HAHN, T. (2005): *CUBA-a library for multidimensional numerical integration*. Computer Physics Communications, **168**, 78. [\[link\]](#)
- HEITMANN, K., LUKIĆ, Z., FASEL, P., ET AL. (2008): *The cosmic code comparison project*. Computational Science and Discovery, **1** (1), 015003. [\[link\]](#)
- HEITMANN, K., WHITE, M., WAGNER, C., HABIB, S., & HIGDON, D. (2010): *The Coyote Universe. I. Precision Determination of the Nonlinear Matter Power Spectrum*. ApJ, **715**, 104. [\[link\]](#)
- HERNÁNDEZ-MONTEAGUDO, C. (2010): *Revisiting the WMAP-NVSS angular cross correlation. A skeptic's view*. A&A, **520**, A101. [\[link\]](#)
- HILL, G. J., GEBHARDT, K., KOMATSU, E., ET AL. (2008): *The Hobby-Eberly Telescope Dark Energy Experiment (HETDEX): Description and Early Pilot Survey Results*. **399**, 115
- HO, S., HIRATA, C. M., PADMANABHAN, N., SELJAK, U., & BAHCALL, N. (2008): *Correlation of CMB with large-scale structure: I. ISW Tomography and Cosmological Implications*. Phys.Rev.D, **78:043519,2008**
- HU, W. (2000): *Weak lensing of the CMB: A harmonic approach*. Phys. Rev. D, **62** (4), 043007. [\[link\]](#)
- HU, W. (2001): *Angular trispectrum of the cosmic microwave background*. Phys. Rev. D, **64** (8), 083005. [\[link\]](#)
- HUBBLE, E. (1929): *A Relation between Distance and Radial Velocity among Extra-Galactic Nebulae*. Proceedings of the National Academy of Science, **15**, 168. [\[link\]](#)
- HUFF, E., SCHULZ, A. E., WHITE, M., SCHLEGEL, D. J., & WARREN, M. S. (2007): *Simulations of baryon oscillations*. Astroparticle Physics, **26**, 351. [\[link\]](#)
- HÜTSI, G. (2006): *Acoustic oscillations in the SDSS DR4 luminous red galaxy sample power spectrum*. A&A, **449**, 891. [\[link\]](#)

- JAIN, B. & BERTSCHINGER, E. (1994): *Second-order power spectrum and nonlinear evolution at high redshift*. ApJ, **431**, 495. [\[link\]](#)
- JEONG, D. & KOMATSU, E. (2006): *Perturbation Theory Reloaded: Analytical Calculation of Nonlinearity in Baryonic Oscillations in the Real-Space Matter Power Spectrum*. ApJ, **651**, 619. [\[link\]](#)
- JEONG, D. & KOMATSU, E. (2009): *Perturbation Theory Reloaded. II. Nonlinear Bias, Baryon Acoustic Oscillations, and Millennium Simulation in Real Space*. ApJ, **691**, 569. [\[link\]](#)
- JÜRGENS, G. & BARTELMANN, M. (2012): *Perturbation theory trispectrum in the time renormalization approach*. MNRAS, **230**. [\[link\]](#)
- JÜRGENS, G. & SCHÄFER, B. M. (2012a): *Cross bispectra and trispectra of the non-linear integrated Sachs-Wolfe effect and the tracer galaxy density field*. MNRAS, accepted, ArXiv e-prints 1210.7513
- JÜRGENS, G. & SCHÄFER, B. M. (2012b): *Integrated Sachs-Wolfe tomography with orthogonal polynomials*. MNRAS, **425** (4), 2589. [\[link\]](#)
- KNOX, L. (1995): *Determination of inflationary observables by cosmic microwave background anisotropy experiments*. Phys. Rev. D, **52**, 4307. [\[link\]](#)
- KOMATSU, E., SMITH, K. M., DUNKLEY, J., ET AL. (2011): *Seven-year Wilkinson Microwave Anisotropy Probe (WMAP) Observations: Cosmological Interpretation*. ApJS, **192**, 18. [\[link\]](#)
- LEMAÎTRE, G. (1927): *Un Univers homogène de masse constante et de rayon croissant rendant compte de la vitesse radiale des nébuleuses extra-galactiques*. Annales de la Societe Scientifique de Bruxelles, **47**, 49
- LESGOURGUES, J., MATARRESE, S., PIETRONI, M., & RIOTTO, A. (2009): *Non-linear power spectrum including massive neutrinos: the time-RG flow approach*. J. Cosmology Astropart. Phys., **6**, 17. [\[link\]](#)
- LESGOURGUES, J. & PASTOR, S. (2006): *Massive neutrinos and cosmology*. Phys. Rep., **429**, 307. [\[link\]](#)
- LEWIS, A., CHALLINOR, A., & LASENBY, A. (2000): *Efficient Computation of Cosmic Microwave Background Anisotropies in Closed Friedmann-Robertson-Walker Models*. ApJ, **538**, 473. [\[link\]](#)
- LIMBER, D. N. (1953): *The Analysis of Counts of the Extragalactic Nebulae in Terms of a Fluctuating Density Field*. ApJ, **117**, 134. [\[link\]](#)
- LINDER, E. V. (1997): *Post-Newtonian Sachs-Wolfe effect*. A&A, **326**, 23
- LÓPEZ-CORREDOIRA, M., SYLOS LABINI, F., & BETANCORT-RIJO, J. (2010): *Absence of significant cross-correlation between WMAP and SDSS*. A&A, **513**, A3. [\[link\]](#)
- LUE, A., SCOCCIMARRO, R., & STARKMAN, G. (2004): *Differentiating between modified gravity and dark energy*. Phys. Rev. D, **69** (4), 044005. [\[link\]](#)
- LUMSDEN, S. L., HEAVENS, A. F., & PEACOCK, J. A. (1989): *The clustering of peaks in a random Gaussian field*. MNRAS, **238**, 293
- MAGGIORE, M., *Book Review: A MODERN INTRODUCTION TO QUANTUM FIELD THEORY / Oxford University Press, 2005, volume 59* (2006)
- MARINUCCI, D. & PECCATI, G. (2009): *Ergodicity and Gaussianity for Spherical Random Fields*. ArXiv e-prints 0911.2502

- MARTINEZ-GONZALEZ, E., SANZ, J. L., & SILK, J. (1994): *Imprints of galaxy clustering evolution on delta T/T*. ApJ, **436**, 1. [\[link\]](#)
- MATARRESE, S. & PIETRONI, M. (2007): *Resumming cosmic perturbations*. J. Cosmology Astropart. Phys., **6**, 26. [\[link\]](#)
- MATARRESE, S. & PIETRONI, M. (2008): *Baryonic Acoustic Oscillations via the Renormalization Group*. Modern Physics Letters A, **23**, 25. [\[link\]](#)
- MC EWEN, J. D., VIELVA, P., HOBSON, M. P., MARTÍNEZ-GONZÁLEZ, E., & LASENBY, A. N. (2007): *Detection of the integrated Sachs-Wolfe effect and corresponding dark energy constraints made with directional spherical wavelets*. MNRAS, **376**, 1211. [\[link\]](#)
- MO, H. J., JING, Y. P., & WHITE, S. D. M. (1997): *High-order correlations of peaks and haloes: a step towards understanding galaxy biasing*. MNRAS, **284**, 189
- MUKHANOV, V., *Physical Foundations of Cosmology* (2005)
- NISHIZAWA, A. J., KOMATSU, E., YOSHIDA, N., TAKAHASHI, R., & SUGIYAMA, N. (2008): *Cosmic Microwave Background-Weak Lensing Correlation: Analytical and Numerical Study of Nonlinearity and Implications for Dark Energy*. ApJ, **676**, L93. [\[link\]](#)
- PADMANABHAN, N., SCHLEGEL, D. J., SELJAK, U., ET AL. (2007): *The clustering of luminous red galaxies in the Sloan Digital Sky Survey imaging data*. MNRAS, **378**, 852. [\[link\]](#)
- PEACOCK, J. A. & DODDS, S. J. (1996): *Non-linear evolution of cosmological power spectra*. MNRAS, **280**, L19
- PEEBLES, P. J. E. (1980): *The large-scale structure of the universe*
- PERLMUTTER, S., ALDERING, G., GOLDHABER, G., ET AL. (1999): *Measurements of Omega and Lambda from 42 High-Redshift Supernovae*. Astrophys.J., **517:565-586,1999**
- PIETRONI, M. (2008): *Flowing with time: a new approach to non-linear cosmological perturbations*. J. Cosmology Astropart. Phys., **10**, 36. [\[link\]](#)
- PIETRONI, M., MANGANO, G., SAVIANO, N., & VIEL, M. (2012): *Coarse-grained cosmological perturbation theory*. J. Cosmology Astropart. Phys., **1**, 19. [\[link\]](#)
- PLANCK COLLABORATION, ADE, P. A. R., AGHANIM, N., ET AL. (2011): *Planck early results. I. The Planck mission*. A&A, **536**, A1. [\[link\]](#)
- PUEBLAS, S. & SCOCCIMARRO, R. (2009): *Generation of vorticity and velocity dispersion by orbit crossing*. Phys. Rev. D, **80** (4), 043504. [\[link\]](#)
- PYNE, T. & CARROLL, S. M. (1996): *Higher-order gravitational perturbations of the cosmic microwave background*. Phys. Rev. D, **53**, 2920. [\[link\]](#)
- RASSAT, A. (2009): *The Effect of Redshift Distortions on the Integrated Sachs-Wolfe Signal*. ArXiv e-prints 0902.1759
- REES, M. J. & SCIAMA, D. W. (1968): *Large-scale Density Inhomogeneities in the Universe*. Nature, **217**, 511. [\[link\]](#)
- RIESS, A. G., FILIPPENKO, A. V., CHALLIS, P., ET AL. (1998): *Observational Evidence from Supernovae for an Accelerating Universe and a Cosmological Constant*. Astron.J., **116:1009-1038,1998**

- ROBERTSON, H. P. (1935): *Kinematics and World-Structure*. ApJ, **82**, 284. [\[link\]](#)
- SACHS, R. K. & WOLFE, A. M. (1967): *Perturbations of a Cosmological Model and Angular Variations of the Microwave Background*. ApJ, **147**, 73. [\[link\]](#)
- SAHNI, V. & COLES, P. (1995): *Approximation methods for non-linear gravitational clustering*. Phys. Rep., **262**, 1. [\[link\]](#)
- SANZ, J. L., MARTINEZ-GONZALEZ, E., CAYON, L., SILK, J., & SUGIYAMA, N. (1996): *Cosmic Microwave Background Radiation Power Spectrum in Cold Dark Matter Open Universes Up to Second-Order Perturbations*. ApJ, **467**, 485. [\[link\]](#)
- SCHÄFER, B. M. (2008): *Mixed three-point correlation functions of the non-linear integrated Sachs-Wolfe effect and their detectability*. MNRAS, **388**, 1394. [\[link\]](#)
- SCHÄFER, B. M. & BARTELMANN, M. (2006): *Weak lensing in the second post-Newtonian approximation: gravitomagnetic potentials and the integrated Sachs-Wolfe effect*. MNRAS, **369**, 425. [\[link\]](#)
- SCHÄFER, B. M. & HEISENBERG, L. (2011): *Weak lensing tomography with orthogonal polynomials*. ArXiv e-prints 1107.2213
- SCHÄFER, B. M., KALOVIDOURIS, A. F., & HEISENBERG, L. (2011): *Parameter estimation biases due to contributions from the Rees-Sciama effect to the integrated Sachs-Wolfe spectrum*. MNRAS, **416**, 1302. [\[link\]](#)
- SELJAK, U. (1996a): *Gravitational Lensing Effect on Cosmic Microwave Background Anisotropies: A Power Spectrum Approach*. ApJ, **463**, 1. [\[link\]](#)
- SELJAK, U. (1996b): *Rees-Sciama Effect in a Cold Dark Matter Universe*. ApJ, **460**, 549. [\[link\]](#)
- SEO, H.-J. & EISENSTEIN, D. J. (2003): *Probing Dark Energy with Baryonic Acoustic Oscillations from Future Large Galaxy Redshift Surveys*. ApJ, **598**, 720. [\[link\]](#)
- SHETH, R. K., MO, H. J., & TORMEN, G. (2001): *Ellipsoidal collapse and an improved model for the number and spatial distribution of dark matter haloes*. MNRAS, **323**, 1. [\[link\]](#)
- SMAIL, I., HOGG, D. W., BLANDFORD, R., ET AL. (1995): *The discovery of two giant arcs in the rich cluster A2219 with the Keck telescope*. MNRAS, **277**, 1
- SMITH, R. E., PEACOCK, J. A., JENKINS, A., ET AL. (2003): *Stable clustering, the halo model and non-linear cosmological power spectra*. MNRAS, **341**, 1311. [\[link\]](#)
- SMOOT, G. & DAVIDSON, K., *Wrinkles in time* (1993)
- SPERGEL, D. N., VERDE, L., PEIRIS, H. V., ET AL. (2003): *First-Year Wilkinson Microwave Anisotropy Probe (WMAP) Observations: Determination of Cosmological Parameters*. ApJS, **148**, 175. [\[link\]](#)
- SPRINGEL, V. (2005): *The cosmological simulation code GADGET-2*. MNRAS, **364**, 1105. [\[link\]](#)
- STOMPOR, R. & EFSTATHIOU, G. (1999): *Gravitational lensing of cosmic microwave background anisotropies and cosmological parameter estimation*. MNRAS, **302**, 735. [\[link\]](#)
- SUNYAEV, R. A. & ZELDOVICH, I. B. (1980): *Microwave background radiation as a probe of the contemporary structure and history of the universe*. ARA&A, **18**, 537. [\[link\]](#)
- TAKAHASHI, R., YOSHIDA, N., MATSUBARA, T., ET AL. (2008): *Simulations of baryon acoustic oscillations - I. Growth of large-scale density fluctuations*. MNRAS, **389**, 1675. [\[link\]](#)

- 
- TASSEV, S. & ZALDARRIAGA, M. (2011): *The Mildly Non-Linear Regime of Structure Formation*. ArXiv e-prints
- TEGMARK, M. & PEEBLES, P. J. E. (1998): *The Time Evolution of Bias*. ApJ, **500**, L79. [[link](#)]
- TEGMARK, M., TAYLOR, A. N., & HEAVENS, A. F. (1997): *Karhunen-Loeve Eigenvalue Problems in Cosmology: How Should We Tackle Large Data Sets?* ApJ, **480**, 22. [[link](#)]
- TULUIE, R. & LAGUNA, P. (1995): *The imprint of proper motion of nonlinear structures on the cosmic microwave background*. ApJ, **445**, L73. [[link](#)]
- VALAGEAS, P. (2008): *Expansion schemes for gravitational clustering: computing two-point and three-point functions*. A&A, **484**, 79. [[link](#)]
- VIELVA, P., MARTÍNEZ-GONZÁLEZ, E., & TUCCI, M. (2006): *Cross-correlation of the cosmic microwave background and radio galaxies in real, harmonic and wavelet spaces: detection of the integrated Sachs-Wolfe effect and dark energy constraints*. MNRAS, **365**, 891. [[link](#)]
- WALKER, A. G. (1935): *On Riemannian Spaces with Spherical Symmetrie about a Line, and the Conditions for Isotropy in General Relativity*. The Quarterly Journal of Mathematics, **os-6** (1), 81. [[link](#)]
- WEINBERG, S., *Cosmology* (Oxford University Press, 2008)
- WEINZIERL, S. (2000): *Introduction to Monte Carlo methods*. ArXiv High Energy Physics - Phenomenology e-prints
- ZALDARRIAGA, M., SPERGEL, D. N., & SELJAK, U. (1997): *Microwave Background Constraints on Cosmological Parameters*. ApJ, **488**, 1. [[link](#)]
- ZHANG, P. (2006): *Testing gravity against the early time integrated Sachs-Wolfe effect*. Phys. Rev. D, **73**, 123504. [[link](#)]
- ZWICKY, F. (1937): *On the Masses of Nebulae and of Clusters of Nebulae*. ApJ, **86**, 217. [[link](#)]



# Acknowledgements

Now it's time to thank everyone who supported me in writing this thesis - in whatever way.

I want to thank you, Matthias, for giving me the opportunity to work on this exciting topic. With you as a supervisor I could always be sure to count on your spontaneous and efficient help - even with tedious calculations - whenever I needed it. Especially, I appreciate that you gave me the scientific freedom to also work on other subjects. Also your notion of life besides physics should not be taken as granted. Thank you for all this!

The next person, I want to thank here, calling his everyday effort for helping students as self-evident is Björn Malte Schäfer. It was a pleasure working with you and I will always have a bad conscience for having stolen so much of your valuable time. Also, I will keep in mind the after-work mountain bike tours up to *Weißer Stein* or *Königstuhl*.

I thank Luca Amendola to agree on being my second corrector as well as Karlheinz Meier and Jürgens Berges to take part in my PhD committee.

The time during my PhD would not have been as exciting without the famous ITA-girls and ITA-boys. Besides the various scientific discussions I enjoyed the working atmosphere in general but also the beer at *Bar Centrale*, ITA hiking days and movie nights. At this point it is not only time to thank - I also want to apologize for all the bad and the very bad puns - especially to my in every sense extraordinary office mates Christian, Alex, Ana and the frequent visitor Björn. Thank you for the wonderful time in *Northeim*.

Now, I have to apologize to the non-German speakers, but I have to continue in German.

Ganz besonders möchte ich mich bei meiner Mutter bedanken. Auch wenn Du immer den Eindruck hast, nichts von dem zu verstehen, was ich da mache, hast Du einen großen Teil dazu beigetragen, dass ich bis hier gekommen bin. Dies gilt natürlich in ganz anderer Weise auch für meinen Vater, der dies leider nicht mehr miterleben kann. Ihr beide habt mir so viele Möglichkeiten gegeben, mich zu entfalten, und ward Unterstützer und Rückzugsort in meinem bisherigen Leben, wie man es sich kaum besser wünschen kann. Auch ohne Euch, Wieland und Rainald, wäre ich sicher nicht der, der ich jetzt bin, und bin immer wieder glücklich darüber, Euch meine Brüder nennen zu dürfen.

Liebe Amélie, auch wenn Du hier ganz zum Schluss auftauchst, solltest Du eigentlich ganz oben stehen. Deinetwegen habe ich immer wieder die Kraft gehabt weiterzumachen, wenn es nicht lief oder ich mal wieder gezweifelt habe. Dass Du mir manchmal den Kopf zurecht rückst möchte ich auch ganz gewiss nicht missen. Danke, dass Du da bist ...

